SPATIALLY INTEGRATED ERBIUM-DOPED FIBER AMPLIFIERS ENABLING SPACE-DIVISION MULTIPLEXING

Thèse

Cang Jin

Doctorat en génie électrique
Philosophiæ doctor (Ph.D.)

Québec, Canada

SPATIALLY INTEGRATED ERBIUM-DOPED FIBER AMPLIFIERS ENABLING SPACE-DIVISION MULTIPLEXING

Thèse

Cang Jin

Sous la direction de :

Sophie LaRochelle, directeur de recherche

Résumé

L'augmentation exponentielle de la demande de bande passante pour les communications laisse présager une saturation prochaine de la capacité des réseaux de télécommunications qui devrait se matérialiser au cours de la prochaine décennie. En effet, la théorie de l'information prédit que les effets non linéaires dans les fibres monomodes limite la capacité de transmission de celles-ci et peu de gain à ce niveau peut être espéré des techniques traditionnelles de multiplexage développées et utilisées jusqu'à présent dans les systèmes à haut débit. La dimension spatiale du canal optique est proposée comme un nouveau degré de liberté qui peut être utilisé pour augmenter le nombre de canaux de transmission et, par conséquent, résoudre cette menace de «crise de capacité». Ainsi, inspirée par les techniques micro-ondes, la technique émergente appelée multiplexage spatial (SDM) est une technologie prometteuse pour la création de réseaux optiques de prochaine génération.

Pour réaliser le SDM dans les liens de fibres optiques, il faut réexaminer tous les dispositifs intégrés, les équipements et les sous-systèmes. Parmi ces éléments, l'amplificateur optique SDM est critique, en particulier pour les systèmes de transmission pour les longues distances. En raison des excellentes caractéristiques de l'amplificateur à fibre dopée à l'erbium (EDFA) utilisé dans les systèmes actuels de pointe, l'EDFA est à nouveau un candidat de choix pour la mise en œuvre des amplificateurs SDM pratiques. Toutefois, étant donné que le SDM introduit une variation spatiale du champ dans le plan transversal de la fibre, les amplificateurs à fibre dopée à l'erbium spatialement intégrés (SIEDFA) nécessitent une conception soignée.

Dans cette thèse, nous examinons tout d'abord les progrès récents du SDM, en particulier les amplificateurs optiques SDM. Ensuite, nous identifions et discutons les principaux enjeux des SIEDFA qui exigent un examen scientifique. Suite à cela, la théorie des EDFA est brièvement présentée et une modélisation numérique pouvant être utilisée pour simuler les SIEDFA est proposée. Sur la base d'un outil de simulation fait maison, nous proposons une nouvelle conception des profils de dopage annulaire des fibres à quelques-modes dopées à l'erbium (ED-FMF) et nous évaluons numériquement la performance d'un amplificateur à un

étage, avec fibre à dopage annulaire, à ainsi qu'un amplificateur à double étage pour les communications sur des fibres ne comportant que quelques modes. Par la suite, nous concevons des fibres dopées à l'erbium avec une gaine annulaire et multi-cœurs (ED-MCF). Nous avons évalué numériquement le recouvrement de la pompe avec les multiples cœurs de ces amplificateurs. En plus de la conception, nous fabriquons et caractérisons une fibre multi-cœurs à quelques modes dopées à l'erbium. Nous réalisons la première démonstration des amplificateurs à fibre optique spatialement intégrés incorporant de telles fibres dopées. Enfin, nous présentons les conclusions ainsi que les perspectives de cette recherche.

La recherche et le développement des SIEDFA offriront d'énormes avantages non seulement pour les systèmes de transmission future SDM, mais aussi pour les systèmes de transmission monomode sur des fibres standards à un cœur car ils permettent de remplacer plusieurs amplificateurs par un amplificateur intégré.

Abstract

The exponential increase of communication bandwidth demand is giving rise to the so-called '*capacity crunch*' expected to materialize within the next decade. Due to the nonlinear limit of the single mode fiber predicted by the information theory, all the state-of-the-art techniques which have so far been developed and utilized in order to extend the optical fiber communication capacity are exhausted. The spatial domain of the lightwave links is proposed as a new degree of freedom that can be employed to increase the number of transmission paths and, subsequently, overcome the looming '*capacity crunch*'. Therefore, the emerging technique named space-division multiplexing (SDM) is a promising candidate for creating next-generation optical networks.

To realize SDM in optical fiber links, one needs to investigate novel spatially integrated devices, equipment, and subsystems. Among these elements, the SDM amplifier is a critical subsystem, in particular for the long-haul transmission system. Due to the excellent features of the erbium-doped fiber amplifier (EDFA) used in current state-of-the-art systems, the EDFA is again a prime candidate for implementing practical SDM amplifiers. However, since the SDM introduces a spatial variation of the field in the transverse plane of the optical fibers, spatially integrated erbium-doped fiber amplifiers (SIEDFA) require a careful design.

In this thesis, we firstly review the recent progress in SDM, in particular, the SDM optical amplifiers. Next, we identify and discuss the key issues of SIEDFA that require scientific investigation. After that, the EDFA theory is briefly introduced and a corresponding numerical modeling that can be used for simulating the SIEDFA is proposed. Based on a home-made simulation tool, we propose a novel design of an annular based doping profile of few-mode erbium-doped fibers (FM-EDF) and numerically evaluate the performance of single stage as well as double-stage few-mode erbium-doped fiber amplifiers (FM-EDFA) based on such fibers. Afterward, we design annular-cladding erbium-doped multicore fibers (MC-EDF) and numerically evaluate the cladding pumped multicore erbium-doped fiber amplifier (MC-EDFA) based on these fibers as well. In addition to fiber design, we fabricate and characterize

a multicore few-mode erbium-doped fiber (MC-FM-EDF), and perform the first demonstration of the spatially integrated optical fiber amplifiers incorporating such specialty doped fibers. Finally, we present the conclusions as well as the perspectives of this research.

In general, the investigation and development of the SIEDFA will bring tremendous benefits not only for future SDM transmission systems but also for current state-of-the-art single-mode single-core transmission systems by replacing plural amplifiers by one integrated amplifier.

Contents

List of Tables

List of Figures

List of Abbreviations

AC-MC-EDF	Annular-cladding multicore erbium-doped fiber
ACA-MC-EDF	Annular-cladding with inner air-hole multicore erbium-doped fiber
ACS-MC-EDF	Annular-cladding with inner silica cladding multicore erbium-doped fiber
ASE	Amplified spontaneous emission
BER	Bit error ratio
CMA	Constant-modulus algorithm
C-MCF	Coupled multicore fiber
CPLS	Cladding pump light stripper
CPU	Central processing unit
CSI	Channel state information
DC-MC-EDF	Double cladding multicore erbium-doped fiber
DMG	Differential mode gain
DMGD	Differential mode group delay
DRA	Distributed Raman amplifier
DSP	Digital signal processing
EDF	Erbium-doped fiber
EDFA	Erbium-doped fiber amplifier
FM-EDF	Few-mode erbium-doped fiber
FM-EDFA	Few-mode erbium-doped fiber amplifier
FS	Free space

ESA	Excited state absorption
FEC	Forward error correction
FMF	Few-mode fiber
FUT	Fiber under test
FWM	Four-wave mixing
GI-FMF	Graded-index few-mode fiber
HOM	High order mode
ISI	Inter symbol interference
LCOS	Liquid crystal on silicon
LD	Laser diode
LG	Laguerre-Gaussian
LP	Linear polarized
LPG	Long period grating
LSM	Least square method
MC-EDF	Multicore erbium-doped fiber
MC-EDFA	Multicore erbium-doped fiber amplifier
MCF	Multicore fiber
MCFA	Multicore fiber amplifier
MC-FM-EDF	Multicore few-mode erbium-doped fiber
MC-FM-EDFA	Multicore few-mode erbium-doped fiber amplifier
MC-FMF	Multicore few-mode fiber
MC-GI-FMF	Multicore graded-index few-mode fiber

MC-SI-FMF	Multicore step index few-mode fiber
MCVD	Modified chemical vapor deposition
MDG	Mode dependent gain
MDL	Mode dependent loss
MDM	Mode division multiplexing
MIMO	Multi input multi output
MM-EDFA	Multimode erbium-doped fiber amplifier
MMF	Multimode fiber
NA	Numerical aperture
NF	Noise figure
OAM	Orbital angular momentum
ODE	Ordinary differential equation
FOPA	Fiber optical parametric amplifier
OSA	Optical spectrum analyzer
OSNR	Optical-signal-noise ratio
OVD	Outside vapor deposition
PCE	Power conversion efficiency
PCVD	Plasma chemical vapor deposition
PDM	Polarization division multiplexing
PL	Photonic lantern
PLC	Planar lightwave circuit
PON	Passive optical network

PP	Phase plate
QAM	Quadrature amplitude modulation
QPSK	Quadrature phase shift keying
ROADM	Reconfigurable optical add-drop multiplexer
SDM	Space-division multiplexing
SI-EDFA	Spatially integrated erbium-doped fiber amplifier
SI-FMF	Step-index few-mode fiber
SMF	Single mode fiber
SMUX	Spatial multiplexer
SNR	Signal to noise ratio
SOA	Semiconductor optical amplifier
SWI	Swept wavelength interferometer
TFB	Tapered fiber bundle
VAD	Vapor axial deposition
WDM	Wavelength division multiplexing
WSS	Wavelength selective switch
XPM	Cross-phase modulation
ZDMG	Zero-differential modal gain

List of Symbols

a	Fiber core radius
A_{21}	Spontaneous emission rate
$A_{\mathrm{clad,in}}$	Inner cladding area
$A_{\mathrm{clad,p}}$	Pump cladding area
A_{core}	Fiber core area
A_{Er}	Erbium doping area
A_{fiber}	Fiber transverse cross-section area
A_K	Area of the K^{th} layer
A_{ring}	Pump ring area
d_{core}	Fiber core diameter
$d_{\mathrm{ring,in}}$	Distances from the core edge to the inner ring side
$d_{\mathrm{ring,out}}$	Distances from the core edge to the outer ring side
$\mathrm{DMG}(\lambda)_{m-n}$	Differential gain between mode m and n at wavelength λ
E_{12}	Energy separation between level 1 and level 2
E_{1i}	Energy of i^{th} sub-level of level 1
F_{eff}	Relative effective index difference
g_1	Number of sub-levels
$G(\lambda)_m$	Gain of mode m at wavelength λ
h	Planck's constant
I_{in}	Incident light intensity

I_k	Beam intensity profile of the k^{th} channel
$I_{nk}(r,\varphi)$	Spatial dependent normalized beam intensity profile of the k^{th} channel
J_l	The l^{th} order Bessel function of the first kind
k_0	Wave number
k_B	Boltzmann constant
K_l	The l^{th} order modified Bessel function of the second kind
m_{1i}	Normalized i^{th} sub-level populations of level 1
m_{2j}	Normalized j^{th} sub-level populations of level 2
n_{co}	Fiber core refractive index
n_{cl}	Fiber cladding refractive index
$n_{\text{clad,p}}$	Refractive index of the pump ring
n_{eff}	Effective index of the fundamental mode without pump ring
n'_{eff}	Effective index of the fundamental mode with pump ring
N_1	Ions population density of level 1
$N_{1,K}$	Ions population density of level 1 for the K^{th} layer
N_2	Ions population density of level 2
$N_{2,K}$	Ions population density of level 2 for the K^{th} layer
N_{abs}	Number of photons that absorb the light
N_{core}	Number of cores
$N_i(r,\varphi)$	Spatial dependent ions population density of the i^{th} level
$N_{\text{n}}(r,\varphi)$	Spatial dependent normalized ions population density
N_{T}	Total erbium ions population density

$\bar{N}$	Average population density
$N_\rho(r,\varphi)$	Spatial dependent normalized erbium ion doping distribution
P_{abs}	Light power absorbed by the ions
$P_{\mathrm{i}}(z)$	ASE power at wavelength λ
$P_{\mathrm{i,m}}(z)$	ASE power at wavelength λ for m^{th} mode
P_{d}	Required pump power
P_{e}	Pump power saving factor
P_{em}	Light power emitted by the ions
$P_k(z)$	Total power at position z of the k^{th} channel
$P_{\mathrm{p}}(z)$	Pump power at position z
$P_{\mathrm{s}}(z)$	Signal power at position z
$P_{\mathrm{s,m}}(z)$	Signal power at position z for the m^{th} mode
$P_{\mathrm{s,out}}$	Output signal power
PCE_{clad}	Modified power conversion efficiency for cladding pumping
S_{p}	Pump power density
t	Time
t_{ring}	Total thickness of the pump ring
T	Temperature
u_k	Direction of the k^{th} propagating wavelength channel
U	Scalar transverse propagation parameter in the core
W	Scalar transverse propagation parameter in the cladding
W_{ijk}	Transition rates from levels i to level j for the k^{th} channel

$\alpha(\lambda)$	Power absorption coefficient at wavelength λ
α_k	Intrinsic background loss coefficient
β	Light propagation constant in the fiber
$\Gamma(\lambda)$	Overlap factor at wavelength λ
Γ_k	Overlap factor of the k^{th} channel
Γ_{i}	Overlap factor of the ASE at wavelength λ
$\Gamma_{(\mathrm{i},m),K}$	The m^{th} ASE mode power filling factor wavelength λ for the K^{th} layer
$\Gamma_{k,K}$	Power filling factor for the K^{th} layer of the k^{th} channel
Γ_{p}	Overlap factor of the pump
$\Gamma_{\mathrm{p},K}$	Pump power filling factor for the K^{th} layer
Γ_{s}	Overlap factor of the signal
$\Gamma_{(\mathrm{s},m),K}$	The m^{th} signal mode power filling factor for the K^{th} layer
$\Delta\nu_{\mathrm{i}}$	Bandwidth of the ASE at wavelength λ
$\Delta\nu_k$	Bandwidth of the k^{th} channel
ε	Average transition energy between two levels
η	Inversion ratio
λ	Wavelength
ν_{i}	Frequency of the ASE at wavelength λ
ν_k	Frequency of the k^{th} propagating wavelength channel
ν_{p}	Frequency of the pump
ν_{s}	Frequency of the signal
ρ	Erbium ion doping concentration

σ_{12}	Absorption cross-section of level 1 to level 2
σ_{13}	Pump absorption cross-section at frequency v
σ_{21}	Emission cross-section of level 2 to level 1
$\sigma_{1i,2j}$	Absorption cross-section, sub-level i^{th} of level 1 to sub-level j^{th} of level 2
$\sigma_{2j,1i}$	Emission cross-section, sub-level j^{th} of level 2 to sub-level i^{th} of level 1
σ_{ai}	Absorption cross-section at ASE wavelength
$\sigma_{\text{a}k}$	Absorption cross-section of the k^{th} propagating wavelength channel
σ_{ap}	Absorption cross-section at pump wavelength
σ_{as}	Absorption cross-section at signal wavelength
σ_{ei}	Emission cross-section at ASE wavelength
$\sigma_{\text{e}k}$	Emission cross-section of the k^{th} propagating wavelength channel
σ_{es}	Emission cross-section at signal wavelength
τ	Lifetime of the metastable level
$\phi(\omega)$	Photon flux at frequency ω
$\psi_{k,lm}(r,\varphi)$	Intensity profile of the lm mode of channel k
ω	Angular frequency

Dedicated to the loving memory of my grandparent.

And God said

$$\nabla \cdot \vec{D} = \rho$$

$$\nabla \cdot \vec{B} = 0$$

$$\nabla \times \vec{E} = -\frac{\partial \vec{B}}{\partial t}$$

$$\nabla \times \vec{H} = \vec{J} + \frac{\partial \vec{D}}{\partial t}$$

and then there was light

Acknowledgement

It would not be possible to obtain the Doctor of Philosophy without great support, selfless assistance, and friendly cooperation from numerous people during my pursuing the Ph.D. study. Here, I would like to express my deep and sincere appreciation to all the people who have helped me, although I know it will be never enough.

First and foremost, I would like to appreciate my supervisor, Prof. Sophie LaRochelle, for providing me an unparalleled opportunity to conduct my doctor researching in her lab and her visionary guidance, meticulous patience, and encouragement since I was her student. She guides me to the field of the optical fiber amplifier, in particular for the space-division multiplexing system, which will make tremendous contributions to next generation optical networks. Her profound knowledge, rigorous scholarship, and sincere passion for science direct me to grow into a researcher, from which I will definitely benefit in my further career. With her amiability and enthusiasm, I have quickly adapted to the new environment.

I would like to express my particular appreciation to Prof. Bora Ung, for his selfless assistance and fruitful discussion in most of my work. His is not only a qualified tutor but also a good friend and big brother in my mind. I would like to express my heartfelt appreciation to Prof. Younès Messaddeq, for his contribution to the fiber preparation and technical supporting. I also would like to express my gratitude to Prof. Leslie Ann Rusch, I learned a lot from her class and her advice.

I wish to thank the defense committee members, Prof. Leslie Ann Rusch, Prof. Lawrence R. Chen, and Prof. Christine Tremblay, for their kindly review, valuable comments and suggestions.

I will also take this unique chance to thank all my genius colleagues in Centre d'optique, photonique et laser at Université Laval. My officemates, Mr. Nicolas Ayotte, Dr. Alexandre Delisle-Simard, Mr. Léonard Gagné-Godbout, Dr. Benoit Filion, and Mr. Kéven Bédard, helped me a lot for study and daily life. I was very enjoying those days staying with them. I also learned a lot from our group members, Dr. Lixian Wang, Dr. Pravin Vaity, Dr. Charles Brunet, Dr. Chul-Soo Park, Dr. Wing-chau Ng, Dr. An-truong Nguyen, Dr. Jiachuan Lin, and Mr. Zhihui Cao. Thanks to our technicians and researchers, Mr. Philippe Chrétien, Mr. Patrick Larochelle, Mr. Souleymane-toubou Bah, Mr. Nicolas Grégoire, and Mr. Steeve Morency, my lab life would not be going well without their kind help and accompanying.

I am grateful to my mentor in Bell Labs, Dr. Nicolas K. Fontaine, for his smart guide, kindly help and personal humor which lead me to have an excellent internship. I am thankful to Dr. Haoshuo Chen whom I consider to be my co-mentor, for his enthusiasm in research and useful guidance in the experiment. I also would like to acknowledge to other people in Bell Labs, Dr. Roland Ryf, Dr. René-Jean Essiambre, Dr. Robert W. Tkach, Dr. Xi Chen and etc. Thanks to my labmates and also the interns in Bell Labs, Mr. Bin Huang, Mr. Kuanping Shang, and Ms. Chengcheng Gui, they made my life fantastic during the internship.

I would like to thank all my friends who shared happiness and sorrow with me in Quebec City. Without your accompanying, it will be hard and lonely for both my life and study. They are Dr. Huan Liang, Dr. Hu Zhang, Dr. Feng Liang, Dr. Linyao Yu, Ms. Yi Dong, Mr. Lei He, Dr. Xiaoqiang Wang, Dr. Zhiqiang Wang, Ms. Ruixuan Wang, Ms. Julie-Anne Roberge and Ms. Roxanne Hamel.

China Scholarship Council which is the most appreciated sponsor provided four-year financial support for my study in Université Laval. I also appreciate the Natural Sciences and Engineering Research Council of Canada (NSERC) supports my research.

Finally, I will present my deepest acknowledgement from the bottom of my heart to my family. My parents, they are continuously and unselfishly inspiring me to pursue my dream with their infinite love. My wife, Dr. Xinxia Liang, is accompanying me and making my life scientific and fantastic. Thank you for your consistent comprehension and encouragements. Without my family support, I would not be where I am now today.

Thank to all of you once again!

Foreword

The Chapter 3 to 5 of this thesis are reproductions of publised or submitted papers, apart from some minor modifications made in order to improve the thesis uniformity. The papers and manuscript presented in the thesis are listed below as as well as the thesis author's contributions.

The main part of Chapter 3 is a reproduction of the conference proceeding published in SPIE digital library.

> *J1. **C. Jin**, B. Ung, Y. Messaddeq, S. LaRochelle, "Tailored modal gain in a multi-mode erbium-doped fiber amplifier based on engineered ring doping profiles," Proc. SPIE 8915, Photonics North 2013, 89150A (October 11, 2013). doi:10.1117/12.2033945*

The thesis author's contributions to this article are:

a) The design of two types of erbium doping profile for few-mode erbium-doped fiber that supports three spatial modes. The goal of the fiber design is to achieve modal gain equalization as well as to provide dynamic gain adjustment.

b) The numerical evaluation of the performances including gain, noise figure, and spectrum flatness of the single stage and double-stage amplifiers based on designed fibers.

c) The writing of the first draft of the paper.

The main part of Chapter 4 is a reproduction of the following journal paper published in OSA digital library.

> *J2. **C. Jin**, B. Ung, Y. Messaddeq, S. LaRochelle, "Annular-cladding erbium doped multicore fiber for SDM amplification," Optics Express, Vol. 23, Issue 23, pp. 29647-29659 (November 4, 2015). doi:10.1364/OE.23.029647*

The thesis author's contributions to this article are:

a) The design of the multicore erbium-doped fiber and the optimization of the fiber parameters.

b) The numerical evaluation of the performances including gain, and noise figure to compare the performance of the classical design of multicore erbium-doped fiber to annular-cladding fibers with depressed or air inner claddings.
c) The numerical simulation of the multi-spot pump edge-coupling scheme.
d) The writing of the first draft of the paper.

The supplementary information at the end of Chapter 4 is a reproduction of a portion of the following conference proceeding that has been presented at the *Optical Fiber Communication Conference* (*OFC*) 2016.

> *C1. **C. Jin**, H. Chen, B. Huang, K. Shang, N. K. Fontaine, R. Ryf, R.-J. Essiambre, B. Ung, Y. Messaddeq, S. LaRochelle, "Characterization of Annular Cladding Erbium-Doped 6-Core Fiber Amplifier," OFC 2016, Tu2I .3, 2016. doi: 10.1364/OFC.2016.Tu2I.3*

The thesis author's contributions to this article are:
a) Calculations using a ray-tracing software to compare the pump confinement.
b) Experimental characterization and comparison of the index depressed solid and air-hole inner cladding annular-cladding multicore erbium-doped fiber.
c) The writing of the paper

Chaper 5 is a reproduction of the following manuscript submitted to Nature Photonics.

> *J3. H. Chen, **C. Jin**, B. Huang, N. K. Fontaine, R. Ryf, K. Shang, N. Grégoire, S. Morency, R.-J. Essiambre, G. Li, Y. Messaddeq, S. LaRochelle, "Spatially Integrated Optical Fiber Amplifier," Submitted to Nature Photonics (February 15, 2016)*

The thesis author's contributions to this article are:
a) The designed and modeling of the fiber, and the ray tracing simulations.
b) The experimental characterization of the optical fiber amplifier
c) The writing of part of the manuscript and supplementary material.

Chapter 1

Introduction

1.1 Capacity limit of single mode fiber links

Almost 50 years ago, a fantastic optical waveguide, the optical glass fiber, was invented by Sir Charles K. Kao and his colleague [1]. In the following decades, low loss fiber [2], erbium-doped fiber amplifier (EDFA) [3], wavelength division multiplexing (WDM) and etc. have been successively invented and developed resulting in the rapid evolution of optical fiber communication. From transoceanic communications to data exchange in data-centers, our communication networks increasingly rely on the optical fiber transmission links. Even in wireless communications, the optical fiber, operating behind the scene, is needed to supports such this huge worldwide mobile network.

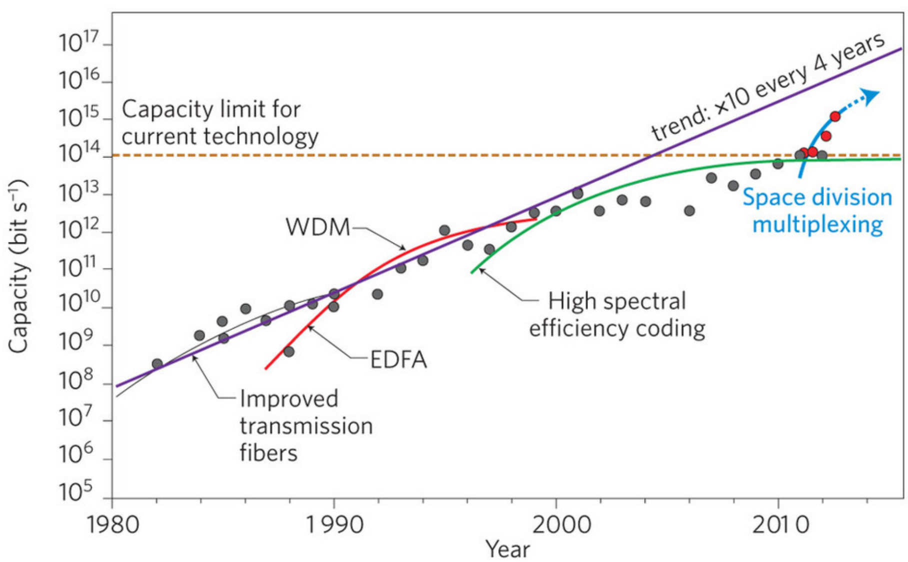

Figure 1.1. The evolution of the transmission capacity in optical fibers as evidenced by state-of-the-art laboratory transmission demonstrations. [4]

Currently, telecommunication, either cabled or wireless, is one of the important tools allowing people to obtain information and acquire knowledge in this *Information Explosion* era. As the main transmission technology, optical fibers that carry a large amount of high-speed data for either long-haul or short reach provide the huge capacity needed to sustain the traffic growth that enthusiast users create around the world. However, in the next two decades, optical fiber based communications will be facing an enormous challenge, as the needed capacity increases exponentially [5] for not only the long transmission distance and high speed data rate but also for short access data link, from the demand for so-called "cloud computing" performed by supercomputers or distributed computers, "big data" processed in data center and high definition video streaming through wireless connection, etc.

For many decades, researchers have investigated solutions and put tremendous efforts on increasing the data transmission capacity of the single-mode fiber. Although WDM and polarization division multiplexing (PDM), as well as advanced modulation formats, were introduced to significantly improve fiber capacity at the end of the last century, this capacity will be nearly exhausted in the forthcoming years [6]. According to the information theory derived by C. Shannon [7], the capacity limitation of conventional single mode fiber (SMF) is approximately 35 Tb/s (in band from 1530 nm to 1625 nm, i.e. C-band plus L-band) according to the spectral efficiency limit of 3 bit/Hz due to nonlinear effects [8]. This theoretical limit exacerbates the growing gap between the data transmission demand and the capacity offered by state-of-the-art technologies. However, not everything goes smoothly when we are attempting to enhance the bit rate on SMFs transmission links. In particular, trying to increase the transmission capacity beyond 100 Tb/s has been alleged to be insurmountable because of high signal to noise ratio (SNR) requirements, the bandwidth limitation of the optical amplifier [9] and the difficulty of high power launching due to the intensity dependent Kerr nonlinearity [10]. It, therefore, seems that a '*capacity crunch*' is looming. In light of this, new multiplexing technologies and encoding methods must be explored and debated in the research community to identify promising innovative paths to overcome the capacity limits imposed by current approaches [11].

1.2 Capacity increase brought about by new dimensions of light

Many different degrees of freedom, mentioned in the previous section are already employed to scale the SMFs capacity both in the lab and commercial products. In order to overcome the theoretical limitation indicated by C. Shannon and accommodate larger transmission capacities to keep up with the internet traffic growth, we need to transmit data in parallel rather than along a solo path, in analogy to the computers that have multicore in one central processing unit (CPU) for parallel calculation. Consequently, a new physical dimension, namely space, is now available and has been paid close attention to worldwide. Inspired by multi input multi output (MIMO) technology in wireless communication [12], space-division multiplexing (SDM) [13] and, in particular, mode division multiplexing (MDM) [14] are on the horizon. These emerging technologies grant optical fiber an exceptional opportunity to enlarge its capacity. Apart from the SDM concept, new components have been investigated or introduced to realize SDM accompanied with WDM, PDM and advanced modulation formats, e.g. multicore fiber (MCF) [15], few-mode fiber (FMF) [16], even multicore few-mode fiber (MC-FMF) [17] and relevant modules such as amplifier and multiplexer [18]. All these technologies are required to translate the potential of SDM into a viable solution for the future optical network.

1.2.1 Space-division multiplexing with multicore fibers

SDM can be seen as a multi-path system similar to the spatial diversity of wireless communication. However, in the latter, spatial diversity is used to counteract multi-path fading by transmitting the same information in all the channels and, in this way, enhancing the reliability but not the capacity. On the contrary, SDM with MCF enables the transmission of several, say N, independent channels carrying different information. These N distinct channels thus multiply the SMF capacity by a factor of N.

Figure 1.2 illustrates a typical system in which SDM establishes many parallel channels while still benefiting from earlier technologies such as WDM/PDM transmitters and advanced modulation like quadrature phase shift keying (QPSK) or quadrature amplitude modulation (QAM). Some new key components needed to implement SDM are MCFs, multicore fiber amplifier (MCFA), spatial multiplexer/demultiplexer, and other multicore compatible devices.

Ideally, there is no interaction between the cores of MCF but cross-talk can exist in the MCF if the cores are tightly packed in the shared cladding. Hopefully, using digital signal processing (DSP), especially MIMO processing after the data has been received by a coherent detector, such cross-talk could be mitigated.

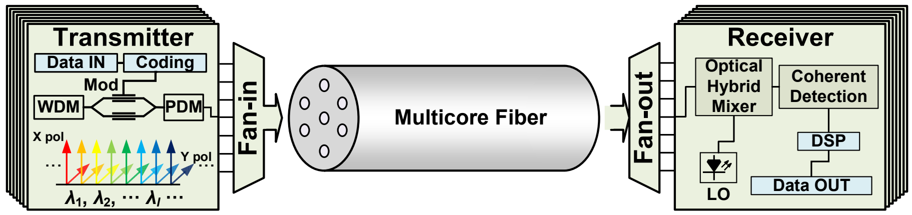

Figure 1.2. System scheme of typical multicore fiber based space-division multiplexing

1.2.2 Space-division multiplexing with multimode fibers

A different SDM solution has multiplexed channels that are built from several, say M, guided optical modes in an multimode fibers (MMF). This approach is called MDM. Those modes can be any set of orthogonal modes, e.g. linear polarized (LP), Laguerre-Gaussian (LG) or orbital angular momentum (OAM) modes. Among these different kinds of modes, the LP modes in weakly guided fibers are well known and easier to excite. The following discussion will focus on this approach.

Since the mode dispersion that exists in MMF leads to pulse broadening, one cannot use the MMF for long distance communication. Therefore, SMF was investigated and is used wildly in backbone links. Nevertheless, transmitting in only one mode, i.e. the fundamental mode with two polarization states, seems insufficient if we want to enlarge the capacity. We thus have to find solutions to surmount the drawbacks from the MMF.

Accordingly, the FMF was proposed as the propagating medium for the spatial optical channels. In the FMF, only a restricted number of modes can be guided through the fiber and this number is determined by the normalized frequency, i.e. the V number that associates the fiber core size and numerical aperture (NA) with the operating wavelength. In addition, mode selective excitation technique drives one WDM data stream carried on the assigned mode, and the multiple spatial channels can be separated at the receiver side by mode filtering.

A practical MDM system is shown in Figure 1.3 in which one just replaces all the multicore components of Figure 1.2 by the multimode/few-mode ones. Unlike the MCF, which can be easier to use in SDM, MDM has some issues inherent to the fact that the channels are sharing the same transmission path, e.g. inter-modal cross-talk occurring during propagation, amplification or input-output coupling will be higher.

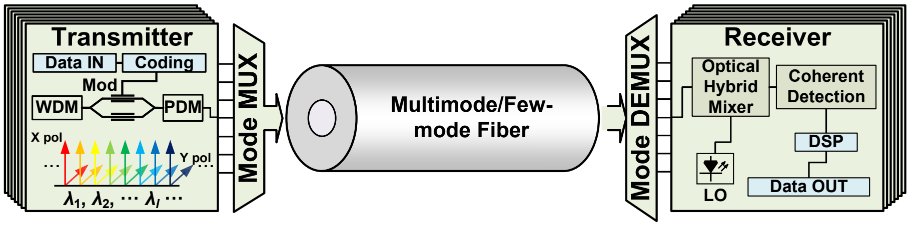

Figure 1.3. System scheme of typical multimode/few-mode fiber based mode division multiplexing

1.2.3 Recent progress in space-division multiplexing transmissions

Since 2010, the new degree of freedom, i.e. spatial multiplexing, has been proposed as a potential technique to overcome the fiber capacity limit mentioned above. At the optical fiber communication conference (*OFC*) 2011, R. Ryf et al. [19] firstly demonstrated the MDM transmission via a graded-index three-mode fiber (i.e. spatial modes LP_{01}, LP_{11a} and LP_{11b}). Various encouraging experimental transmission results based on SDM or MDM using MCF or FMF have been reported in post-deadline sessions of *OFC* and European conference on optical communication (*ECOC*). Both J. Sakaguchi et al. and B. Zhu et al. reported over 100 Tb/s capacity transmission in seven-core single mode fibers using WDM/SDM combined to PDM-QPSK modulation, achieving 109 Tb/s through 16.8 km MCF [20] and 112 Tb/s through 76.8 km MCF in the C+L band [21], respectively. Recently, the most memorable record has been reported in *ECOC* 2015 by B. J. Puttnam et al. who employed a 22-core fiber with 399 WDM channels to reach 2.15 Pb/s capacity [22]. Other interesting transmission demonstrations done over MCF are shown in Table 1.1.

Among those results, most of the high capacity records have been done with transmission over a single fiber span which does not emulate a realistic transmission link. Although [23] and [24] achieved quite long distance transmissions, even exceeding a few thousand kilometers, there was not any multicore amplifier implemented in the link until [25] was carried out.

Table 1.1. Recent progress in multicore transmission

Year	Capacity (Tb/s)	Channel rate (Gb/s)	WDM channels/core	Distance (km)	Span length (km)	Fiber type	No. of core	Ref.
2011	109.14	172	97	16.8	16.8	MCF	7	[20]
2011	112	107	160	76.8	76.8	MCF	7	[21]
2011	56	107	80	76.8	76.8	MCF	7	[26]
2011	7.84	1120	1	76.8	76.8	MCF	7	[27]
2011	8.96	128	10	2688	76.8	MCF	7	[23]
2011	0.168	56	1	24	24	C-MCF	3	[28]
2011	0.336	112	1	24	24	C-MCF	3	[29]
2011	0.22	80	1	1200	60	C-MCF	3	[30]
2012	0.96	80	5	4200	60	C-MCF	3	[24]
2012	305	172	100	10.1	10.1	MCF	19	[31]
2012	33.768	603	8	844.8	76.8	MCF	7	[32]
2012	37.856	676	8	1075.2	76.8	MCF	7	[33]
2012	35.84	128	40	6160	55	MCF	7	[25]
2012	1012.32	456	222	52	52	MCF	12	[34]
2013	140.7	100	201	7326	45.5	MCF	7	[35]
2013	688	92	748	1500	50	MCF	12	[36]
2014	108	600	30	1705	31	C-MCF	6	[37]
2015	120.7	95.8	180	204	204	MCF	7	[38]
2015	2150	6468	399	31	31	MCF	22	[22]

Table 1.2. Recent progress in few-mode transmission

Year	Capacity (Tb/s)	Channel rate (Gb/s)	WDM channels/mode	Distance (km)	Span length (km)	Fiber type	No. of mode	Ref.
2011	0.168	56	1	10	10	GI-FMF	3	[19]
2011	0.2	112	1	40	40	SI-FMF	2	[39]
2011	0.336	56	1	33	33	FMF	3	[40]
2011	0.56	112	1	40	40	SI-FMF	5	[41]
2011	29.568	112	88	50	50	FMF	3	[42]
2012	0.214	107	1	4.5	4.5	SI-FMF	2	[43]
2012	0.22	80	1	96	96	FMF	3	[44]
2012	0.31	112	1	85	85	FMF	3	[45]
2013	73.7	256	96	118.8	118.8	GI-FMF	3	[46]
2013	6.5	40	34	700	70	GI-FMF	3	[47]
2013	24.6	80	32	177	59	FMF	6	[48]
2013	0.336	56	1	900	25	SI-FMF	3	[49]
2013	1.013	337.5	1	130	130	FMF	3	[50]
2013	7.68	320	8	120	120	FMF	3	[51]
2013	33.288	38	146	500	50	GI-FMF	3	[52]
2014	57.6	960	20	60	60	FMF	3	[53]
2015	21.6	60	12	22.8	22.8	GI-FMF	15	[54]

Table 1.3. Recent progress in multicore few-mode transmission

Year	Capacity (Tb/s)	Channel rate (Gb/s)	WDM channels /core/mode	Distance (km)	Span length (km)	Fiber type	No. of core	No. of mode	Ref.
2014	9.524	243	50	1	1	MC-SI-FMF	7	3	[55]
2014	10.3284	105	20	40.4	40.4	MC-GI-FMF	12	3	[56]
2015	11.16	100	40	5.5	5.5	MC-SI-FMF	36	3	[57]
2015	0.16	10	8	9.8	9.8	MC-GI-FMF	19	6	[58]
2015	3.9348	40	20	527	52.7	MC-GI-FMF	12	3	[59]
2015	2052	50	360	9.8	9.8	MC-GI-FMF	19	6	[60]

Extending capacity by mean of MDM seems to be even more challenging. Regardless of the performance criteria considered (total capacity or transmission distance), MDM over FMF is inferior to MCF. V. Sleiffer et al. reported a 73.7 Tb/s transmission capacity of three spatial modes in cascaded FMF spools over 119 km, combined with WDM and PDM [46], which is known as the capacity record of MDM so far. On the other hand, nearly a thousand kilometers transmission was demonstrated in a 30 km three-mode fiber recirculating loop with photonic lantern based mode multiplexer [61]. Other interesting records of transmission in FMF are shown in Table 1.2.

An ultra-dense SDM implementation can be done by utilizing MC-FMF rather than MCF or FMF. With enlarged core size from previous MCF and adding trench or air-hold around the cores, MC-FMF integrates a maximum number of spatial channels within the limit of the cladding. Although only a few works reported transmission over such fibers, the outcomes are encouraging, e.g. over 2 Pb/s capacity was given by 19-core six-mode fiber for 10 km [60]. More descriptions of relevant references are available in Table 1.3.

1.3 Critical components in space-division multiplexing

Although some exultant performance has been achieved, enlarging the capacity by means of SDM or MDM encounters formidable issues that need to be addressed such as cross-talk, MIMO processing and new device or equipment etc.

1.3.1 Novel transmission fibers

The SDM technique, emphasizing the scaling of the spatial domain, requires novel fibers possessing more than one physical path in order to transmit parallel signal channels simultaneously. MCF and FMF are the most popular transmission medium used for SDM. Moreover, other fibers such as conventional MMF or microstructures fiber are attractive in SDM studies as well. Following, we will describe and discuss the MCF, FMF and their combination, i.e. MC-FMF. Figure 1.4 illustrates some of the SDM compatible fibers, including FMF, MMF, MCF and MC-FMF. The dark gray represents the core area while light gray is the cladding area.

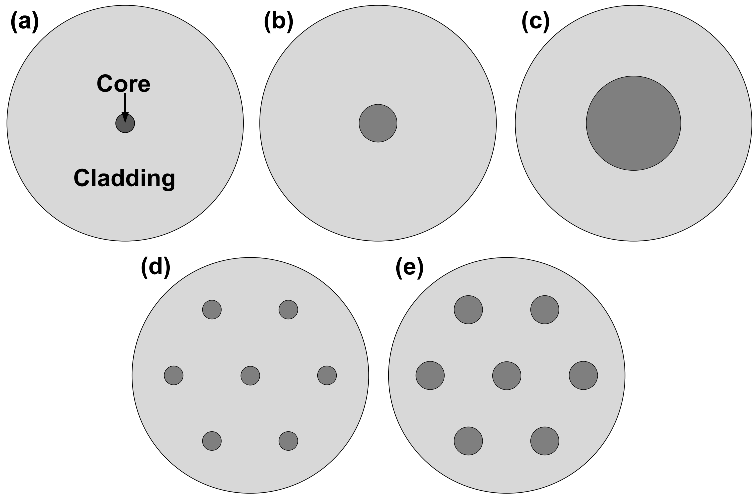

Figure 1.4. Structures for different types of optical fibers: (a) single-mode fiber; (b) few-mode fiber; (c) multimode fiber; (d) multicore fiber and (e) multicore few-mode fiber.

1.3.1.1 Multicore fiber

Although the MCF was reported tens of years ago [62], it has not been paid much attention in the context of optical fiber communications until SDM was proposed as a promising solution for next generation optical fiber networks. Compared to a bundle of fibers placed in one optical cable, MCF (see Figure 1.4) has N cores ($N > 1$) in a single fiber, which means that the cores are surrounded by the same cladding. Thus, it provides N parallel physical channels through only one fiber structure and enables a scale-up in capacity per fiber. Note that, the MCF described here has single mode cores. Based on the core-to-core pitch that determines coupling between adjacent cores, the single mode MCF can be classified in two categories, uncoupled and coupled. In order to prevent cross-talk from one core to another and avoid MIMO signal processing after the receiver, most reported MCFs utilize an uncoupled design.

Before MCF becomes a practical transmission medium solution, many engineering difficulties problems need to be resolved. In terms of fabrication, the preform for each core of an MCF can be prepared by a mature preform fabrication technology, e.g. modified chemical vapor deposition (MCVD). Thereafter, a number of preforms are assembled and drawn into an MCF. Those fabrication processes of MCF must maximize the number of cores in a limited cladding size, while keeping analogous performance to standard SMF (e.g. chromatic dispersion, polarization mode dispersion, background propagation loss, bending loss, mechanical strength, and ease of splicing and connection with other optical components or system equipment). To gain the advantage of spatial integration for cost saving, these MCFs must offer similar performance than state-of-the-art fiber links.

Certainly, the main problem hindering the number of cores being integrated and long-haul transmission performance with uncoupled MCF is cross-talk between cores. To deal with this, researchers have investigated some approaches to mitigate cross-talk by reducing power coupling and, although good results were obtained, the scalability is up to 22 cores so far [22]. K. Saitoh et al. presented a novel air-hole assisted multicore structure for suppressing the cross-talk between neighboring cores by achieving a coupling length of several tens of kilometers in a dual-core fiber [63]. Shortly afterward, T. Hayashi et al. reported a trench-assisted index profile that reduces cross-talk to less than -55.5 dB after 17.6 km propagation in a fiber that has seven cores with attenuation less than 0.18 dB/km and effective areas of about 80 μm^2 [64]. Besides the seven-core scheme, S. Matsuo et al. reported a ten core MCF with a large effective area which advances the scalability to a new level. Its cross-talk is observed to be -26 dB between outer cores and -30 dB between the outer cores and the central core after 100 km, while simultaneously keeping attenuation at 0.24 dB/km [65]. The above mentioned works reduced cross-talk by lessening coupling strength and almost always negated fluctuation of the index profile that can cause fiber imperfections and perturbations. In this case, the homogenous cores are characterized by identical propagation constants and cross-talk will accumulate after a long propagation distance even though the coupling is small. Hence, fibers with non-identical multicores, namely heterogeneous [66] and quasi-homogeneous [67] configurations have been studied. If the cores are no longer homogeneous, phase mismatch can reduce cross-talk but how much phase difference is needed to suppress cross-talk remains an open question. Another important parameter is the core arrangement, which is usually a hexagonally packed lattice. This strategy results in different cross-talk level for each core layer. A ring structure [68], [69] was proposed to avoid such variations because in this case the cores only suffer the cross-talk from the two adjacent cores located on either side. At *OFC*'2015, Sumitomo announced an eight-core fiber with a ring arrangement. It seems that this is not an aggressive core number, however, the cladding diameter is 125 μm, which is compatible with the standard system. Actually, the fiber cladding size cannot be larger than a few hundred micrometers since large cladding will make the fiber mechanically fragile.

Additionally, when MCF is used for short-reach links such as passive optical network (PON) and data center interconnection, bending loss is a critical factor to be concerned about.

1.3.1.2 Few-mode fiber

Like MCF, MMF is not a novel concept since MMF was widely used before SMF took the leading role in the backbone network shortly after the invention of the optical fiber. This is because the large modal dispersion of MMF has so far restricted its application, especially for long distance communication. Theoretically, the M orthogonal modes guided in MMF could multiply by M the capacity of the SMF.

The idea of MDM was first introduced with the goal to achieve two-mode multiplexing in MMF over few tens of meters [70]. Further increase in the capacity can be obtained through careful control of the fiber modal content. That means a limited number of modes will be excited and propagated in a specialty optical fiber, named FMF. Unlike MMF that supports a huge number of guided modes due to their large cores (usually seven to eight times larger than SMF), FMF supports a discrete number of well-defined spatial modes, typically two to nine LP modes that, considering their generate states, will provide six to 30 spatial channels. The number of modes is often limited by the need to selectively launch fiber modes for easy multiplexing and demultiplexing. FMF fabrication is similar to SMF, the core size just has to be enlarged.

For example, C. Koebele et al. reported a MIMO processing based five channels transmission at 100 Gb/s employing a FMF that supports four mode groups, i.e. LP_{01}, LP_{11}, LP_{21} and LP_{02} [41]. Because of technical difficulties associated with differential mode group delays (DMGD) as well as multiplexers, other experiments mostly only utilized two mode groups, i.e. the fundamental mode LP_{01} and the two spatially degenerated LP_{11} modes. E. Ip et al. presented a WDM transmission over 50 km using such a two-mode group fiber with a few-mode fiber amplifier, achieving three times more capacity than current 100 Gb/s system over short distance [42]. Beyond two LP modes, FMF supporting four, six, seven, and nine [71], [72] LP mode groups have been proposed and some fibers were experimentally demonstrated. As the number of modes is increased, DMGD must be controlled, which can be addressed by introducing a graded-index profile [71].

Besides DMGD, other critical issues such as mode selective injection, mode dependent loss (MDL), and inter- and intra-modal nonlinear effects also need to be considered and solved. To launch few modes into the fiber, offset launching or mode converter are used. A. Li et al. investigated a mode converter that deforms the input end of FMF by inducing a strength grating through the application of pressure with a metallic grating. The authors employed a 3-dB mode converter to equally excite LP_{01} and LP_{11} and another mode converter to transform LP_{11} back to LP_{01} [43]. C. Koebele et al. studied nonlinear effects in the FMF, and they pointed out that, if DMGD is sufficiently large, the nonlinear effect between two non-degenerate modes can be suppressed [73]. K. Ho et al. analyzed the statistical MDL in the strong-coupling regime, i.e. when the fiber can be seen as a cascaded independent characteristics segments and it is much longer than the correlation length, and small overall MDL. They found that the eigenvalue distribution of zero-trace Gaussian unitary ensemble can be used to describe the statistics of MDL and to calculate its standard deviation [74]. Finally, four-wave mixing (FWM) [75] and cross-phase modulation (XPM) [76] among inter-mode and intra-mode were both experimentally examined. Results indicate that inter-mode nonlinearity in the FMF can be fully phase matched far from the zero-dispersion wavelength of each spatial mode.

1.3.1.3 Multicore few-mode fiber

Naturally, if one can combine a multicore approach, with N distinct cores, and few-mode cores that support M spatial modes, the total capacity can be as high as $N \times M$ times that of SMF. The current MC-FMF make this vision a reality. As MCF, considering that the cores size is enlarged to guide more modes, this type of fiber can obviously suffer from larger cross-talk if the fiber geometry is otherwise unchanged compared to common MCF. Thanks to the trench made by air-holes, a low cross-talk seven-core × three-mode fiber with core pitch close to the single mode case has been investigated [17]. MC-FMFs are using this scheme to obtain more capacity, from seven-core to 36-core [57]. Meanwhile, the number of modes per core is extended from three-mode to six-mode [58]. The highest transmission record to this date, beyond 2 Pb/s in a MC-FMF, was achieved with 114 spatial channels spread over 19-core and six-mode per core [60]. Those fibers have important shortcomings, i.e. fiber lengths are limited to a few kilometers, which may only be suitable for access network or interconnections. However, such fiber configuration with a high density of cores is not easy to fabricate with good uniformity resulting in signals that will accumulate cross-talk during propagation. Again, MIMO processing has to be utilized to mitigate the impairment brought by cross-talk to achieve transmission distances ranging from tens of kilometers [56] to hundreds of kilometers [59].

1.3.2 New devices and subsystems

Since the fibers used in SDM are not compatible with standard SMF systems and components, new devices such as multiplexers [18], isolators, and attenuators, and subsystems like amplifiers, wavelength selective switches (WSS) must be investigated. Those new elements can be based on free space optics or planar lightwave circuit (PLC), depending on fabrication or configuration complexity and application situation.

1.3.2.1 Multiplexers and mode converters

In WDM and PDM, filters and polarization couplers are used to multiplex distinct wavelength channels and two linear polarization states, respectively. The SDM multiplexer has to transform multiple optical paths to a single multiplexed combination of different modes.

For the MCF with single mode cores, a so-called fan-in, and fan-out technique is often used to couple each beam from N SMFs into one MCF and vice versa. By using this method, the conventional SMF can be efficiently connected to the MCF that has a hexagonal close-packed structure with -33-dB cross-talk and 0.21-dB losses [34]. This device assembles *N* individual SMF cores at a carefully arranged location with a facet that matches the core distribution of MCF. That could be made from free-space optics, fiber bundle, 3D waveguide or PLC. Among those means, the fiber bundle is the most favorable case since it provides accurate positioning, good uniformity, low insertion loss and low cross-talk. All these are achievable in a reliable way by directly splicing the device to MCF. Free-space optics is a good option for laboratory studies but it is not practical for real system integration.

Mode multiplexers are more difficult to achieve for FMF because they require controllable high order mode (HOM) generation, which is quite different from current transmitter used in WDM systems that operate in the fundamental mode. Hence, one has to transform the fundamental mode to HOMs in order to form individual channels and, furthermore, the *M* modes must also be combined at the input, as well as separated at the output of the FMF transmission link. For mode conversion, some techniques such as phase plates [40], liquid crystal on silicon (LCOS) [77] and fiber gratings [78] have been investigated. Phase plates and LCOS convert the modes by shaping the phase front to match the ones of HOMs in FMF. The former can be made from glass with a variety of thickness pattern, while the pattern of the latter is programmable on a liquid crystal array, which is more flexible. Waveguide-based mode converter can be more convenient but its design is sensitive to the operating wavelength.

Free space optic setups are widely employed for multi-beam coupling and separating. A classical implementation involves passing a beam coming from a collimator with a SMF pigtail input into a mode converter, e.g. phase plate, and combining several of these beams via beam splitters before launching into the FMF. Although it is simple to carry out, the insertion loss will increase with the number of modes and the coupling stability is sensitive to environmental perturbations. Moreover, such systems are relatively fixed, which leads to poor adaptability. Multi-plane light converters based on reflective phase plate [79] have lower insertion loss when handling a higher number of fiber modes. Other than free space optic methods, other methods that were investigated include waveguide based mode converters, multiplexers such as long period gratings and photonic lanterns that have advantages in terms of loss and complexity. The distinguishing features of several kinds of mode converters, as well as the corresponding multiplexers, are compared in Table 1.4.

Fiber based multiplexers were also used for MDM in MMF. H. Bülow et al. reported a tapered fused fiber input coupler as a multiplexer and, after transmission, the mixed modes could be retrieved without loss by MIMO processing [80]. Unlike tapered fused bundle, H. S. Chen et al. proposed a mode selective spatial filter based on a SMF array butt coupled to a MMF as the demultiplexer, due to cross-section limitations of the MMF, only three sub-channels were detected [81].

Table 1.4. Comparison of various mode conversion and multiplexing technologies

Conversion	Multiplexing	Wavelength dependence	Insertion loss	Complexity	Ref.
Phase plate	Free space	Low	High	High	[82]
Multi-plan	Free space	Low	Medium	Medium	[79]
LCOS	Free space	Low	High	High	[83]
Spot-based	Free space	Low	Medium	High	[84]
Fiber grating	Fiber based	High	Low	Low	[85]
Silicon waveguide	Free space	High	High	Medium	[86]
Photonic lantern	Fiber based	High	Low	Low	[61]

1.3.2.2 Fiber amplifier

Analogously to SMF based WDM/PDM system, long-haul transmission over MCF or FMF needs amplification as well and both lumped EDFA and distributed Raman amplifier (DRA) are potential candidates considered to provide signal amplification in SDM transmission links. Fiber optical parametric amplifier (FOPA) is a promising amplifying technique, but it is not yet mature and has some issues, e.g. requiring high nonlinear coefficient medium and high pump power, being phase and polarization sensitive, etc. These problems restrict its application on SDM system. Semiconductor optical amplifier (SOA) is an option, however mode adaptation from the optical fiber to the SOA would be challenging and could introduce severe cross-talk. Furthermore, cross-gain modulation could occur between spatial modes.

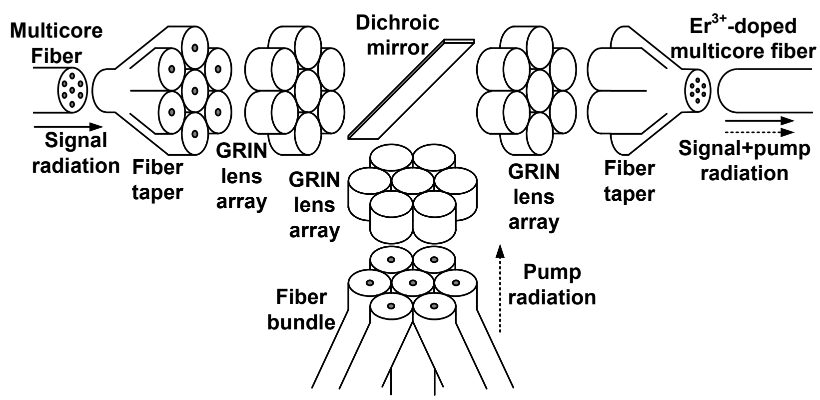

Figure 1.5. Pump signal combiner for multicore fibers [87]

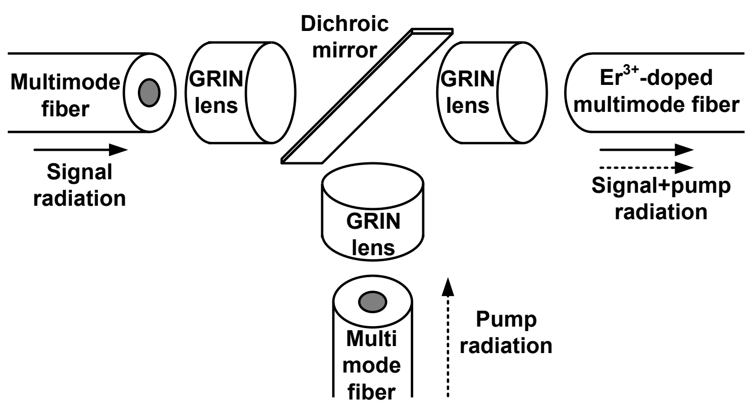

Figure 1.6. Pump signal combiner for multimode fibers [87]

As in WDM systems, cost saving and energy efficiency of SDM transmission systems can only be achieved by efficient and simultaneous amplification of the parallel channels supported by MCF and FMF. Hence, amplifiers based on such fibers must have equal performance, i.e. gain and noise figure (NF) for all cores or modes. P. Krummrich et al. proposed a general schematic to illustrate the combining methods between signal and pump for both FMF (see Figure 1.5) and MCF (see Figure 1.6) amplification. Interestingly, they point out that MCF based amplification will consume 60 % more pump power than FMF configuration [87]. Once the noise of DRA is reduced, it could become possible to implement it in SDM system. However, efficient nonlinear interactions with all modes and the resulting pump power budget would be challenging for DRA. The literature on state-of-the-art SDM amplifiers will be reviewed in detail in section 1.3.4.

1.3.2.3 Receiving data processing

The space domain is an added degree of freedom to the conventional transmission system, thus, the signal processing after the receiver will need to be upgraded. For SDM systems built on MCF, standard signal processing used in coherent detection can be adopted for each core. In FMF based SDM, a quite different situation occurs as the individual optical paths overlap spatially with each other. That introduces random mode coupling among all the guided modes more during propagation in the FMF. This coupling generates cross-talk between modes and, consequently, results in inter-channel interference on detection. Theoretically, the coupling can be classified into two regimes, i.e. weakly coupling and strong coupling. The FMF with the step-index profile is usually characterized by the former regime while graded-index profile tends to be the latter one. Ideally, the multiplexed modes would be separated at the receiving side by optical filtering only. However, due to non-uniformities along the FMF that induces perturbation and then mode coupling, MIMO must be implemented, after optical to electrical conversion, to mitigate those impairments. Actually, this signal processing technique has already been used in PDM over SMF transmission system with a 2×2 equalization matrix for two polarization states. In the present case, the MIMO will have a $M \times M$ matrix in order to process the M spatial modes of the SDM signal, if the FMF is in the strong coupling regime. On the other hand, weakly coupling FMF only requires up to 4×4 matrices for spatially degenerate modes because each mode group can be separated by the optical demultiplexer before the receiver.

The amount of DMGD in FMF need to be carefully examined when implementing MIMO processing as it determines the number of equalization taps and hence the digital signal processing complexity. Due to the DMGD existing in FMF, which is analogous to multi-path delays in wireless, the code sequences need to be equalized before the decision in receivers. The methods of equalization can be classified into three types, which are linear adaptive, semi-blind and blind equalization. The linear adaptive equalization requires some training sequences in order to know the channel state information (CSI) and those sequences will consume part of the transmission bandwidth. Additionally, if the channel state changes rapidly or frequently, more training sequences must be employed while the processing efficiency will be reduced, which affects real-time performance. That is why we cannot increase training sequences unrealistically though it is helpful in lessening bit error ratio (BER). Theoretically, if the number of taps in the equalizer is approaching infinity, ISI can be completely eliminated but of course, this is not practical in real systems. The reasonable strategy is to estimate the equalizer length of an equalizer from the DMGD and the channel coding rate. If the delays are small enough, i.e. smaller than a symbol period, the impact from that can be negligible. So that few taps in the equalizer will be used or even no equalization is needed.

As discussed above, for high-speed optical transmissions, linear adaptive equalization may not be the wisest choice. Some experimental demonstrations rather employ blind equalization with the constant-modulus algorithm (CMA), least square method (LSM) or other algorithms to estimate the channel state without data-aided mode, i.e. no training sequence is required. In addition, blind equalization is widely used in off-line DSP. In their pioneer work, R. Ryf et al. and C. Koebele et al. reported offline MIMO processing using CMA with 6×6 equalizers [19] and 2×2 equalizers plus 4×4 equalizers [41], respectively. The former experiment adopted a semi-blind method, using the data-aided LSM for training and CMA for the decision while the latter only employed a blind method and reduced MIMO processing by making sure mode coupling was contained. The impressive record, and also very sophisticated, MIMO off-line processing was recently demonstrated for 15 spatial modes MDM, driven by a 30×30 matrix frequency domain equalizer [54].

1.4 Recent progress in space-division multiplexing amplifier

Long-haul SDM transmissions, including MDM, need optical amplifiers to compensate the inevitable background losses of silica-based optical fibers. Consequently, signal regeneration in long-haul transmission is a key issue that must be resolved to implement SDM systems in the next decade. Analogously to SMF transmission links, one needs amplifiers periodically placed along a link to compensate the losses of each span. Among the various optical amplifier technologies, such as rare-earth doped fiber amplifiers, SOAs, fiber Raman amplifiers and FOPAs, the erbium-doped fiber amplifier (EDFA) is a most practical and efficient solution for SDM systems offering advantages in terms of high signal gain and low NF. In the context of SDM, amplifiers based on MC-EDFs [88], FM-EDFs [89] and multicore few-mode erbium-doped fibers (MC-FM-EDF) [90] have been demonstrated and developed. These amplifiers provide simultaneous amplification of all spatial channels with nearly identical performance in terms of gain, NF and output power. By doing so, one can achieve not only the power efficient in-line amplification but also space saving and pump source sharing. Furthermore, SDM will also be advantageous if it is compatible with routing/switching technologies. It is in this context that such amplifiers are critical. In this section, we will review the recent progress in erbium-doped fibers (EDF) and amplifier designs investigated for SDM.

The characteristics of the optical amplifiers using for SDM which are reported so far are shown in Table 1.5 and Table 1.6.

As for the few-mode erbium-doped fiber amplifier (FM-EDFA), most investigations of that amplifier focused on the EDF design, in particular, engineering of the erbium doping profile. The reason to modify the erbium doping profile is to overcome the different modes having different gains, namely mode dependent gain (MDG). Detailed discussion will be addressed in section 1.4.1 and more theoretical explanation will be given in chapter 2.

Both Cocq et al. and Kang et al. proposed the ring doping profile [91][92] which enable the model gain equalization. Inspired by the ring shape doping, researchers have tailored varieties of doping profiles such as out-ring plus center-rod [93], double-ring [93], raised-ring [94], and even so-called accurately tailored doping profile [95]. Based on those erbium doping profile design, spatial erbium-doped FMFs have been fabricated and respective amplifiers have been characterized as well, some results can be found in Table 1.5. As we can conclude from those results, the amplifier gain, NF as well as differential mode gain (DMG) still have room to be improved.

Table 1.5. Recent progress in few-mode erbium-doped fiber amplifier

Year	No. Mode	Multiplexer Mode conversion	Pump power (mW)	Fiber length (m)	Gain (dB)	NF (dB)	DMG (dB)	Equalizing Method	Ref.
2011	3	FS+LPG	200	5	~20	-	~1	Both	[96]
2012	3	FS+PP	49 +85	15	~20	-	<1	Active	[97]
2012	3	FS+LPG	250	3.5	>20	-	<2	Passive	[92]
2012	5	FS+PP	400	4	~17	<16	~6	Passive	[98]
2012	6	FS+PP	320	4.5	~19	<8	<4	Passive	[99]
2012	6	FS+PP	100	3.4	>20	-	<1	Passive	[100]
2012	3	FS+PP	158	6	>16	-	2	Passive	[101]
2013	3	FS+PP	355	4	>20	-	<1	Passive	[49]
2013	3	FS+PP	500	6	~20		~0	Passive	[102]
2013	3	FS+PP	363	4	>15	<5.5	<2.5	Passive	[103]
2015	5	FS+PP	630	3.5	>13	-	<5.7	Passive	[89]

Table 1.6. Recent progress in erbium-doped multicore fiber amplifier

Year	No. Core	Multiplexer	Pump power (mW)	Fiber length (m)	Gain (dB)	NF (dB)	λ_{Pump} (nm)	Pump scheme	Ref.
2011	7	TFB	146	15	~30	<4	980	In-core	[104]
2012	6	TFB	7600	50	>20	~6	980	Edge-cladding	[105]
2013	7	MCF	480	-	10	-	1452	Remote	[106]
2014	7	FS	8800	10	~14	<9	980	Edge-cladding	[107]
2014	7	TFB	4700	34	>20	<15	980	Side-cladding	[88]
2015	6	TFB	8000	2	>11	<12	980	Edge-cladding	[108]
2016	6	TFB	13000	2	>17	<6	980	Side-cladding	[109]

The FM-EDFA characterization setups in recent reports used a free space (FS) optics based mode multiplexer and phase plate (PP) to convert the fundamental mode into the desired mode. This technique was discussed in section 1.3.2.1. In addition, the core pumping scheme can be feasibly implemented via a dichroic mirror with such setup.

On the other hand, the MC-EDFA first demonstrated by K. Abedin et al. consisted seven cores and was core pumped by seven lasers [104]. Afterwards, in order to reduce the complexity of amplifier implementation and achieve efficient pumping, people switched from core pumping to cladding pumping. This issue will be discussed in following section 1.4.2.

1.4.1 Few-mode fiber amplifier

The most important issue concerning in FM-EDFA is the MDG (or DMG if we compare the gain difference between two modes). Note that, here the word *mode* denotes the *spatial* mode, which means that these modes have different mode field distribution in the plane perpendicular to the propagation axis. Therefore, the overlap of the signal mode profiles with both the erbium doping profile and the pump mode will vary if we assume uniform erbium doping across the fiber core and pump propagation in the fundamental mode. We usually use the DMG to quantify the performance of modes in FM-EDFA, which is represented as,

$$\mathrm{DMG}(\lambda)_{m-n} = G(\lambda)_m - G(\lambda)_n \quad m \neq n, \forall (m,n) \tag{0.1}$$

or

$$\mathrm{DMG}(\lambda)_{m-n} = \max\left\{\left|G(\lambda)_m - G(\lambda)_n\right|\right\} \quad m \neq n, \forall (m,n) \tag{0.2}$$

where G is the signal gain of mode m or n at wavelength λ in a unit of dB, m and n denote two different mode groups or spatial modes. Ideally, the DMG should be equal to zero, however, due to the MDG and loss, the DMG is non-zero unless special care is taken in the optical amplifier design. Similar to the gain flattening filter employed for equalizing the wavelength dependent gain covering the C-band, a mode gain equalizer could be implemented after the FM-EDFA to minimize the DMG, yet it is complicated. In order to mitigate the DMG, people proposed both tailoring the erbium doping profile [93] or controlling the modal content of the pump [110] methods, namely passive and active gain equalization. The former is to design an erbium doping profile that can achieve similar overlap integrals for the modes supported by the doped fiber while the latter utilizes several pumps with different mode and power level. Considering the typically doped fiber fabrication process, e.g. MCVD, a precise erbium doping profile [95] engineered to reduce the DMG is difficult to fabricate with high accuracy. On the other hand, amplifying N modes by pumping with N pump lasers operating on the corresponding modes [110] introduces flexibility on the modal gain control but at the expense of important added complexity. Consequently, the combination of active and passive equalization has been proposed to minimize the DMG and simplify the amplifier at the same time [111]. In addition, gain equalization can be done by means of the long period grating (LPG) [112] in which the pump mode is switched from one mode to the another.

Lately, another way to suppress DMG in FM-EDFA has been introduced. Rather than designing specific erbium doping profile or vary modal pump power, this solution minimizes the mode field difference by creating a ring core to guide the modes [113]. With the ring core, the mode intensity profiles are mostly located within resulting in modes with more uniform overlap factors. These fibers can further be used for the amplifications of modes carrying orbit angular momentum (OAM) or so-called vortex modes guided in optical fibers [114].

Certainly, achieving mode gain equalization by EDFA design is not the only way to achieve the target. In order to equalize the wavelength dependent gain and MDG simultaneously, the free space optical filters were investigated [115][116]. In this approach, most demonstrations use spatial light modulators to modify the incoming light and equalize both the spectral gain and modal gain.

The amplifiers mentioned above are core pumped. Cladding pumping could be considered to reduce the complexity of input coupling setup and, also potentially reduce MDG. Experimental results from [117] indicate that cladding pumped FM-EDFAs have similar performance as the core-pumped ones but offer greater potential for scaling of the number of modes.

Comparing to the multicore fiber amplifier, which has been reported with up to 19 single mode cores configuration [118], the few-mode fiber amplifier still only supports up to six modes until now [99]. The difficulty of mode gain equalization increases when adding more propagation modes. In conclusion, the mentioned methods to reduce the DMG faces many challenges such as complicated pump scheme, sophisticated erbium doping profile design, and non-adjustable gain equalization.

1.4.2 Multicore fiber amplifier

In comparison with FM-EDFA, the MC-EDFA is easier to obtain since it does not need to overcome MDG. Various forms of rare earth doped fiber amplifier for SDM, e.g. multicore amplifier [104], multi-element amplifier [119] and bundled amplifier [120], have been investigated and validated via experimental demonstrations. The difference among them is that the cores of MCF share a common cladding while the latter two have individual cladding for each core, as seen in Figure 1.7.

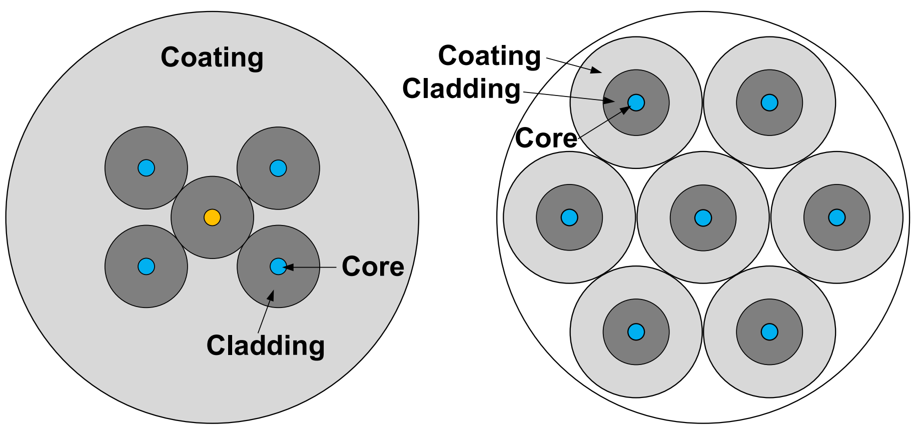

Figure 1.7. Multi-element amplifier (Left), bundled amplifier (Right)

The key point of the multicore fiber amplifier is to integrate as many doped cores as possible within a limited diameter cladding. It can be done through minimizing the core-to-core pitch, however, that pitch is limited by the cross-talk between cores. Since the cross-talk from adjacent cores which can be seen as “small signal” may be amplified in the desired core unexpectedly, one needs to pay attention to such issue. Although the bundled fiber amplifier has lower cross-talk, it cannot be combined with a cladding pumping scheme.

For the MC-EDFA, the pumping scheme is an important issue that is the subject of many considerations. Since the main advantage in implementing MC-EDFAs is that one amplifier will replace *N* parallel EDFAs, much of this advantage is lost when the pumping configuration requires *N* single-mode pump lasers with pump combiner and spatial channel demultiplexers/multiplexers at the amplifier input or output or both sides. Furthermore, the approach not only results in a complicated pump feeding architecture but also introduces extra cross-talk and even degrades the NF. [121]

Many studies on cladding pumping techniques are presently dedicated to reducing the complexity of the pumping configuration and related devices costs, towards efficient multi-core SDM amplification. With a double cladding fiber structure, cladding pumping can allow implementing low-cost and high-power multimode diode lasers at 980 nm or 1480 nm, that pump all erbium-doped cores simultaneously. However, a well-known limitation of the pump power efficiency of this method is the low pump light field overlap with the doped cores. This naturally originates from the small aggregate core area compared to large pump cladding area (assuming a uniformly distributed pump power). In this regard, the improvement of the signal and pump overlap should ideally be performed by shrinking the cladding and placing more doped cores while respecting the core-to-core pitch needed to limit cross-talk.

1.5 Objectives and methodology

Increasing the capacity of optical communication transmission system can be achieved by implementing SDM, through MCFs or FMFs. Record-breaking data transmission rates are thus achieved by combining SDM with WDM/PDM and advanced modulation format. At the heart of the long-haul transmission links based on SDM, a SDM compatible fiber amplifier is an indispensable component that must be addressed to develop viable SDM systems.

In this thesis, our objective is to investigate spatially integrated EDFAs for SDM transmission, focusing more precisely FM-EDFA and MC-EDFA. Our goal is to explore novel fiber designs that will enhance the performance of theses amplifiers. We propose means to achieve dynamic gain equalization in FM-EDFA. We also design fibers that will provide more power efficient optical amplification in MC-EDFA. The work in this thesis firstly relies on numerical simulations for optical fiber designs. The EDF parameters and EDFA performances are then characterized in the laboratory and, whenever possible, their performance is evaluated in transmission scenarios.

1.6 Thesis organization

The remainder of this thesis is organized as follows.

Chapter 2 briefly describes the EDFA theory including the amplification mechanism, energy level system as well as the wavelength dependent cross-sections. Afterwards, the numerical modeling of conventional EDFA is reviewed. Based on that general model, considerations related to the modeling of the spatially integrated amplifiers are discussed. Finally, the simulation procedure is introduced.

Chapter 3 proposes to engineer the erbium doping profile of FM-EDF to provide DMG equalization and tuning by changing the pump power at 980 nm in the fundamental mode. The designed fibers which have tailored doping profiles can be used not only in single stage amplifiers but also in double-stage ones to allow dynamic and simultaneous tuning of both gain and DMG. The performances of single stage and double-stage amplifiers based on the designed fibers, including gain, NF, and wavelength flatness, are numerically evaluated. These fibers were fabricated at the Centre for optics, photonics and lasers (COPL) and some experimental results are presented in the supplementary information section. We first present the results of the fiber chemical analysis performed to measure the distribution or the erbium ion concentration and the absorption spectrum. With these results, we have the opportunity to revisit our simulations and compared the expected performance of the designed fibers and the fabricated ones. We also present experimental measurement of the DMG of the fabricated fiber.

Chapter 4 presents the annular pump cladding design that we proposed in order to increase the pumpin efficiency. Numerical tools are implemented to not only determine the optimized fiber parameters but also to examine the performances of the amplifiers that based on these fibers. In the supplementary information section, we give more information on the pump confinement evaluated using a ray-tracing approach and we compare the results to experimental observations. These fibers were fabrication at the COPL and amplifiers were assembled with cladding pumping introduced by a tapered fiber fused to the cladding. The fiber is characterized in terms of gain, NF and cross-talk.

Chapter 5 demonstrates the first multicore few-mode erbium-doped fiber amplifier (MC-FM-EDFA) which can amplify up to 18 spatial channels simultaneously. The fiber parameters and fabrication process are described. The amplifier characterization is also presented followed by system transmission experiments simulating the transmission over 120 km of eight wavelength channels per core with each channel carrying polarization-multiplexed QPSK at 30 GBauds, for a total transmission capacity of 2.4 Tbit/s.

Chapter 6 presents a summary of the thesis and the main conclusions this thesis. We also offer some perspectives on future study.

In addition to the above mentioned work, in the course of this study, the thesis author participated and contributed to the design and characterization of several types of optical fibers for SDM. Table 1.7 below summarizes the different types of fibers as well as the publications in which these results are reported. The full list of publications also follows. This thesis focuses on the main contributions related to the design and test of novel EDF designs for spatially integrated optical amplifiers.

Table 1.7. List of fibers designed and characterized for space-division multiplexing transmissions and related publications.

Fibers	Experiment/ Design	Papers/Chapter
FM-EDFA Two-mode engineered Er^{3+} doped	Design	**J1** (Chapter 3)
	Characterization	C3
FMF Two-mode transmission fiber	Design	
	Characterization	J5, J6, C6
MC-EDFA Single mode cores with annular pump cladding (silica/air inner cladding)	Design	**J2**, C5 (Chapter 4)
	Characterization	C1 (Chapter 4)
MC-FM-EDFA Few mode cores with annular pump cladding (silica inner cladding)	Design	
	Characterization System test	**J3**, C4 (Chapter 5)
MC-EDFA Single mode cores with conventional double-cladding	Design	
	Characterization System test	J4, C2

The additional journal papers are:

J1. **C. Jin**, B. Ung, Y. Messaddeq, S. LaRochelle, "Tailored modal gain in a multi-mode erbium-doped fiber amplifier based on engineered ring doping profiles," Proc. SPIE 8915, *Photonics North 2013*, 89150A (2013)

J2. **C. Jin**, B. Ung, Y. Messaddeq, S. LaRochelle, "Annular-cladding erbium doped multicore fiber for SDM amplification," *Opt. Express*, Vol. **23**, No. **23**, pp. 29647-29659 (2015)

J3. H. Chen, **C. Jin**, B. Huang, N. K. Fontaine, R. Ryf, K. Shang, N. Grégoire, S. Morency, R.-J. Essiambre, G. Li, Y. Messaddeq, S. LaRochelle, "Spatially Integrated Optical Fiber Amplifier," Submitted to *Nature Photonics* (Accepted as the revised version) (2016)

J4. H. Chen, N. K. Fontaine, R. Ryf, **C. Jin**, B. Huang, K. Shang, R.-J. Essiambre, L. Wang, T. Hayashi, T. Nagashima, T. Sasaki, Y. Messaddeq and S. LaRochelle, "Demonstration of Cladding-Pumped Six-Core Erbium-Doped Fiber Amplifier," *J. Lightwave Technol.*, Vol. **34**, No. **8**, pp.1654-1660 (2016)

J5. R. Gabet, E. Le Cren, **C. Jin**, M. Gadonna, B. Ung, P. Sillard, H. G. Nguyen, Y. Jaouën, M. Thual and S. LaRochelle, "Complete dispersion characterization of Few Mode Fibers by OLCI Technique," *J. Lightwave Technol.*, Vol. **33**, No. **6**, pp.1155-1160 (2015)

J6. L. Wang, **<u>C. Jin</u>**, Y. Messaddeq and S. LaRochelle, “Microwave Interferometric Technique for Characterizing Few Mode Fibers,” *Photon. Technol. Lett.*, Vol. **26**, No. **17**, pp.1695-1698 (2014)

The additional conference papers are:

C1. **<u>C. Jin</u>**, H. Chen, B. Huang, K. Shang, N. K. Fontaine, R. Ryf, R.-J. Essiambre, B. Ung, Y. Messaddeq, S. LaRochelle, “Characterization of Annular Cladding Erbium-Doped 6-Core Fiber Amplifier,” *OFC 2016*, Tu2I.3 (2016)

C2. **<u>C. Jin</u>**, B. Huang, H. Chen, N. K. Fontaine, R. Ryf, R.-J. Essiambre, B. Ung, Y. Messaddeq, S. LaRochelle, "Investigation of the inter-core cross-talk of cladding pumped double-clad six-core erbium doped fiber amplifier," *CLEO 2016*, STu1F.7 (2016)

C3. B. Huang, H. Chen, N. K. Fontaine, **<u>C. Jin</u>**, K. Shang, R. Ryf, R.-J. Essiambre, B. Ung, Y. Messaddeq, S. LaRochelle, G. Li, “Characterization of Space-Division Multiplexing Amplifiers Using a Swept Wavelength Coherent Reflectometer,” *OFC 2016*, W4F.2 (2016)

C4. **<u>C. Jin</u>**, B. Huang, K. Shang, H. Chen, R. Ryf, R.-J. Essiambre, N. K. Fontaine, G. Li, L. Wang, Y. Messaddeq, S. LaRochelle, “Efficient Annular Cladding Amplifier with Six, Three-Mode Cores,” *ECOC 2015*, PDP.2.1 (2015)

C5. **<u>C. Jin</u>**, B. Ung, Y. Messaddeq, S. LaRochelle, “Annular Cladding Erbium-Doped Multi-Core Fiber for SDM Amplification,” *CLEO 2015*, JW2A.95 (2015)

C6. R. Gabet, E. Le Cren, **<u>C. Jin</u>**, M. Gadonna, B. Ung, Y. Jaouën, M. Thual, S. LaRochelle, “Characterization of Few Mode Fibers by OLCI Technique,” *ECOC 2014*, Th.1.4.2 (2014)

Chapter 2

Erbium-doped Fiber Amplifier Theory and Modeling

Abstract

In Chapter 1, we described one of the key elements, i.e. the optical fiber amplifiers, for SDM transmission systems, in particular for long-haul optical fiber links. The emerging SDM technique requires the introduction of the spatial domain in all subsystems including optical fiber amplifiers that must be spatially integrated to ensure compatibility with transmission fibers, reduce volume and improve power efficiency. These new optical amplifiers require modifications to the classical numerical model that describe signal and pump power propagation in the doped fiber.

In this chapter, the basic theory of EDFA will be first reviewed. We discuss the energy levels of trivalent erbium ions (Er^{3+}) in silica and discuss their radiative properties. Following, we introduce the conventional EDFA model with coupled equations describing the signal amplification, pump absorption, and amplified spontaneous emission (ASE) generation, as well as population rate equations of Er^{3+}. Then we describe how the model must be modified in the case of MCF and MMF based amplification.

2.1 Fundamentals of erbium-doped fiber amplifiers

The optical amplification mechanism in rare-earth doped fiber amplifier is based on stimulated emission. An optical fiber amplifier needs an external optical pump to enable population inversion in the gain medium consisting of active ions that are present in the host glass or crystal. Usually, in the case of an optical fiber amplifier, the active ions are rare-earth elements such as erbium, ytterbium, thulium, etc. Among these elements, Er^{3+} is particularly well suited for optical fiber communications operating in the C-band and L-band. Indeed, Er^{3+} efficiently absorbs pump photons at 980 nm or 1480 nm and will subsequently emit lower energy photons in the wavelength range from 1510 nm to 1610 nm, thus covering both the C- and L-bands. The emission is either spontaneous or stimulated which, in the latter case, can result in amplification of co-propagating or counter-propagating signal photons in the process.

2.1.1 Energy levels

A critical property of amplification based on stimulated emission is the energy level diagram of the gain medium. Figure 2.1 illustrates a portion of Er^{3+} energy levels, from the lower level $^4I_{15/2}$ to the higher level $^4F_{7/2}$.

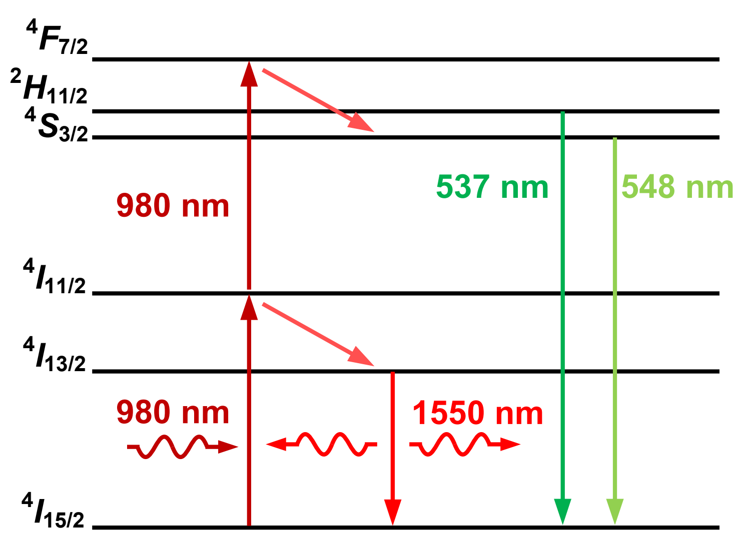

Figure 2.1. Part of Er^{3+} energy level, from $^4I_{15/2}$ to $^4F_{7/2}$

The Er^{3+} has multiple energy levels, and, therefore, the trivalent ions can absorb photons at several different wavelengths. The detailed absorption spectrum of the gain medium is however also influenced by the host glass material. A typical Er^{3+} absorption spectrum for the Al-Ge-P co-doped silica host glass is shown in Figure 2.2.

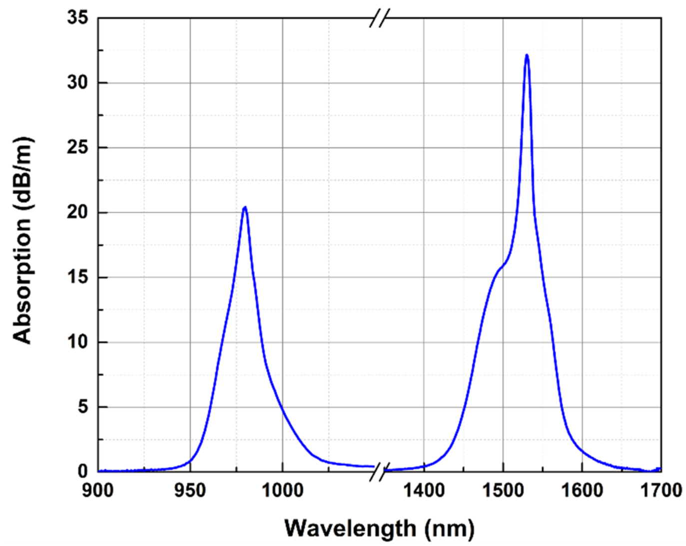

Figure 2.2. Typical erbium absorption spectrum of Al-Ge-P co-doped silica glass

Accordingly, 980-nm and 1480-nm pump wavelengths can be used to excite the erbium ions from the ground level, $^4I_{15/2}$, to the upper level and produce the population inversion between these levels. The different excitation paths, through 980-nm and 1480-nm pumping, are shown in Figure 2.3. The ion that absorbs a 1480-nm pump photon directly transits to the metastable level ($^4I_{13/2}$) and then decays back to the ground level ($^4I_{15/2}$) by stimulated emission if there is the presence of a signal photon within the wavelength range 1500 ~ 1600 nm. When pumping at 980 nm, on the contrary, the ion first transits to the excited level ($^4I_{11/2}$), but then quickly decays to the metastable level with about 1-μs non-radiative relaxation time. The rest of the process is similar to that of the 1480-nm pumping. The relatively long relaxation time (low spontaneous emission decay rate) in the metastable level allows the population inversion to build up when there are sufficient pump photons.

Since the $^4I_{11/2}$ is not the highest level in the erbium energy level system, additional absorption processes, which are the so-called excited state absorption (ESA), may also occur when the ion is in an excited state. For example, the absorption originating from the $^4I_{11/2}$ level to higher levels will occur at various wavelengths including 514 nm, 630 nm, 715 nm, 790 nm, 850 nm, 1140 nm and in particular 980 nm. The 980-nm pump power is continually absorbed by ions excited to the $^4I_{11/2}$ level that then transition to the $^4F_{7/2}$ level as shown in Figure 2.1. The ion may non-radiatively decay to the $^4S_{3/2}$ level and then emit 548-nm light via radiative relaxation. That *green emission* is the reason why we sometimes can see a green light when the EDF is pumped by 980-nm laser source.

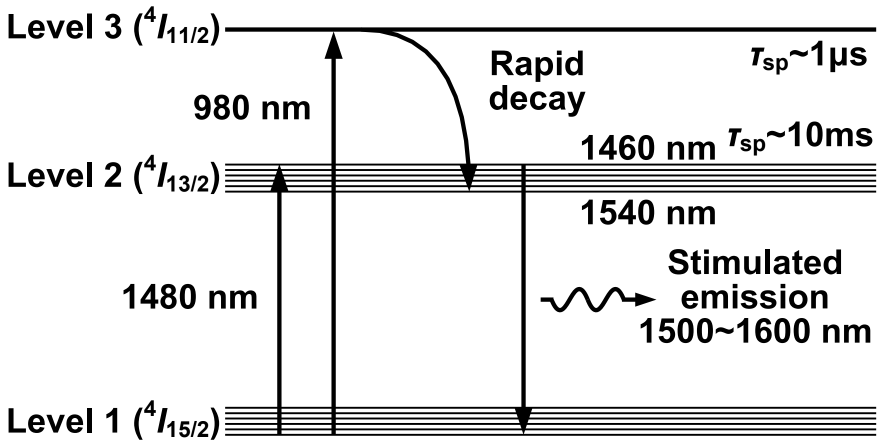

Figure 2.3. Three-level energy diagram for Er^{3+} in silica host glass showing pump bands at 1480 nm and 980 nm and emission from metastable level 2 to ground state level 1.

2.1.2 Cross-section

At the microscopic level, the energy exchange among energy levels relies on erbium ion transition processes between energy levels that are governed by transition probabilities, or, in other words, transition rates. The absorption and emission processes have specific rates that are quantified by their cross-sections, i.e. absorption cross-section and emission cross-section, respectively.

Assuming a two-level system formed by level 1 and 2 in Figure 2.3, with corresponding energies of E_1 and E_2 for these levels. A photon with angular frequency ω such that its energy is $\hbar\omega = E_2 - E_1$, will have a probability of absorption (from level 1 to level 2) or emission (from level 2 to level 1) proportional to the cross-section σ_{12} and σ_{21}, and to the incident light intensity. In this system, the transition rate for a number of photons be absorbed at frequency ω is expressed as,

$$N_{\text{abs}} = \sigma_{12}\phi(\omega) \tag{2.1}$$

where $\varphi(\omega)$ is the photon flux present, i.e. the number of photons per area per time. Accordingly, by multiplying N_{abs} by the photon energy $\hbar\omega$, the amount of incident light power absorbed is given by,

$$P_{\text{abs}} = \sigma_{12} I_{\text{in}} \tag{2.2}$$

where I_{in} is the incident light intensity. For the reverse process, similarly, the amount of simulated light power is given by,

$$P_{\text{em}} = \sigma_{21} I_{\text{in}} \tag{2.3}$$

If level 2 has an ion population of N_2 while that one of level 1 is N_1, when light passes through the gain medium the power changes according to,

$$\Delta P = P_{\text{em}} - P_{\text{abs}} = (N_2\sigma_{21} - N_1\sigma_{12}) I_{\text{in}} \tag{2.4}$$

Since the erbium ion levels $^4I_{13/2}$ and $^4I_{15/2}$ have a number of sub-levels, the transition cross-sections between level 1 and 2 are obtained from the weighted summation of sub-level cross-sections weighted by their respective populations,

$$\sigma_{12}(\nu) = \sum_{i,j} m_{1i}\sigma_{1i,2j}(\nu) \tag{2.5}$$

$$\sigma_{21}(\nu) = \sum_{i,j} m_{2j}\sigma_{2j,1i}(\nu) \tag{2.6}$$

where m_{1i} and m_{2j} are the sub-level populations normalized to the level 1 population N_1 and level 2 population N_2, respectively. The Boltzmann distribution is employed to determine the population distribution among sub-levels. For example, for level 1,

$$m_{1i} = \frac{\exp\left(E_{1i} - E_{11}\right)}{\sum_{i=1}^{g_1} \exp\left[-\left(E_{1i} - E_{11}\right)/k_{\mathrm{B}}T\right]} \tag{2.7}$$

where E_{1i} is the energy of i^{th} sub-level of level 1, g_1 is the number of sub-levels, k_{B} and T denote the Boltzmann constant and temperature in Kelvins, respectively.

For a photon with an energy of $h\nu$, according to the above equations, the relationship between absorption and emission cross-sections is

$$\sigma_{21}\left(\nu\right) = \sigma_{12}\left(\nu\right) \frac{N_1}{N_2} \exp\left[\left(E_{12} - h\nu\right)/k_{\mathrm{B}}T\right] \tag{2.8}$$

where E_{12} is the energy separation between level 1 and level 2.

The population for either level 1 or level 2 is rapidly redistributed among sub-levels at room temperature, i.e. about 298 K. That phenomenon is the so-called thermalization and its time constant is typically of the order of ps. Such a fast redistribution contributes to the homogeneous broadening behavior of erbium ion transitions at room temperature.

Practically, the wavelength dependent absorption cross-section can be estimated via the absorption spectrum since,

$$\alpha\left(\lambda\right) = \rho\Gamma\left(\lambda\right)\sigma_{12}\left(\lambda\right) \tag{2.9}$$

where $\alpha(\lambda)$ is the power absorption coefficient, ρ is the erbium ion doping concentration, and $\Gamma(\lambda)$ is the light intensity overlap factor with the erbium ion distribution.

After determining the absorption cross-section, the emission cross-section can be obtained by an empirical equation, namely the McCumber relation [122],

$$\sigma_{21}\left(\nu\right) = \sigma_{12}\left(\nu\right) \exp\left[\left(\varepsilon - h\nu\right)/k_{\mathrm{B}}T\right] \tag{2.10}$$

where ε represents the average transition energy between two levels in particular, for erbium ions, it is mean transition energy between $^4I_{13/2}$ and $^4I_{15/2}$.

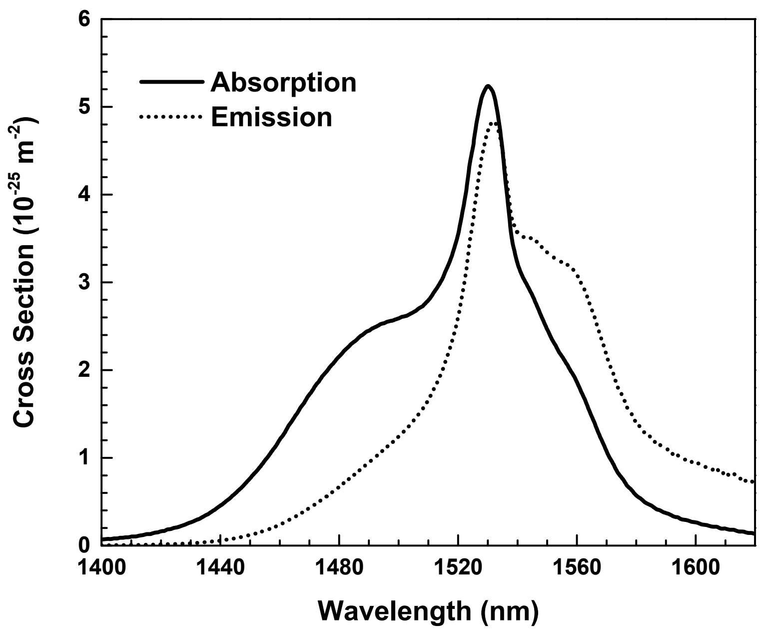

Figure 2.4. Absorption and emission cross-sections of erbium ion around 1550-nm window

Figure 2.4 shows typical absorption and emission cross-sections of erbium ions incorporated in an Al-Ge-P doped silica host glass for wavelengths around 1.5 μm.

2.2 Numerical modeling of the amplifier

To model the EDFA operation, one first needs to specify the amplifier energy level system to be considered, namely a two-, three-, four- or even five-level systems (see Figure 2.5). For erbium ions, the number of energy levels depends on whether ESA can be neglected and on the pump wavelength. The erbium ion pumped at 980 nm is treated as a three-level system. The ions transit to level 3 driven by the power absorbed from the 980-nm pump, and then immediately decay to level 2, which is the so-called metastable level, without emitting radiation. Finally, the ions come back to level 1 with spontaneous emission or stimulated emission. In this process, approximately half (depending on the wavelength) of the ion population has to be excited to level 2, otherwise, the gain medium behaves as an absorber at the signal wavelength. In the modeling, the energy system can be simplified to a two-level system owing to the fast (quasi-instantaneous) nonradioactive decay from level 3 to level 2.

On the other hand, the 1480-nm light pumping scenario corresponds to a two-level system. In this case, the large stark-splitting of the energy levels combined to the fast thermalization enables the two-level system to work as an amplifier when using 1480-nm intra-band pumping. Note that stimulated emission occurs at the pump wavelength, i.e. 1480 nm, which may deplete the upper-level population and the resulting lower population inversion will degrade the NF. In order to establish the numerical modeling which can describe amplification in multicore and multimode fibers, we start from a basic two-level model of EDFAs.

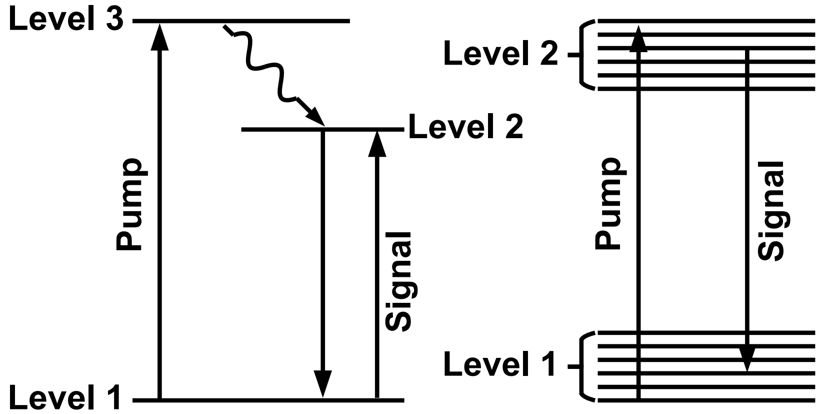

Figure 2.5. Schematic representation of three- and two-level systems

2.2.1 Power propagation evolution and atomic rate equations

The conventional EDFA model used for simulating signal gain as well as NF performance has been described in [123][124] and consists of a set of equations that include ion population rate equations and power propagation evolution equations. For a two-level system, the population rate equations are,

$$\frac{dN_2}{dt} = \sum_k W_{12k} N_1 - \sum_k W_{21k} N_2 - N_2/\tau \tag{2.11}$$

$$N_{\mathrm{T}} = N_1 + N_2 \tag{2.12}$$

where N_1 and N_2 are erbium ions population densities of the ground state (level 1) and excited state (level 2) of the two-level system, respectively. N_T is total erbium ions density which is assumed equal to the doping concentration and τ is the lifetime of the metastable level representing the spontaneous decay from the upper excited level to the lower ground state one. The W_{ijk} symbols represent the transition rates from levels i to level j caused by the power of the k^{th} propagating wavelength channel, where subscripts k indicate either pump, signal or an ASE band. We consider the steady state condition such that

$$\frac{dN_2}{dt} = 0 \tag{2.13}$$

and the upper level, i.e. excited state, ion population density can be expressed as,

$$N_2 = \frac{\sum_k W_{12k}}{\sum_k W_{12k} + \sum_k W_{21k} + 1/\tau} N_\mathrm{T} \tag{2.14}$$

The transition rates W_{ijk} for the k^{th} channel are expressed as follows,

$$W_{12k} = \frac{\sigma_{\mathrm{a}k} I_k}{h\nu_k} \tag{2.15}$$

$$W_{21k} = \frac{\sigma_{\mathrm{e}k} I_k}{h\nu_k} \tag{2.16}$$

σ_{ek} and σ_{ak} are, respectively, the wavelength dependent emission and absorption cross-sections of the k^{th} propagating wavelength channel.

To simplify the calculations, we introduce the normalized beam intensity which has units of inverse area,

$$I_{\mathrm{n}k}(x, y) = I_k(x, y, z)/P_k(z) \tag{2.17}$$

where P_k is total power at position z of the k^{th} channel; $I_{\text{n}k}$ is the normalized beam intensity profile of the k^{th} channel such that,

$$\iint_{A_{\text{fiber}}} I_{\text{n}k} dA_{\text{fiber}} = 1 \tag{2.18}$$

where A_{fiber} is the fiber transverse cross-section area.

Thereafter, considering that the studied fiber transverse cross-section has a cylindrical symmetry, we can use polar coordinates and Equations (2.15) and (2.16) become,

$$W_{12k} = \frac{\sigma_{\text{a}k} I_{\text{n}k}(r,\varphi) P_k(z)}{h\nu_k} \tag{2.19}$$

$$W_{21k} = \frac{\sigma_{\text{e}k} I_{\text{n}k}(r,\varphi) P_k(z)}{h\nu_k} \tag{2.20}$$

Accordingly, the lower level erbium ion population density is expressed as,

$$N_1(r,\varphi,z) = \frac{\sum_k W_{21k} + 1/\tau}{\sum_k W_{12k} + \sum_k W_{21k} + 1/\tau} N_{\text{T}}(r,\varphi,z) \tag{2.21}$$

The rate equations describe the energy exchange between the upper level and lower levels in terms of erbium ion population densities. One now also needs to describe how the optical power of each channel evolves along the fiber. The propagation of the pump, signal, and ASE power is described by,

$$\begin{aligned} \frac{dP_k(z)}{dz} &= u_k \sigma_{\text{e}k} \iint_{A_{\text{Er}}} I_{\text{n}k} N_2(z) dA_{\text{Er}} \cdot \left[P_k(z) + mh\nu_k \Delta\nu_k \right] \\ &\quad - u_k \sigma_{\text{a}k} \iint_{A_{\text{Er}}} I_{\text{n}k} N_1(z) dA_{\text{Er}} \cdot P_k(z) - \alpha_k P_k(z) \end{aligned} \tag{2.22}$$

where u_k indicates the propagation direction of the channel, more specifically $u_k = 1$ for a pump co-propagating with the signal while $u_k = -1$ for a counter-propagating pump; h is the

Planck constant, v_k is the center frequency and Δv_k the bandwidth of the k^{th} channel, and $mhv_k\Delta v_k$ represents the contribution of ASE where m is usually 2 due to the two linear orthogonal polarization states supported by the optical fiber; α_k is the intrinsic background loss coefficient.

Again, in polar coordinates, the Equation (2.22) is rewritten as,

$$\begin{aligned}\frac{dP_k(z)}{dz} &= u_k\sigma_{\mathrm{e}k}\int_0^{2\pi}\int_0^{\infty} I_{\mathrm{n}k}(r,\varphi)N_2(r,\varphi,z)rdrd\varphi\cdot\left[P_k(z)+mhv_k\Delta v_k\right] \\ &\quad -u_k\sigma_{\mathrm{a}k}\int_0^{2\pi}\int_0^{\infty} I_{\mathrm{n}k}(r,\varphi)N_1(r,\varphi,z)rdrd\varphi\cdot P_k(z)-\alpha_k P_k(z)\end{aligned} \tag{2.23}$$

2.2.2 Overlap factor discretization

In the equations given above to describe the amplifier operation, one of the important terms is the spatial overlap integral

$$\int_0^{2\pi}\int_0^{\infty} I_{\mathrm{n}k}(r,\varphi)N_i(r,\varphi,z)rdrd\varphi \quad i=1,2 \tag{2.24}$$

which defines the degree of interaction between the propagating k^{th} channel and erbium dopant. If we introduce the normalized ion population density,

$$N_{\mathrm{n}}(r,\varphi)=N_i(r,\varphi)/\bar{N} \quad i=1,2 \tag{2.25}$$

where N_i is either upper level or lower level population density and $\bar{N}$ is the average population density. Then Equation (2.24) is usually simplified by using an overlap factor,

$$\Gamma_k=\int_0^{2\pi}\int_0^{\infty} I_{\mathrm{n}k}(r,\varphi)N_{\mathrm{n}}(r,\varphi)rdrd\varphi \quad i=1,2 \tag{2.26}$$

where Γ_k = C, C$\in$[0,1], i.e. the overlap factor is a dimensionless parameter whose value ranges from 0 to 1. To simplify numerical simulations, overlaps integrals in SMF amplifiers are often calculated only once by assuming that the level populations are uniformly excited and, therefore, the transverse distribution follow the normalized erbium ion doping distribution $N_\rho(r,\varphi)$

$$\Gamma_k = \int_0^a \int_0^{2\pi} I_{\mathrm{n}k}(r,\varphi) N_\rho(r,\varphi) r dr d\varphi \tag{2.27}$$

where a is the core radius (assuming that the doping area is the same as the core area). $N_\rho(r,\varphi)$ is the erbium ion doping distribution of transverse cross-section, usually, it is normalized to the maximum dopant concentration, ρ.

2.2.3 Modeling of few-mode fiber amplifiers

In the case of MMFs, uniform population excitation across the transverse fiber area can no longer be assumed. For each mode, the normalized intensity profile $I_{nk}(r,\varphi)$ defined in Equation (2.17) can be rewritten as,

$$I_{\mathrm{n}k}(r,\varphi) = \frac{\psi_{k,lm}(r,\varphi)}{\int_0^\infty \int_0^{2\pi} \psi_{k,lm}(r,\varphi) r dr d\varphi} \tag{2.28}$$

where $\psi_{k,lm}(r,\varphi)$ denotes the intensity profile of the lm mode of channel k. In this thesis, we will limit our analysis to the LP modes in a weakly guiding fiber supporting a few mode groups. If all modes of a mode group are simultaneously excited, the resulting intensity profile will be azimuthally symmetric and will only depend on r. In Chapter 3, when we model MMF amplifiers, we will introduce the radial dependence of the erbium ion populations by discretizing the transverse fiber areas into multi-layer. For each layer, we will calculate mode overlaps and erbium ion populations. In the case of MMF, due to the presence of several modes with different mode distributions, the erbium ion population is no longer uniformly excited across the core. Consequently, the overlap of the intensity with the ion population depends on the transverse coordinates (r,φ), the interaction efficiency between the doped area and optical mode (i.e. how much power will be then involved in energy transition, or in the amplification), can be calculated by evaluating the integral in several rings.

2.2.4 Simulation procedure

As part of this thesis, we develop an in-house EDFA simulation software to investigate fiber designs of few-mode and multicore fiber amplifiers. The numerical simulations are based on the EDFA modeling described in the preceding sections and uses a fourth-order Runge-Kutta method, which is a numerical tool often used to solve ordinary differential equations (ODEs). The software, in Matlab® language, provides signal gain, as well as the NF. The program flow chart is depicted in Figure 2.6.

Many numerical techniques are required to either obtain accurate results or reduce the computing time. The evaluation of numerical convergence is an example. The convergence criterion is determined by,

$$P_{\mathrm{s,out}}\left(\mathrm{iter.}\,j\right) - P_{\mathrm{s,out}}\left(\mathrm{iter.}\,j-1\right) < \mathit{Tolerated\ error} \tag{2.29}$$

where the $P_{\mathrm{s,out}}(\mathrm{iter.}\,j)$ is the output signal power for the j^{th} iteration. Equation (2.29) indicates that when the difference between two conductive iterations is less than the given *Tolerated error*, the simulation loop stops. Moreover, sometimes the convergence process is not monotonically decreasing. In fact, such process usually experiences a period of numerical fluctuations. Therefore, a given number of iterations are needed in order to reach the convergence at the steady state in which each numerical difference of two conductive iterations is below the tolerated error threshold.

2.3 Summary

In this chapter, starting from the basic mechanism of the EDFA operation, we introduced some key parameters of the amplification principle, such as energy levels, cross-sections, etc. The former reveals how energy is exchanged between the propagating light channels and the erbium ions, as well as within the ion itself. While the latter is an intrinsic property, which is influenced by the fiber host glass component, that describes the ions affinity for light absorption and emission.

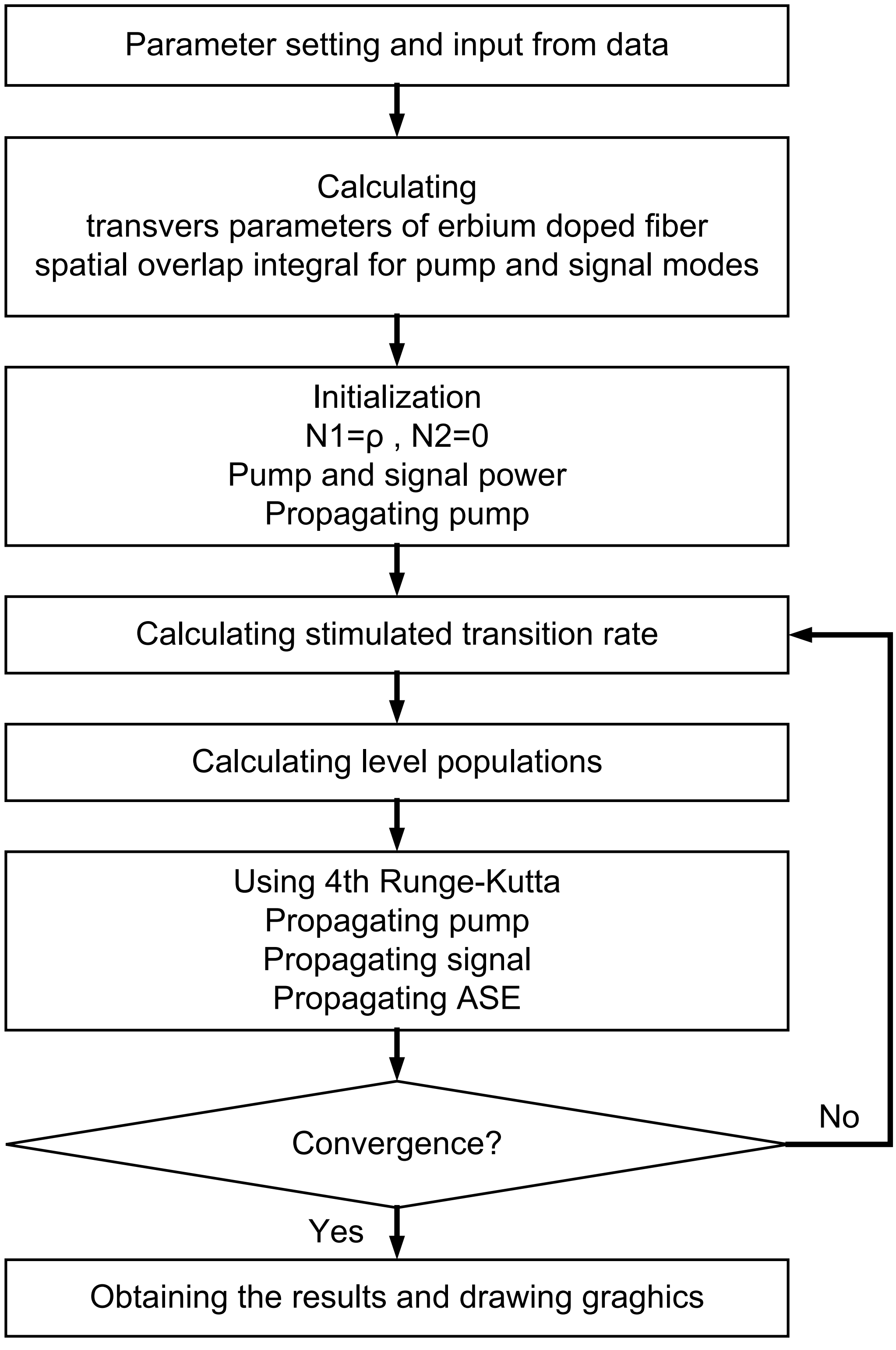

Figure 2.6. Flow chart of algorithm for amplifier simulation in Matlab®

Subsequently, the classical numerical modeling of EDFA and its corresponding sets of equations was reviewed. In Chapter 3, we will examine how this model needs to be modified to describe amplification in FM-EDFs. More specifically, we will introduce variations in the transverse plane by separating the area into rings. We also discussed how the overlap factor of the pump channel is modified when using a cladding pumping configuration. This will be useful in the modeling of multi-core amplifiers presented in Chapter 4.

Finally, we briefly sketched the algorithm used for the numerical simulations that are performed using the well-known fourth-order Runge-Kutta method was employed in order to solve the ODEs. In addition, the convergence of the numerical solution was discussed.

Chapter 3

Tailored Modal Gain in a Multimode Erbium-doped Fiber Amplifier Based on Engineered Ring Doping Profiles

Abstract

Various SDM schemes are currently investigated as a way to overcome the capacity limit of data links. We here focus on MDM in a MMF. Towards long-haul data transmission, for which signal amplification is a key enabling component, we investigate a simple approach to precisely control the MDG between the co-propagating LP_{01} and LP_{11} modes of a multimode erbium-doped fiber amplifier (MM-EDFA) by engineering a multi-ring doping profile. In practice, the MDL of the few-mode transmission fiber must be taken into account in order to equalize the gain for all modal channels. In a step towards practical implementation of MM-EDFA for long-haul SDM, we extend the single ring doping approach to incorporate multi-ring and multi-level doping. Through numerical simulations we study the optimization of the width and doping level of each ring so as to control the MDG. We further discuss the possibility of modal gain equalization through zero-differential modal gain (ZDMG) points in a single stage MM-EDFA, or via tuning of pump powers in a dual-stage MM-EDFA configuration.

Résumé

Divers scénarios de régimes de SDM sont actuellement étudiés comme moyen de surmonter la limite de capacité des fibres optique pour la transmission de donnée à haut débit. Nous nous concentrons ici sur le MDM dans une MMF. L'amplification du signal est un élément clé des applications de transmission de données sur de longues distances. Nous étudions une approche simple pour contrôler avec précision la variation du MDG, plus spécifiquement entre les modes LP_{01} et LP_{11} dans un amplificateur qui supporte un petit nombre de modes (MM-EDFA). L'approche consiste à faire la conception d'un profil de dopage ayant une variation radiale, par exemple des anneaux multiples. Dans la pratique, les pertes modales doivent être prises en compte afin d'égaliser le gain pour tous les modes. Dans une étape vers la mise en œuvre pratique des MM-EDFAs pour le SDM, nous étendons l'approche de dopage en anneau simple aux anneaux multiples et au dopage à plusieurs niveaux. Grâce à des simulations numériques, nous étudions l'optimisation du niveau de chaque anneau de manière à contrôler le MDG. Nous discutons en outre la possibilité de l'égalisation du gain modal dans un MM-EDFA à un seul étage ou via le réglage des puissances de pompage dans une configuration MM-EDFA à double étage.

3.1 Introduction

The exponential growth of data traffic in recent years has by now practically exhausted all known means (e.g. wavelength and polarization multiplexing, and higher-order modulation formats) of increasing the capacity limit in SMFs [125]. Spatial multiplexing is seen as a promising route to overcome the expected '*capacity crunch*' while minimizing the energy cost per bit sent [87][126]. This is made possible by introducing a new degree of freedom through which one can multiplex several data links within a single fiber strand by either one of two general schemes: a multimode fiber - where each eigenmode corresponds to an independent channel [70][127][128][129] - or in a multi-core fiber where each core represents a link [130][131] The present work relates to the former embodiment known as MDM.

Also at the heart of any practical implementation of spatial multiplexing schemes for long-haul transmission, lies the development of high-performance and cost-effective inline optical amplifiers [87]. The difficulty of achieving equal gain across all channels in a MM-EDFA has been discussed in [132][74][94][95]. To circumvent this problem, active methods based on controlling the input pump conditions have been proposed [110][133][134]. However, active methods relying on the injection of multiple pumps in different modes and a delicate control of their relative strengths can potentially increase the system complexity, hence the cost-per-bit.

A passive method for gain equalization based on a ring-doping approach [e.g. Figure 3.1(a)] was met with promising early results: 20-dB gain with a DMG of less than 3 dB has been demonstrated for the LP_{11} and LP_{21} mode groups in [100] and for the LP_{01} and LP_{11} mode groups in [92], while 12.5-dB gain with 1-dB gain excursion between the LP_{01} and LP_{11} modes was demonstrated in [103]. The same method was recently extended to include a small doped core in the center of a doped ring MM-EDFA in which four signal modes (LP_{01}, LP_{11}, LP_{21}, LP_{02}) were predicted to achieve gains over 20 dB using two pump modes (LP_{01} and LP_{41}), although noise and modal coupling were neglected in the analysis[135].

In this chapter we further extend this passive approach towards multiple doped rings [see Figure 3.1(b-c)] and demonstrate superior control over the MDG of a MM-EDFA supporting two signal mode groups (LP_{01} and LP_{11}) at 1550 nm and with -13-dBm input power each, while using a single LP_{01} 980-nm pump. Our numerical analysis fully takes into account the effect of ASE noise and predicts over 20-dB average gain for both mode groups with a DMG less than 1 dB and average NFs below 5 dB. Our analysis suggests that the proposed method should allow precise control over the gain equalization, thus opening a variety of practical working points for MM-EDFAs. We also discuss how such multi-ring multi-level doped fibers can be used in a two-stage EDFA configuration so as to enable dynamic control of the MDG via tuning of the input pump power in each stage. Finally, an argument is made towards multi-ring doped profiles for managing MDG in MM-EDFAs supporting more than two mode groups, and OAM modes.

3.2 Theory and multi-ring doping profiles

The operation of an EDFA can be described, as is well known, by a set of power propagation equation and rate equation [123]. The former describes the power intensity, either pump or signal, evolution through the doped fiber; while the latter updates the population densities of upper and lower level along the doped fiber, as follows:

$$\begin{aligned}\frac{dP_k(z)}{dz} &= u_k\sigma_{\mathrm{e}k}\int_0^{2\pi}\int_0^{\infty} i_k(r,\varphi)N_2(r,\varphi,z)\cdot rdrd\varphi\cdot\left[P_k(z)+mh\nu_k\Delta\nu_k\right] \\ &\quad -u_k\sigma_{\mathrm{a}k}\int_0^{2\pi}\int_0^{\infty} i_k(r,\varphi)N_1(r,\varphi,z)\cdot rdrd\varphi\cdot P_k(z)-\alpha_k P_k(z)\end{aligned} \tag{3.1}$$

$$N_2(r,\varphi,z)=\frac{\sum_m \dfrac{\sigma_{\mathrm{a}k}I_k(r,\varphi)P_k(z)}{h\nu_k}}{\sum_k \dfrac{\sigma_{\mathrm{a}k}I_k(r,\varphi)P_k(z)}{h\nu_k}+\sum_k \dfrac{\sigma_{\mathrm{e}k}i_k(r,\varphi)P_k(z)}{h\nu_k}+\dfrac{1}{\tau}}\cdot N_{\mathrm{T}}(z) \tag{3.2}$$

where k indicates the pump, signal or ASE channel, u_k denotes the propagation direction (1 or -1), $\sigma_{\mathrm{e}k}$ and $\sigma_{\mathrm{a}k}$ are respectively the emission and absorption cross-sections, $I_k(r,\varphi)$ is the normalized beam intensity profile, N_2 and N_1 are the upper and lower population level densities, m indicates the number of polarization modes, variables ν_k and $\Delta\nu_k$ designate respectively the optical frequency and the ASE channel bandwidth centered at ν, h is the Planck constant, α_k stands for the background loss and τ is the lifetime of the metastable level of the erbium ions. Conservation is locally enforced on the population densities, $N_T = N_1+N_2$, where N_T is total erbium ion population density.

In our analysis, we considered a SI-FMF that supports two modes group: LP_{01} and LP_{11}. To account for the large dissimilarity in the field distributions of the modes and the ensuing spatial mode competition, the transverse cross-section in our numerical model was discretized using the multi-layer approach described in [103][136]. Based on this model, we derived a new set of equations to describe our MM-EDFA:

$$\begin{cases} \dfrac{dP_{\mathrm{p}}(z)}{dz} = -\sigma_{\mathrm{ap}}\left(\sum_K N_{1,K}\Gamma_{\mathrm{p},K}\right)P_{\mathrm{p}}(z) \\ \dfrac{dP_{\mathrm{s},m}(z)}{dz} = \left(\sigma_{\mathrm{es}}\sum_K N_{2,K}\Gamma_{(\mathrm{s},m),K} - \sigma_{\mathrm{as}}\sum_K N_{1,K}\Gamma_{(\mathrm{s},m),K}\right)P_{\mathrm{s},m}(z) \\ \dfrac{dP_{\mathrm{i},m}(z)}{dz} = \left(\sigma_{\mathrm{i}}\sum_K N_{2,K}\Gamma_{(\mathrm{i},m),K} - \sigma_{\mathrm{i}}\sum_K N_{1,K}\Gamma_{(\mathrm{i},m),K}\right)P_{\mathrm{i},m}(z) \\ \qquad\qquad + \sigma_{\mathrm{i}}\left(\sum_K N_{2,K}\Gamma_{(\mathrm{i},m),K}\right)2h\nu_{\mathrm{i}}\Delta\nu_{\mathrm{i}} \end{cases} \tag{3.3}$$

where subscript m denotes the signal mode, K indicates the parameters for the K^{th} ring. The variable Γ stands for the power confinement in a given ring of a given channel in a given mode. Note that since the emission cross-section is zero at 980 nm for the erbium ions, we omitted the term related to it. We also consider only one wavelength channel for the signal, and the background loss is neglected. The factor of 2 in Equation (3.3) takes into account the two polarizations states of each mode. We also note that the azimuthal spatial dependence of the LP_{11} mode was dropped, $I_m(r,\varphi) = I_m(r)$, since we assumed that all four spatial and polarization modes average out during propagation so as to effectively yield a ring shaped intensity profile.

Along with the power evolution equations, the rate equations are given as following,

$$\begin{cases} N_{1,K}(z) = \dfrac{1/\tau + W_{3,K}}{W_{1,K} + W_{2,K} + W_{3,K} + A_K/\tau} N_{\mathrm{T},K}(z) \\ N_{2,K}(z) = \dfrac{W_{1,K} + W_{2,K}}{W_{1,K} + W_{2,K} + W_{3,K} + A_K/\tau} N_{\mathrm{T},K}(z) \\ N_{\mathrm{T},K}(z) = N_{1,K}(z) + N_{2,K}(z) \end{cases} \tag{3.4}$$

where

$$\begin{cases} W_{1,K} = \dfrac{\sigma_{\mathrm{ap}} \Gamma_{\mathrm{p},K} P_{\mathrm{p}}}{h\nu_{\mathrm{p}}} \\ W_{2,K} = \sum_m \left(\dfrac{\sigma_{\mathrm{as}} \Gamma_{(\mathrm{s},m),K} P_{\mathrm{s},m}}{h\nu_{\mathrm{s}}} + \sum_\lambda \dfrac{\sigma_{\mathrm{ai}} \Gamma_{(\mathrm{i},m),K} P_{\mathrm{i},m}}{h\nu_{\mathrm{i}}} \right) \\ W_{3,K} = \sum_m \left(\dfrac{\sigma_{\mathrm{es}} \Gamma_{(\mathrm{s},m),K} P_{\mathrm{s},m}}{h\nu_{\mathrm{s}}} + \sum_\lambda \dfrac{\sigma_{\mathrm{ei}} \Gamma_{(\mathrm{i},m),K} P_{\mathrm{i},m}}{h\nu_{\mathrm{i}}} \right) \end{cases} \tag{3.5}$$

Thus, the population density has a bi-dimensional spatial dependence along the fiber axis direction (z) and the radial direction (r). These equations allow us to describe with good accuracy the population dynamics and the corresponding amplification behavior of several modes, including HOMs.

As mentioned before, a SI-FMF of core radius 8 μm, cladding index 1.445 and NA = 0.1, is assumed throughout the chapter. This FMF supports two co-propagating mode groups (LP_{01} and LP_{11}) in the C-band.

We then consider the three types of erbium doping profiles shown in Figure 3.1, where the maximum relative concentration level (ρ = 1) corresponds to 1×10^{25} m^{-3}. We note that a minimum feature size of 0.5 μm was imposed in all modeled doping profiles for fabrication tolerance.

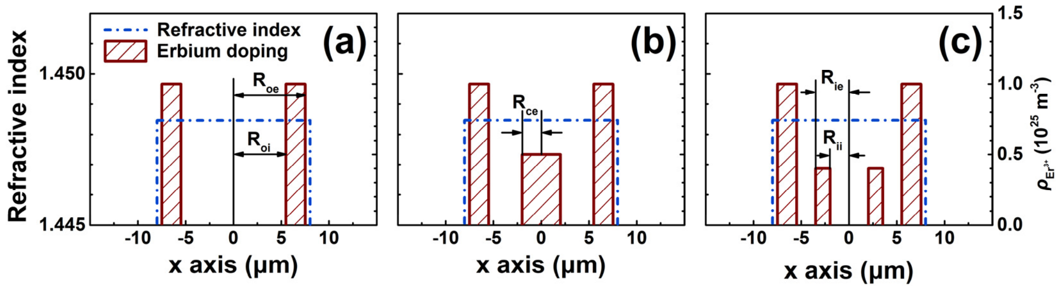

Figure 3.1. Erbium doping profiles: (a) outer ring, (b) outer ring + center rod, and (c) outer ring + inner ring.

A qualitative argument can be made for the doping profiles in Figure 3.1 (b, c) versus that of Figure 3.1(a), i.e. a single ring design. In the case of a single ring, one has limited control over the signal field overlap with the doping regions; since the LP_{01} mode has peak intensity in the center while the LP_{11} mode's peak intensities occur on both sides, a single-ring design typically favors the LP_{11} mode gain. By introducing multiple rings [Figure 3.1(c)] or a center rod [Figure 3.1(b)] in the design of the doping profile, one achieves a more precise control over the MDG. Moreover, this approach allows one to forego the complex multiple pump arrangements in favor of a single fundamental pump.

3.3 Single stage simulation results

Our doping profile design followed these steps: (i) determining and optimizing the parameters of the outer ring; (ii) adding the central doping structure, either inner ring or center rod; (iii) finding the most appropriate doping profile parameters for equalization of the MDG, and MDL compensation, in single-stage or dual-stage multimode doped amplifiers.

3.3.1 Single outer ring doping: fiber parameters and analysis

We first examined the case of a single outer ring [Figure 3.1(a)] of unit relative concentration, internal radius value R_{oi} and external radius R_{oe}. For each pair of parameters (R_{oi}, R_{oe}) we assessed the MM-EDFA's gain and noise characteristics by solving the two-level system rate and propagation in Equations (3.3)-(3.5) through Runge-Kutta 4th order calculations. The simulations took into account the ASE noise power and polarization degeneracy; but neglected mode coupling effects since these were deemed small enough for the short amplifier lengths involved (≤ 10 m) and because the step-index profile provides weak coupling between signal modes [137]; and the fiber background loss is also neglected. Additionally, we utilized a co-propagating fundamental mode pump at 980 nm with 200-mW power.

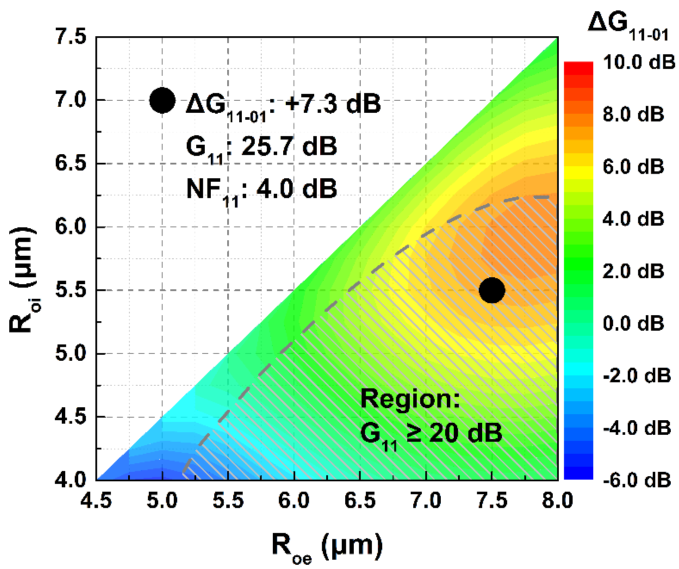

Figure 3.2. Differential modal gain ($\Delta G_{11\text{-}01}$) as a function of R_{oi} and R_{oe} in a 10-m long MM-EDFA with 200-mW of 980-nm pump. The dashed line represents the contour line of 20-dB gain for LP_{11}, while more than 20-dB gain is obtained inside the shaded area. The black dot indicates the parameters of interest for the outer ring design.

The plot in Figure 3.2 of the differential gain (defined as the gain of LP_{11} minus that of LP_{01}: $\Delta G_{11\text{-}01} = G_{11} - G_{01}$) as a function of outer ring parameters (R_{oi} and R_{oe}) allows one to identify the region of the parameter space where $\Delta G_{11\text{-}01} > 0$ can be achieved with a LP_{01} mode forward pump at 980-nm wavelength and P_p = 200-mW input power. We note that a MM-EDFA length of 10 m was implemented in the calculations of Figure 3.2 as we found this value to be close to the optimum length for maximum LP_{11} signal gain, inside the entire parameter space. Superimposed on the same figure, the shaded area indicate G_{11} >20-dB gain. We note that the calculated signal noise was kept below NF <5 dB in all our simulations. Based on these results we selected the outer ring parameters R_{oi} = 5.5 μm and R_{oe} = 7.5 μm as they

More details in the overlap factor calculation can be found in supplementary information section.

yield >20-dB gain and a positive $\Delta G_{11\text{-}01}$ = +7.3-dB gain skew for the LP_{11} mode, thus providing ample room for accommodating additional doping structures inside the center region that can be used to create a reciprocal negative DMG towards net gain equalization (i.e. $\Delta G_{11\text{-}01}$ = 0 dB).

3.3.2 Outer ring with a central rod doping profile

As suggested in the previous section, by adding and tuning the radius (R_{ce}) and concentration level (ρ_c) of a central rod in the doping profile [see Figure 3.1(b)] one can manage MDG and equalize the gain. Figure 3.3 shows the simulated DMG for the whole parameter space (R_{ce}, ρ_c) while using fixed parameters R_{oi} = 5.5 μm and R_{oe} = 7.5 μm for the outer ring, which were pre-optimized in Section 3.3.1. The increased pump absorption due to the central doped rod resulted in the shortening of the optimum fiber length for maximum LP_{11} signal gain. Thus a fixed MM-EDFA length of 7 m was implemented in the calculations of Figure 3.3.

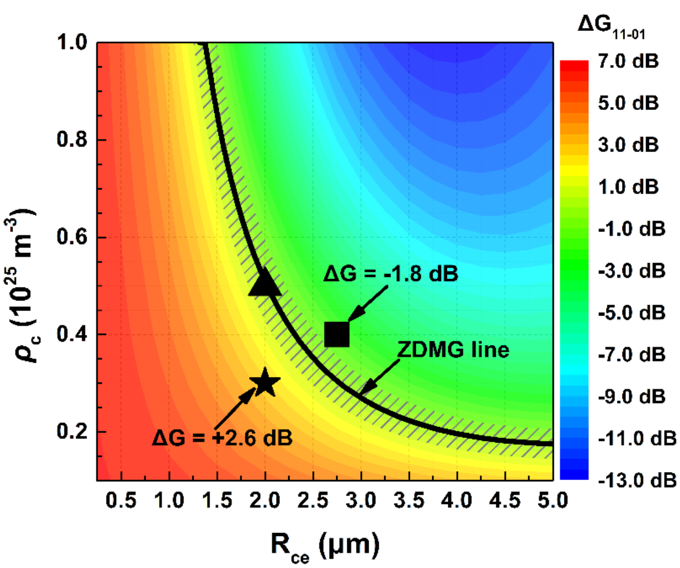

Figure 3.3. Differential modal gain ($\Delta G_{11\text{-}01}$) in a MM-EDFA with a fixed outer ring profile (R_{ob} = 5.5 μm and R_{oe} = 7.5 μm) and for varying center rod doping profiles. Pump power is P_p = 200 mW and doped fiber length is 7 m. The solid line indicates the contour line of ZDMG (ΔG = 0 dB). The marker identified with a star corresponds to ΔG = +2.6 dB while the square marker indicates ΔG = −1.8 dB. The shaded area surrounding the ZDMG line depicts the region where |ΔG| <1 dB.

The numerical results in Figure 3.3 indicate a variety of ZDMG points, where $\Delta G = 0$, which forms a continuous line (solid line in Figure 3.3) inside the parameter space. We selected three different points - denoted respectively by solid triangle, star and square markers, the first one located on ZDMG line while another two are in positive and negative regions - so as to investigate in more detail the performance of the corresponding MM-EDFA.

We remark in Figure 3.3 that although all points located along the ZDMG line can provide $\Delta G = 0$ dB, the profiles described by points located above the triangle marker are less susceptible to fluctuations in the doping concentration level of the center doped rod; while those located below the same marker are more tolerant to slight variations in the actual radius of the center doped rod. For each set of parameters identified, we first simulated the behavior of the MDG with change of input pump power as displayed in Figure 3.4.

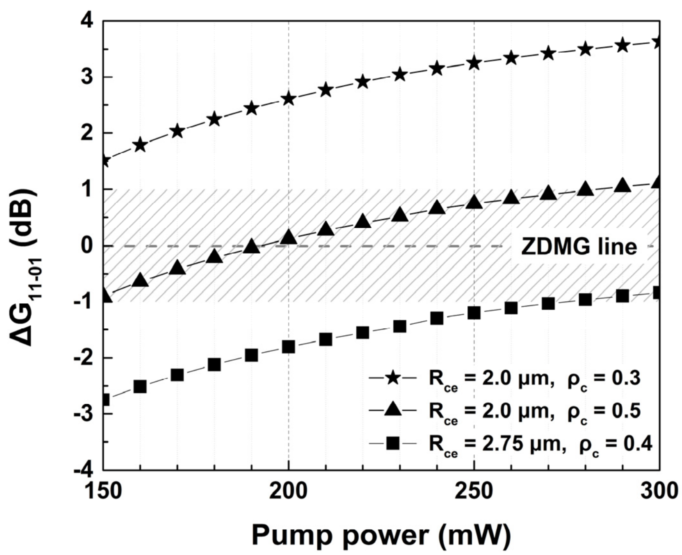

Figure 3.4. Differential modal gain as a function of pump power in a 7-m long MM-EDFA with an outer ring + center rod doping profile. The three solid markers correspond to doping profiles identified in Figure 3.3.

Figure 3.4 indicates the ability of controlling the DMG by about ±1 dB via tuning of the pump power from 150 mW to 300 mW, while crossing the ZDMG line near P_p =200 mW. Selecting the parameters corresponding to the solid star (R_{ce} = 2.0 μm, ρ_c = 0.3) merely shifts by approximately +2 dB the tuning ability with pump power. This feature enables one to dynamically adjust the modal gain in order to overcome the MDLs typically incurred inside a fiber span, as the LP_{01} mode usually suffers lower coupling losses between link components than HOMs. For example, if we assume input signal powers of −13 dBm and −15 dBm for the LP_{01} and LP_{11} modes at 1550 nm and 1555 nm respectively - equivalent to MDL = 2 dB prior to amplifier - one can achieve over 18-dB signal gains and simultaneously compensate for the MDL by using a MM-EDFA with "solid star" doping configuration (R_{ce} = 2.0 µm, ρ_c = 0.3) and input pump power: P_p = 160 mW (as shown in Figure 3.5). We note that slightly different wavelengths were assigned to the signal modes so as to facilitate visualization.

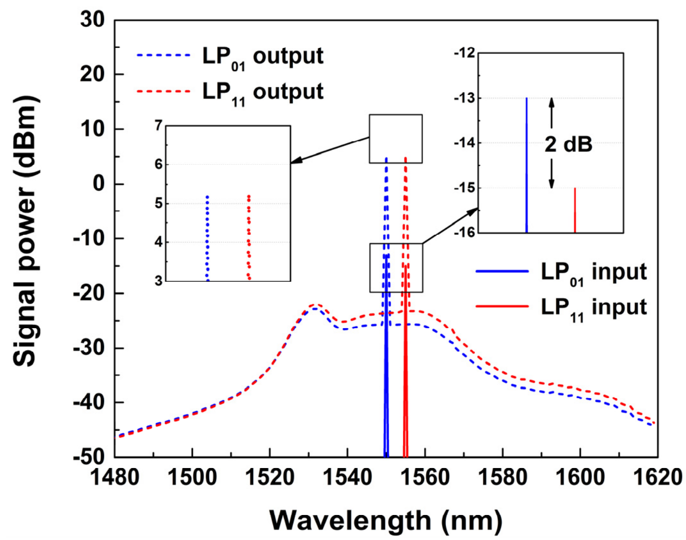

Figure 3.5. Input and output signal power spectra of both modes for the outer ring + center rod (R_{ce} = 2.0 µm, ρ_c = 0.3) doping configuration in a 7-m long MM-EDFA pumped with P_p = 160 mW power. Insets show enlarged views of the input and output power spectra.

3.3.3 Outer ring with inner ring doping profile

Substituting the center rod for an inner doped ring [see Figure 3.1(c)] and keeping the parameters of the outer doped ring fixed as before (R_{oi} = 5.5 µm, R_{oe} = 7.5 µm), parametric simulations (Figure 3.6) were performed as a function of the inner ring bounding radii R_{ii} and R_{ie}, and using a fixed doping concentration level ρ_i = 0.4. The latter concentration level was found to yield adequate LP_{11} signal gain (G_{11} >20 dB) inside the whole parameter space (R_{ii},

R_{ie}) while also providing a moderate and quasi-linear DMG response with input pump power (see Figure 3.7). This systematic approach allows reducing the number of degrees of freedom to only two variables (R_{ii} and R_{ie}) for our parametric analysis.

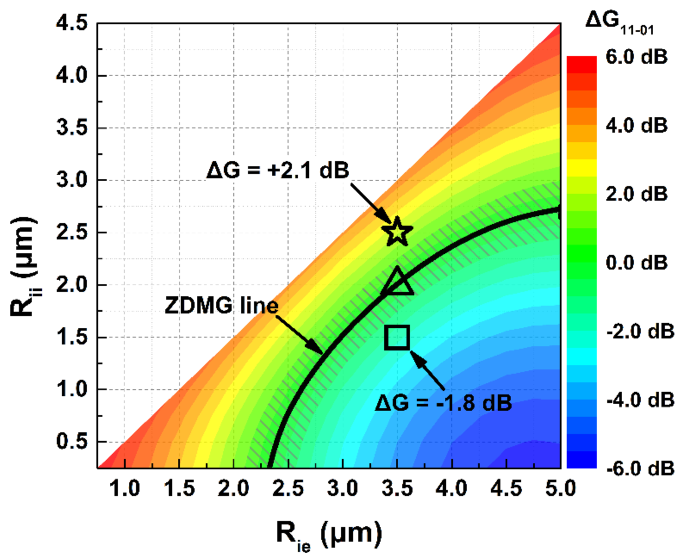

Figure 3.6. Differential modal gain ($\Delta G_{11\text{-}01}$) in a 7-m long MM-EDFA with a fixed outer ring profile (R_{oi} = 5.5 μm and R_{oe} = 7.5 μm) and for varying inner ring doping profiles described with bounding radii R_{ii} and R_{ie}. Pump power is P_p = 200 mW. The solid line indicates the contour line of ZDMG (ΔG = 0 dB). The point identified with a hollow star corresponds to ΔG = +2.1 dB while hollow square indicates ΔG = −1.8 dB. The shaded area surrounding the ZDMG line depicts the region where |ΔG| <1 dB.

Based on the simulation results in Figure 3.6, we again selected three points of interest, denoted respectively by hollow triangle, star and square markers.

As discussed in the previous section, the LP_{11} signal mode typically incurs larger losses than the LP_{01} mode inside a transmission link. Hence the doping profile in Figure 3.6 denoted by the hollow star - which provides ΔG = +2.1 dB gain towards the LP_{11} mode - represents one example among a family of profiles that may be exploited in order to compensate for the MDL. As shown in Figure 3.7, the "hollow star" profile can compensate MDLs varying from 1 to 3 dB through a quasi-linear change of pump power from 150 to 300 mW. Alternatively in the case of almost equal input signal powers, other doping profiles (e.g. hollow triangle marker in Figure 3.6) located along the ZDMG line, may similarly be used to obtain net gain equalization $\Delta G = 0$ dB by tuning the pump power (see Figure 3.7). The observed tuning sensitivity of the MDG with pump power is $\Delta G/\Delta P_p \approx 0.0013$ dB/mW.

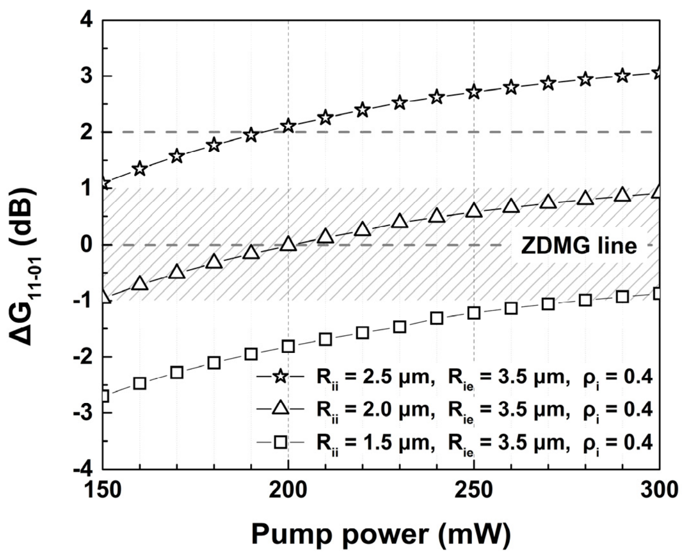

Figure 3.7. Differential modal gain as a function of pump power in a 7-m long MM-EDFA with an outer ring + inner ring doping profile.

3.3.4 Differential modal gain flatness study

Besides sweeping the pump power, we also looked at the wavelength dependence for all sets of parameters highlighted earlier for both outer ring + center rod and inner ring configurations. The results for the outer ring + center rod profiles (see Figure 3.8) indicate that less than 1-dB gain excursion throughout the C-band can be achieved in case of the solid triangle marker located on the ZDMG line (see Figure 3.3) and for pump power levels $P_p \geq 200$ mW. These simulations again demonstrate the possibility of achieving less than 1-dB modal gain excursion across the C-band by appropriate choice of multi-ring/rod doping profiles and pump power.

The wavelength dependent behavior of the DMG for the doping profiles corresponding to the three hollow markers (see Figure 3.6) for the outer ring + inner ring configuration (Figure 3.9), is analogous to that of the outer ring + center rod configuration (Figure 3.8). However the MDGs wavelength dependence is noticeably flatter across the C-band for the outer ring + inner ring compared to the outer ring + center rod configuration. Especially the "hollow star" profile in Figure 3.9, exhibits significantly better DMG flatness with less than 0.5-dB gain excursion inside the C-band when $P_p \geq 250$ mW.

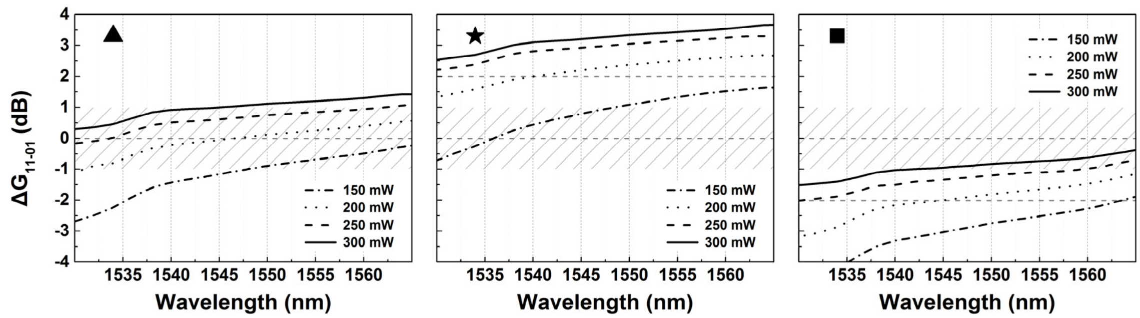

Figure 3.8. Differential modal gain as a function of wavelength under several pump power for the outer ring + center rod doping profile. Where the triangle, star and square marks corresponding to the same points in Figure 3.3. The shaded area corresponds to the |ΔG| <1 dB region.

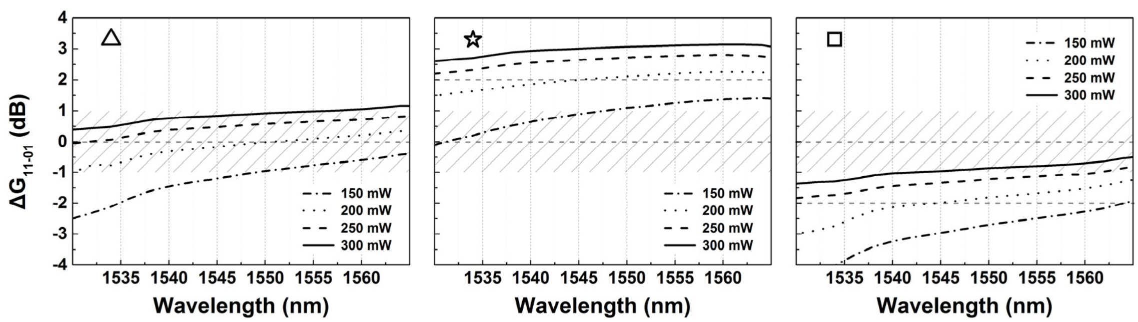

Figure 3.9. Differential modal gain as a function of wavelength under several pump power for the outer ring + inner ring doping profile. Where the hollow triangle, star and square marks corresponding to the same points in Figure 3.6. The shaded area corresponds to the |ΔG| <1 dB region.

This phenomenon can be rationalized as following: as the signal wavelength goes towards long wavelengths, the intensity profile of the fundamental mode will spread and the peak intensity is subsequently reduced in the center. This is why the MDG in a MM-EDFA using a center doped rod structure is more sensitive to wavelengths shifts than a similar profile using the inner ring structure instead.

We close this section by mentioning that we also calculated the NFs for each signal mode in all our simulations. Typical NFs calculated for the single-stage MM-EDFAs were around 4.5 dB with about 0.5-dB noise excursions between the two signal modes.

3.4 Application in two-stage amplifiers

We have shown in the previous section the possibility of tuning the DMG in a single-stage configuration by varying the pump power, albeit with a small change in the signal gain. By exploiting this feature, we demonstrate in this section the ability of tuning the DMG while keeping the signal gain constant in a dual-stage configuration. Figure 3.10 illustrates the lay-out of such dual-stage MM-EDFA, where two 980-nm pump lasers provide fundamental mode pumping for each stage in co-direction with the input signal modes. The two pumps are combined with the signal modes by WDM couplers, and a multimode isolator is inserted to prevent backward ASE and back-reflected light from reentering the first stage.

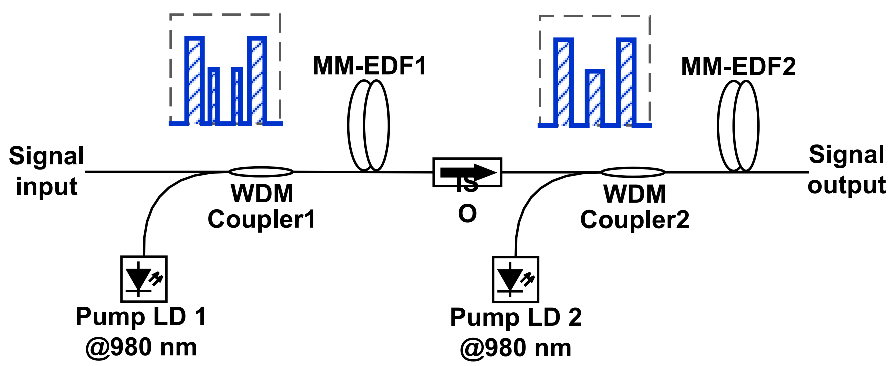

Figure 3.10. Scheme of two-stage MM-EDFA. Two pump lasers at 980 nm serve as fundamental mode forward pumping in co-propagation with the input signal. The first stage has a doping profile made of outer ring + inner ring, the second stage has an outer ring + center rod doping profile. ISO: multimode optical isolator.

The doping profile we chose for the first stage is the outer ring + inner ring because it pro-vides slightly lower NFs than a comparable outer ring + center rod profile. Once the signal power levels have been substantially increased after the first stage, a second-stage with an outer ring + center rod profile enables to adjust the DMG so as to equalize and provide more signal gain.

We chose the hollow triangle (see Figure 3.6) and solid triangle (see Figure 3.3) doping profiles for the first stage and second stage, respectively. We set the input signal power to -30 dBm for both LP_{01} and LP_{11} modes, and varied the pump power for each stage. In the simulation results presented in Figure 11, we ignored coupling and isolator losses.

Figure 3.11 reveals that if the pump power of each stage is properly chosen along the ZDMG line (black solid line), one can equalize the DMG. Moreover, the signal gain can be fixed at either 40 dB or 41 dB, for example, while the ΔG is adjusted from −0.5 dB to +1.0 dB by proper tuning of the two-stage pump powers. The DMG tuning sensitivity with pump power is 0.013 dB/mW for first stage and 0.007 dB/mW for the second. Hence in this case controlling the first stage pump power effectively enables coarse tuning while that of the second stage is used for fine tuning of the DMG.

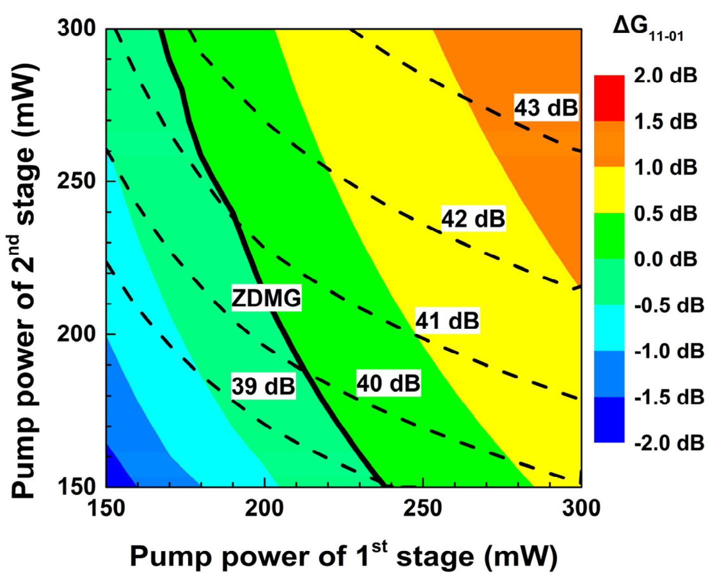

Figure 3.11. Differential modal gain as a function of the pump power in each stage. The black solid line indicates the pair of pump powers which can achieve ZDMG (ΔG = 0 dB); the black dash line represent the contour line for various LP_{11} mode signal gain.

Inside a realistic transmission link, as mentioned before, the LP_{11} mode will typically suffer more attenuation than the fundamental mode. We here describe how to compensate such MDL by using our proposed multi-ring MM-EDFAs in a dual-stage configuration. We first select an outer ring + inner ring doping profile with positive DMG, $\Delta G = +2.1$ dB, (see hollow star in Figure 3.6) for the first stage, and an outer ring + center rod doping profile with negative DMG ($R_{ce} = 4.5$ μm, $\rho_c = 0.25$, $\Delta G = -2.1$ dB) in the second stage. The rationale for doing so is that the first stage with positive DMG acts to compensate the MDL while the second stage is used to adjust and equalize the gain. The results shown in Figure 3.12, indicate a DMG tuning dynamic range from 0 dB to 2.5 dB while keeping the LP_{11} signal gain constant at 41 dB. Observed tuning sensitivities for 1st and 2nd stages are 0.017 dB/mW and 0.007 dB/mW, respectively.

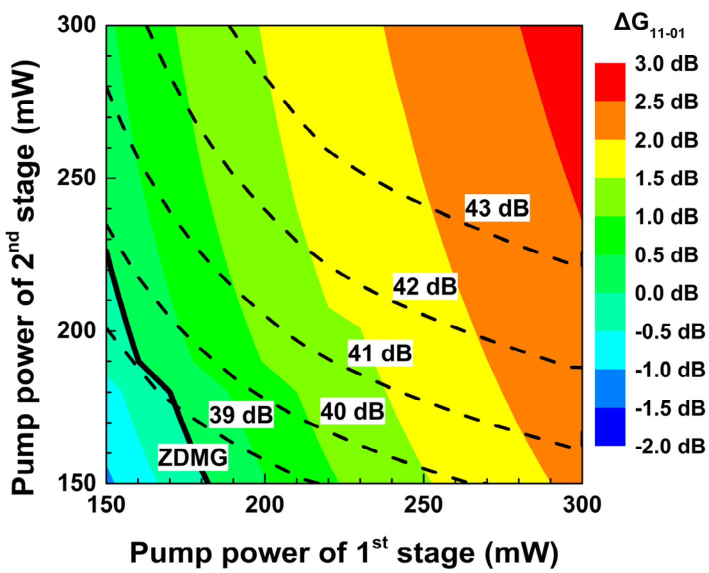

Figure 3.12. Differential modal gain as function matrix of the pump powers of both stages for positive and negative points configuration. The black solid line indicates the pair of pump powers which can achieve ZDMG ($\Delta G = 0$ dB); the black dash line represent the contour line for various LP_{11} mode signal gain.

We remark that owing to the high gain yielded by the dual-stage configuration presented previously, the NFs of the LP_{01} and LP_{11} modes are both kept to relatively low levels of about 4 dB with small deviations <0.2 dB between the two modes. The proposed dual-stage MM-

EDFA scheme enables not only higher gain (>40 dB) than a similar single-stage MM-EDFA, but also lower NFs.

3.5 Conclusions

In this chapter, two types of multi-ring multi-level doping profiles for MM-EDFAs are proposed and investigated: one presents an outer ring + center rod doping profile, while the other has an outer ring + inner ring doping profile. Through numerical simulations of the single-stage MM-EDFAs performance (for LP_{01} and LP_{11} signal modes at 1550 nm) using the engineered doping profiles, we demonstrated precise control over the mode-dependent gain by tuning the fundamental mode pump power (at 980 nm). We predict over 20-dB signal gain for both modes, while gain excursion inside the C-band can be maintained below ± 0.8 dB in the case of the outer ring + center rod profile, and ± 0.5 dB for the outer ring + inner ring profile.

In the dual-stage configuration, via independent control of the pump powers in each stage (150-mW dynamic range) we demonstrate the ability to obtain over 40-dB signal gain while simultaneously compensating for mode-dependent losses up to 2 dB. Moreover, we show that the first stage may serve for coarse tuning of the DMG while the second stage may be used for fine-adjustment tuning and equalization of the DMG. Due to the high gain achieved in a dual-stage configuration, low NFs around 4 dB are obtained throughout the tuning range.

Our analysis also showed that the outer ring + inner ring doping profile results in better gain flatness across the C-band, and this type of doping profile naturally favors the amplification of HOMs that have zero intensity in their center. Moreover, due to the circular symmetry of the multi-ring doping profiles, one is tempted to see them as potential candidates for MM-EDFAs in communication links with recently proposed fibers supporting OAM modes.

3.6 Supplementary information

This section will first present more information on the calculation of overlap factors taking into account radial variations of erbium ion population in the modeling of few-mode fiber amplifiers. We then present some experimental results on the fabrication and characterization of EDF having a central doped rod and a doped outer ring design, including chemical analysis and MDG performance.

3.6.1 Overlap factor calculation

The calculation of radial dependent overlap factor needed to implement the multi-layer model will be reviewed in this section.

For a step-index weakly guiding fiber, the transverse cross-section mode intensity profile, ψ_{lm} (r,φ) is given by the following Bessel and modified Bessel functions[137],

$$\psi_{lm}\left(r,\varphi\right)=\begin{cases} J_l^2\left(\dfrac{U}{a}r\right)f(\varphi) & r\le a \\ \left[\dfrac{J_l\left(U\right)}{K_l\left(W\right)}\right]^2 K_l^2\left(\dfrac{W}{a}r\right)f(\varphi) & r>a \end{cases} \tag{3.6}$$

where J is the Bessel function of the first kind while K is modified Bessel function of the second kind. l indicates the order of Bessel function. U and W are scalar transverse propagation parameters,

$$U=a\sqrt{\left(k_0^2n_{\text{co}}^2-\beta^2\right)} \tag{3.7}$$

$$W=a\sqrt{\left(\beta^2-k_0^2n_{\text{cl}}^2\right)} \tag{3.8}$$

where k_0 is wave number. n_{co} and n_{cl} are fiber core and cladding refractive indices, respectively. β is the mode propagation constant.

The $f(\varphi)$ is azimuthal term,

$$f(\varphi)=\begin{cases}\sin^2(l\varphi) & \text{odd mode}\\ \cos^2(l\varphi) & \text{even mode}\end{cases} \tag{3.9}$$

In order to integrate Equation (2.28), a multi-layer approach [136] was introduced. In that modeling, assuming every layer is thin enough then the dopant concentration and the population inversion can be considered as constant in each layer, and both of the normalized intensity profile and dopant profile exclusively depend on radial variation, i.e. as the function of r. Here we assume that all degenerated modes of a mode group is equally excited.

Figure 3.13 illustrates a multi-layer transverse cross-section which takes the form of a ring shape-liked decomposition of the transverse cross-section in the case of uniform erbium ion doping over the whole fiber core.

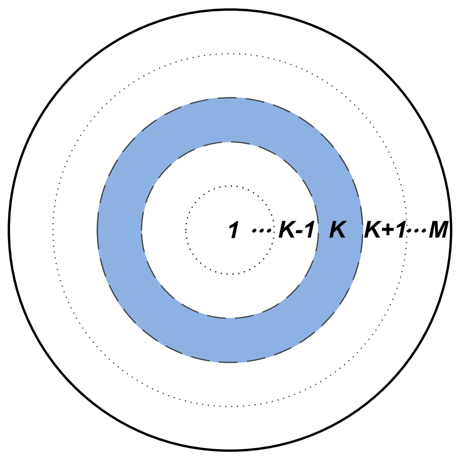

Figure 3.13. Ring shape multi-layer decomposition of the doped area

Assuming erbium ions doping profile has uniform distribution in transverse cross-section which means,

$$N_\rho(r)=\begin{cases}\rho & r\le a\\ 0 & r>a\end{cases} \tag{3.10}$$

where ρ is dopant concentration in a unit of volume and equal to a constant, $\rho = 1\times10^{24}\ \mathrm{m}^{-3}$ as an example.

Following, for a cylindrical fiber, one can define the power filling integral as,

$$\Gamma_k\left(r\right) = 2\pi\int_0^a I_{\mathrm{n}k}\left(r\right) rdr \tag{3.11}$$

where $I_{\mathrm{n}k}$ (r) is radial dependent normalized intensity profile that similar to Equation (2.28).

In this multi-layer decomposition, the Equation (3.11) can be calculated layer by layer for all the incident beams including pump, signal, and ASE,

$$\Gamma_{k,K}\left(r\right) = \frac{\int_{r_{K-1}}^{r_K} \psi\left(r\right) rdr}{\int_0^{\infty} \psi\left(r\right) rdr} \tag{3.12}$$

where $\Gamma_{k,K}$ is the power filling factor for the K^{th} layer of the k^{th} channel. In addition, the number of Γ_K is M which is determined by the required calculation accuracy. Taking into account the trade-off between computing time and accuracy, M is set to 100 in [136].

3.6.2 Fiber parameters

An EDF with the design parameter presented in Table 3.1 was fabricated at the COPL (fiber 2012G3).

Table 3.1. Designed fiber parameters of 2012G3

Item	Value	Unit
r	8.0	µm
NA	0.1	-
R_{ce}	3.0	µm
R_{oi}	5.5	µm
R_{oe}	7.5	µm
ρ_{c}	0.27	a.u.
ρ_{o}	1.0	a.u.

3.6.3 Chemical analysis results

Before and after the fiber drawing, both the preform and fiber have been analyzed by Electron Probe Micro Analyzer (CAMECA) at the Laboratoire de Microanalyse, Department of Geology and Geological Engineering. The results including micrographs and weight percentage for doping components (Er_2O_3, P_2O_5, Al_2O_3, and GeO_2) across the transverse cross-section (Figures 3.14 and 3.16) are given as in figures 3.15 and 3.17. For the fiber, the analysis was made for fibers drawn from a position corresponding to 150 mm and 250 mm from the beginning of the preform.

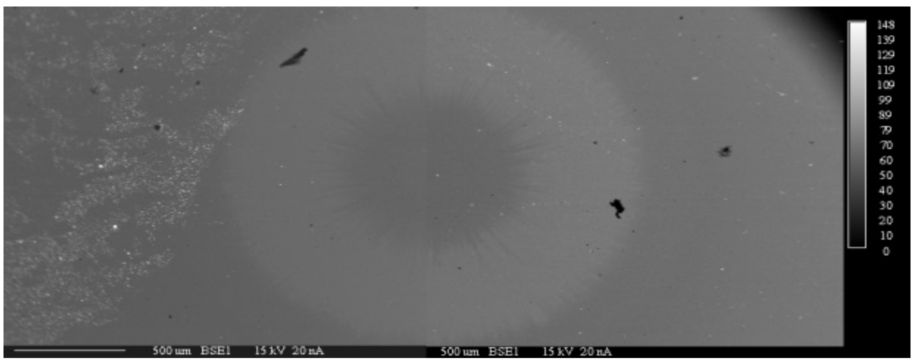

Figure 3.14. Micrograph of the preform cross-section

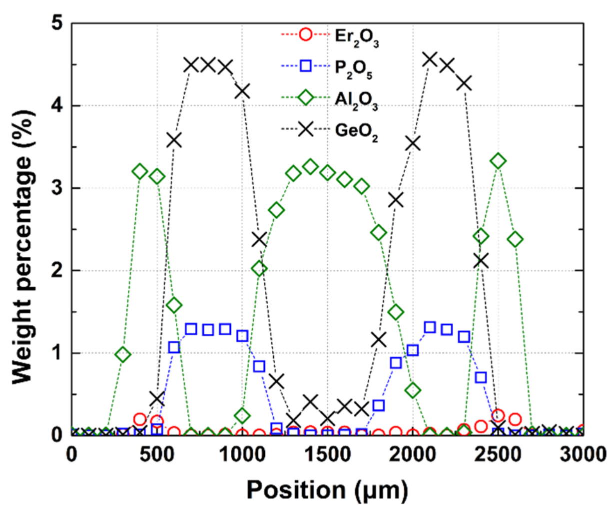

Figure 3.15. Weight percentage of dopants across a cross-section of the preform

The scanning radial position resolution is not sufficient for the fiber scale measurement, in particular for the Er weight percentage which is smaller than other elements. We note that the concentration profile should not change obviously, therefore we did a downscaling in order to utilize the profile of preform to observe the Er profile of fiber. Such downscaling follows several steps below.

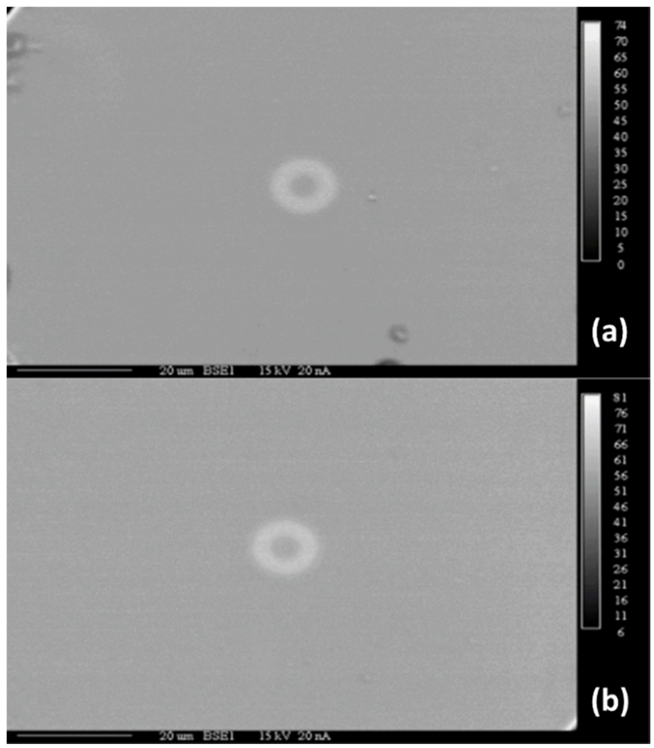

Figure 3.16. Micrograph of a cross-section of fibers drawn from the position of preform at (a) 150 mm, (b) 250 mm

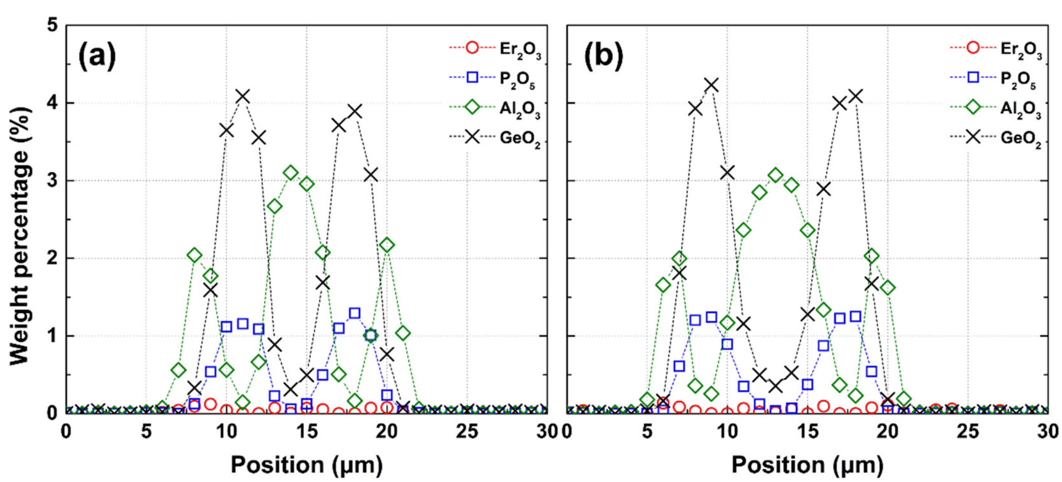

Figure 3.17. Weight percentage of dopants across a cross-section of fibers drawn from the position of preform at (a) 150 mm, (b) 250 mm

Step 1. Determine the downscaling ratio from preform to the fiber by using the Al weight percentage distribution. Firstly, we extracted the data of Al from the preform weight percentage of dopants results and modified it to center the distribution along the radial axis. The same procedure is done for the Al weight percentage distribution of the fiber. Then we know that the downscaling ratio is 157.69~178.26 by comparing the Al weight percentage distribution. The mean value is 167.98. To be more confident, we observed the Ge weight percentage distributions of both preform and fiber in the same way. Referring to the Ge weight percentage distribution, we obtained that the ratio is 152.94~185.71 and the mean value is 169.33. Therefore, the downscaling ratio can be taken as average of both mean values above, which is 168.65.

Step 2. After determining the downscaling ratio, we initially shifted the Er weight percentage distribution of the preform to be centered as previous treatment. Note that, according to the 0.08 % equipment detection limit, the points under such level are uncertain. We found that the distance between the doped areas on both sides of the preform, or equivalent the diameter of the ring doping, is 2000 μm.

Step 3. We then downscale the Er weight percentage distribution of the preform to the fiber dimension according to the ratio obtained in *Step 1*. Consequently, the diameter of the ring doping areas is 12 μm. Considering that the designed doping area for the outer ring is from a radius of 5.5 to 7.5 μm, the expected diameter value was 13 μm.

Step 4. Verify the procedure by downscaling the Al and Ge weight percentage distributions to the fiber dimensions and compare them to the measurement data of fiber. By doing so, we concluded that the downscaling procedure is well matched to the measured data of the fiber. However, contrary to the position matching, the weight percentage levels are not the same.

Step 5. Convert the weight percentage to the ion concentration. See the final profile in Figure 3.18.

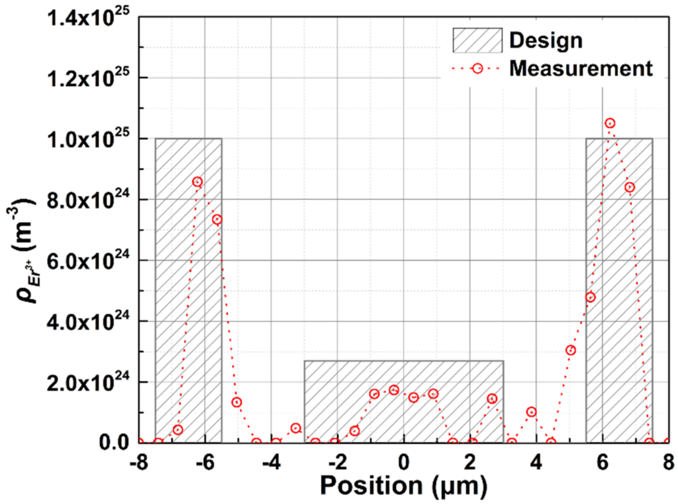

Figure 3.18. Er^{3+} distribution along the transverse cross-section of design and measurement (downscaled)

3.6.4 Absorption spectrum analysis

A piece of fiber (about 1 m) was used for absorption analysis. Due to the fiber under test supporting two mode groups, we applied a mode stripper which was made by a coiling a section of the fiber under test in order to remove the LP_{11} mode. Otherwise, the mode beating will deteriorate the measurement accuracy, as shown in Figure 3.19. The observed spectrum covers from 900 nm to 1700 nm and was obtained by injecting a broadband source into the fiber under test. The two main absorption peaks are 980 nm and 1532 nm (see Figure 3.19), with absorptions of 3.4 dB/m and 6.4 dB/m for the pump and the signal (with mode stripper), respectively.

3.6.5 Simulation with measured profiles

Besides the Er^{3+} concentration profile, we measured the refractive index profile of the fiber by using the EXFO NR-9200. As we can see in Figure 3.20, the fabricated fiber diameter matches well our design, the core index is slightly higher than expected, however. The ripples on the measured profile are due to the Al and Ge doping. We here also compared the fundamental mode intensities at 1550 nm for both profile, the simulation results indicate that they are almost completely overlapping.

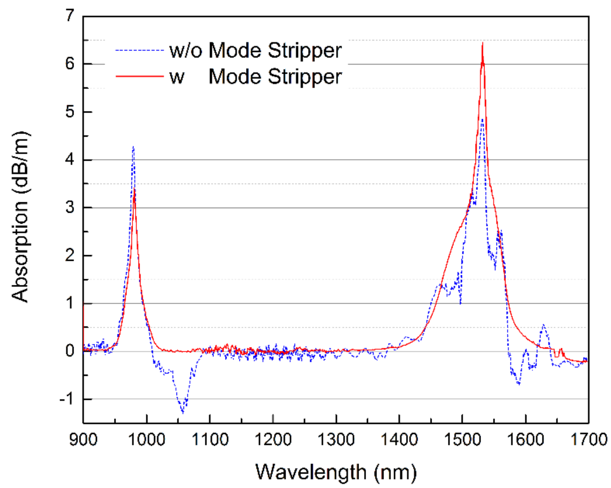

Figure 3.19. Absorption spectrum of the fiber under test

On the other hand, based on the downscaling concentration profile mentioned above, we implemented a modified Er^{3+} concentration distribution by symmetrizing and averaging the result we obtained in section 3.6.3. The procedure firstly made an interpolation within the core area from the measured data points; then the interpolated values in both sides of the transverse cross-section were averaged to each other; finally, the modified profile was automatically symmetrized and it is depicted in Figure 3.21. The curve from center up to boundary of the core has 800 point, which means the simulation resolution is 0.01 μm, the same resolution that we used for the designed profile before.

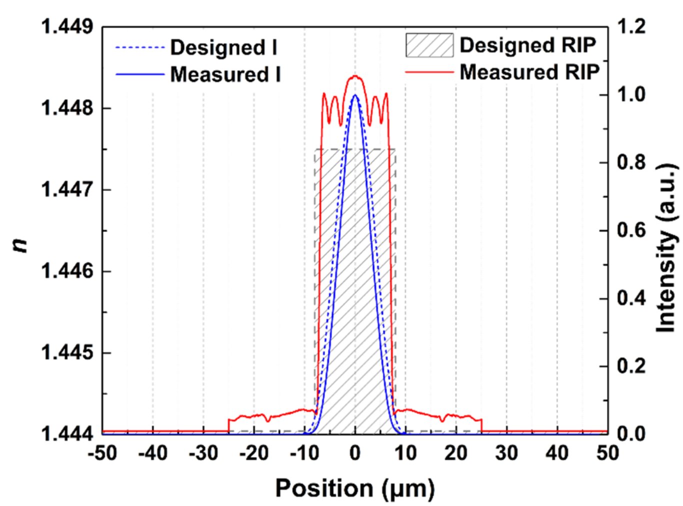

Figure 3.20. Designed and measured RIPs with corresponding LP_{01} intensities at 1550 nm

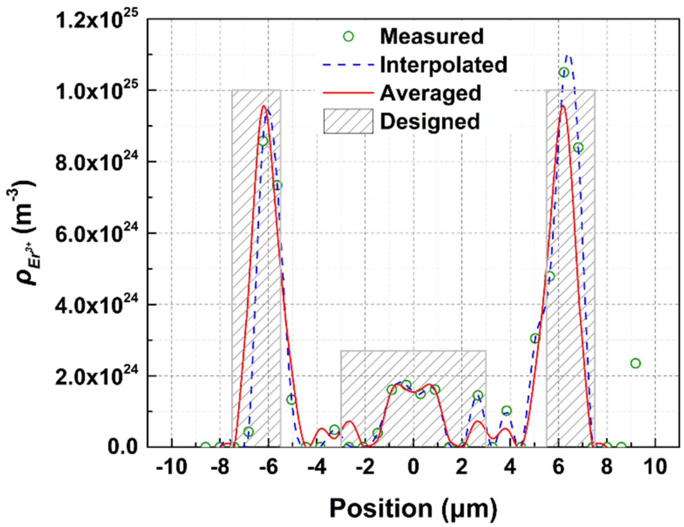

Figure 3.21. Designed and measured Er^{3+} concentration profiles

The main simulation results are illustrated in Figure 3.22 and Figure 3.23. The forward ASE level reveals opposite features, i.e. the power is higher for the measured profile at short wavelength while lower at long wavelength side, and vice versa; both levels of two modes are similar at short wavelength for measured profile however that occurs at long wavelength for designed one. The pump absorption capability of measured profile is weaker than what we expected. Under the same fiber length, e.g. 14 m, the signal gain for each mode is almost identical and tends to saturate for the designed profile; contrasting to that, signal gain for the measured profile is still increasing towards 14 m and mode gain difference is non-neglectable which is about 4 dB. Although the signal gain performance is not as good as the designed case, the NF of the measured profile is better than designed one, additionally, all the NFs are less than 4 dB at the 14-m output.

Following, based on such measured profiles, we did the simulations and compared their results to the one of the designed profiles previously discussed in the paper.

The better NF performance at 1550 nm can be explained by observing the population densities of upper and lower level. Since the designed erbium concentration profile is an idealized model, i.e. the Er^{3+} ions only exist in the areas limited to the center rod and outer ring, there is not any ion in the rest of the core. That results in a finite interaction between incident light photons and Er^{3+} ions, the upper-level population is consequently insufficient and more ASE happens. As to the measured erbium concentration profile, such limit is broken and there are ions in elsewhere than the center rod and out ring. Hence, we can see in Figure 3.23, the upper-level population is higher than the ideal case across the transverse cross-section and the ASE level is consequently reduced.

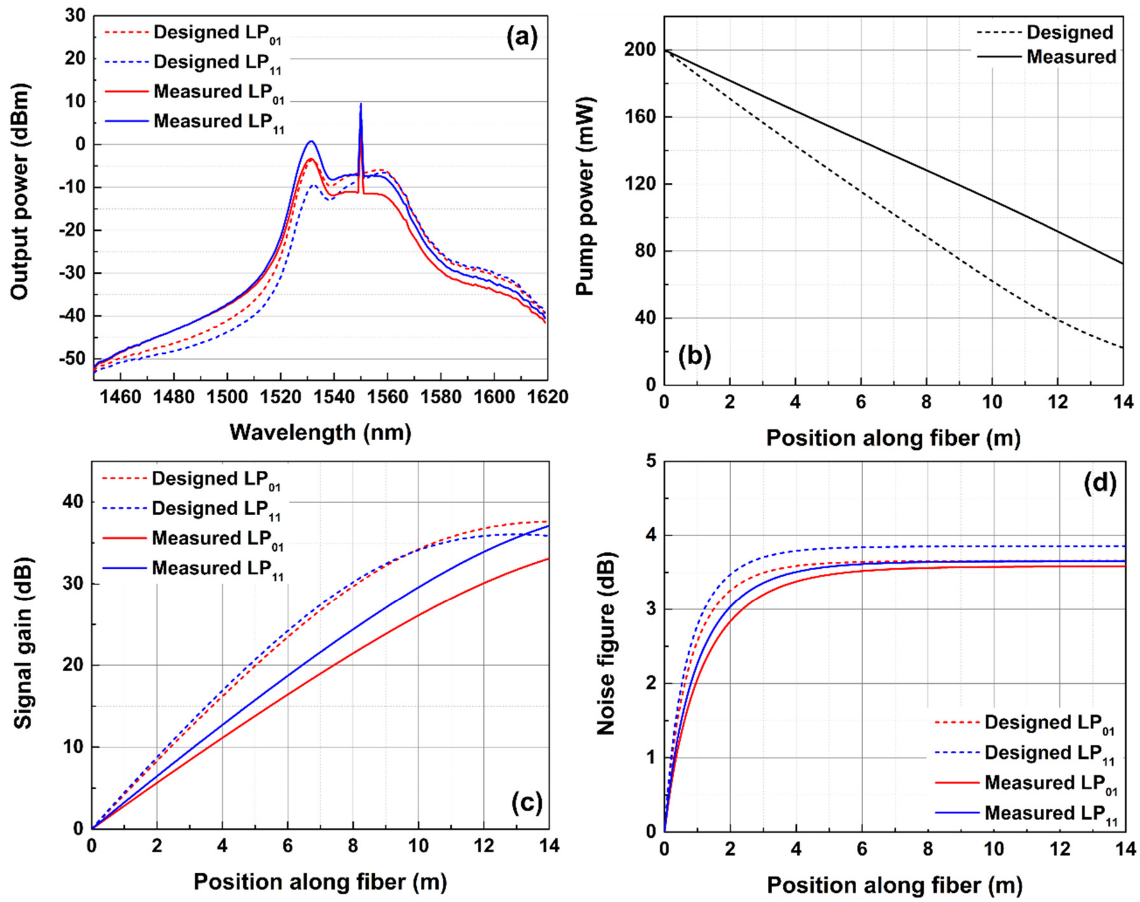

Figure 3.22. Simulation results comparison for designed and measured profiles, (a) output spectrum, (b) pump power along the fiber, (c) signal gain along the fiber, and (d) NF along the fiber

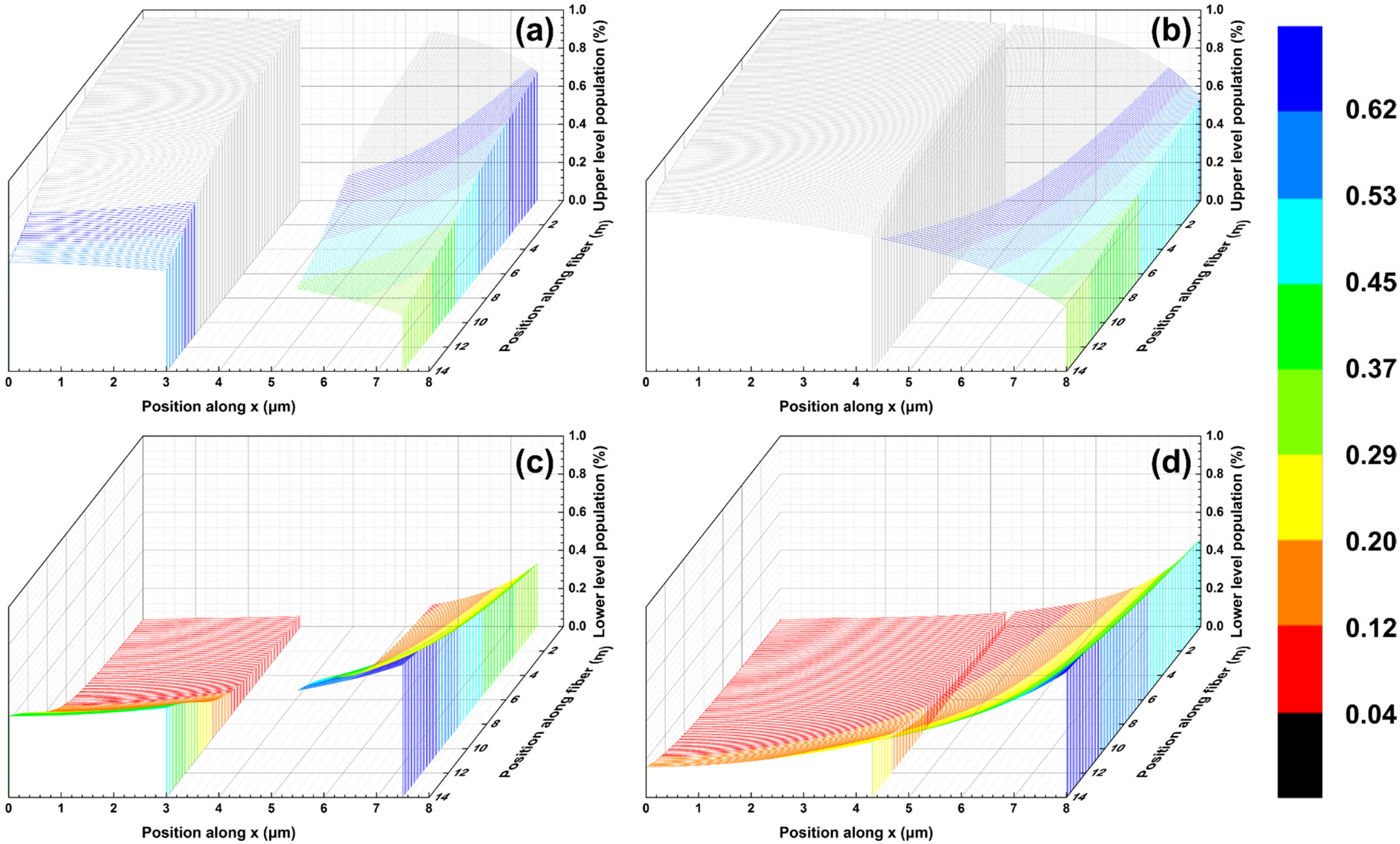

Figure 3.23. (a) Upper-level and (c) lower-level population densities of designed profiles, and (b) Upper-level and (d) lower-level population densities of measured profiles

3.6.6 Swept wavelength interferometer characterization

We employed a swept wavelength interferometer (SWI) [138] to characterize the amplifier performance based on the fiber tested above. The measurement setup is drawn in Figure 3.24. The output signal from the SWI was combined with the pump light coming from a 980-nm single mode laser diode. The pump diode current was 600mA, which provides about 300-mW pump power. After that, the combination of signal and pump is converted to the desired mode via the mode selective three-mode photonic lantern (PL) which has 10-dB extinction ratio and then fed into the 50-m FM-EDF under test.

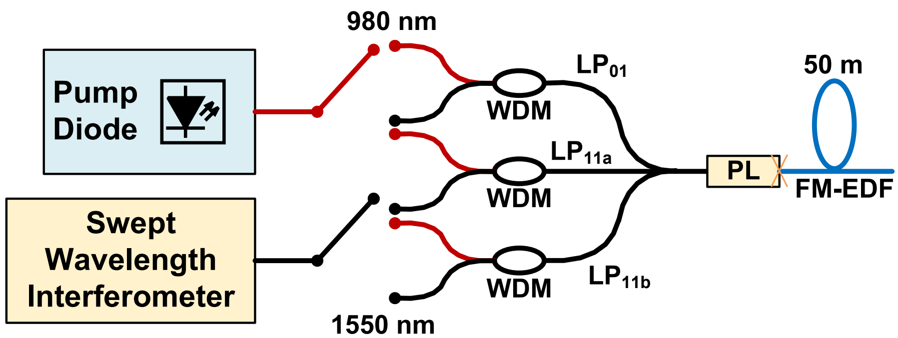

Figure 3.24. Experimental setup for the FM-EDF characterization

The mode patterns for both 1550-nm signal and 980-nm pump after photonic lantern are shown in Figure 3.25. The reflected signal propagated through the input path and was received by the SWI. The signal gains for all the three spatial modes were measured separately, i.e. each time only one mode was observed.

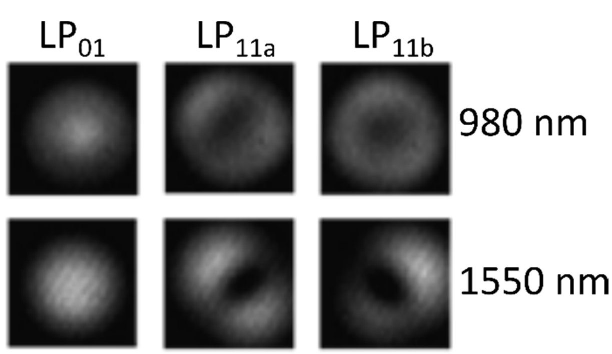

Figure 3.25. Mode patterns of LP_{01} and LP_{11} at 980 nm and 1550 nm after photonic lantern

Figure 3.26 shows the reflected signal powers of LP_{01} (blue curve) and LP_{11} (green curve, addition of both spatial degenerated modes) from the 50-m FM-EDF. Thanks to the backward scattering information along the fiber axis, one can determine the optimized length of both modes by evaluating the peak points in Figure 3.26. The optimized lengths under 600-mA pump current for LP_{01} and LP_{11} are about 14 m and 17 m, and respective signal gains are 22.3 dB and 17.6 dB, respectively. In addition, the DMG between LP_{01} and LP_{11} is about 5 dB for the fiber length of 15 m.

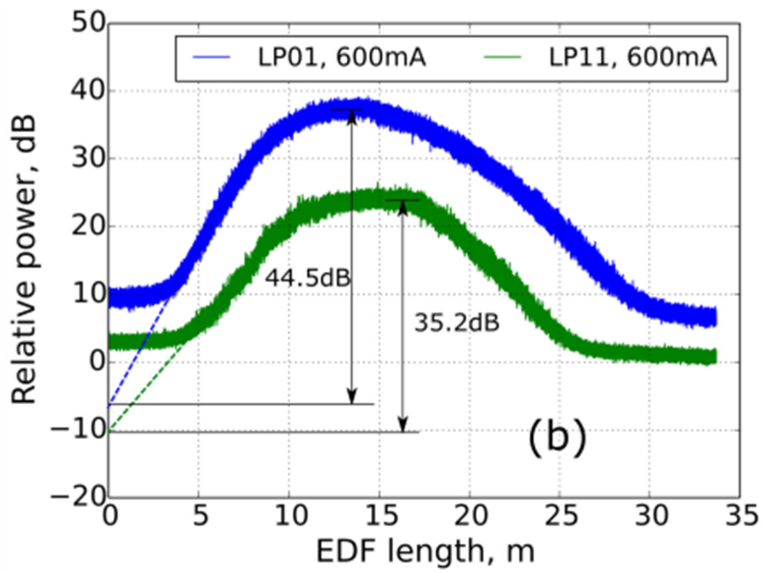

Figure 3.26. Backward reflected powers of LP_{01} and LP_{11} under I_p = 600 mA.

3.7 Summary

In this chapter, we proposed and discussed the multi-layer, multi-level erbium doping design of the FM-EDF. As for the fiber characterization, chemical analysis indicates that the fabricated doping profile does not match the design well. The double-stage amplifier was not able to realize due to devices such as few-mode isolator are unavailable. In addition, we obtained about 5-dB DMG under certain pump power by SWI measurement. The engineering doping profile will become sophisticated because of more modes introducing. Moreover, the core pumping scheme reveals complicated implementation that needs several WDM couplers. Therefore, the alternative way to equalize the DMG and reduce setup complexity is employing cladding pump scheme.

Chapter 4

Annular-cladding Multicore Erbium-doped Fiber for SDM Amplification

Abstract

We propose and numerically investigate annular-cladding multicore erbium-doped fiber (AC-MC-EDF) with either solid or air hole inner cladding to enhance the pump power efficiency in optical amplifiers for SDM transmission links. We first propose an all-glass fiber in which a central inner cladding region with a depressed refractive index is introduced to confine the pump inside a ring-shaped region overlapping the multiple signal cores. Through numerical simulations, we determine signal core and annular pump cladding parameters respecting fabrication constraints. We also propose and examine a multi-spot injection scheme for launching the pump in the annular-cladding. With this all-glass fiber with annular-cladding, our results predict 10-dB increase in gain and 21 % pump power savings compared to the standard double cladding design. We also investigate a fiber with an air hole inner cladding to further enhance the pump power confinement and minimize power leaking into the inner cladding. The results are compared to the all-glass AC-MC-EDF.

Résumé

Nous proposons et étudions numériquement une fibre optique dopée à l'erbium multi-cœurs ayant une gaine annulaire (AC-MC-EDF) pour guider le signal pompe. Le centre de la fibre est fait soit avec un verre ayant un indice de réfraction inférieur à celui de la silice ou encore est constitué d’un trou. La gaine en anneau permet d’augmenter l’intensité de la pompe et l’efficacité des amplificateurs optiques pour le SDM dans des liaisons de télécommunications optiques. Grâce à des simulations numériques, nous déterminons les paramètres des cœurs de la fibre optiques transportant les signaux et ceux de l’anneau afin d’optimiser le recouvrement de la pompe et des cœurs tout en respectant les contraintes de fabrication. Nous proposons et examinons également un système d'injection multi-point pour le lancement de la pompe dans la gaine annulaire. Nos résultats prédisent que cette fibre tout en verre ayant une gaine annulaire présentera un gain supérieur de 10 dB et offrira une économie d’énergie de 21 % par rapport à une fibre à double gaine standard. Nous étudions également une fibre ayant un trou d'air pour améliorer encore le confinement de la puissance pompe et minimiser la fuite de puissance vers l'intérieur de la gaine. Les résultats sont comparés à la fibre tout en verre.

4.1 Introduction

The recent exponential growth of data traffic, fueled by applications such as cloud computing and mobile streaming, has by now practically exhausted all known means (e.g. wave-length, polarization and time division multiplexing, and higher-order modulation formats) of increasing the capacity of SMFs [125][139]. Beyond those techniques, SDM is a promising approach to overcome the anticipated '*capacity crunch*' [4][140] while minimizing the energy per bit [126][141]. This is realized by exploiting a new degree of freedom, the space, through which one can multiplex a number of data channels with-in a single fiber strand, i.e. sharing the same cladding. There exists two main SDM schemes, firstly using MMFs that can be either graded index [142] or step index [97], in which each orthogonal mode corresponds to an independent channel, or secondly using MCFs [143], in which each core corresponds to a different link. Hybrid implementations of these SDM techniques have been performed for increased capacity [56][55] and switching between different SDM schemes along a transmission link has been demonstrated to illustrate their compatibility [144]. This chapter is focused on optical amplifier design for the MCF embodiment.

At the heart of any practical implementation of SDM schemes for long-haul transmission links is the development of high-performance and cost-effective inline optical amplifiers [145][146]. Both MC-EDFAs [121] and multicore Raman amplifiers [147] have been studied recently. For MC-EDFA, the pumping configuration is an important issue. In-core pumping of an MC-EDFA avoids the drawback of using multiple parallel EDFAs, one for each core of the multicore transmission fiber, but it requires several single-mode pump lasers, WDM couplers, and more importantly spatial channel demultiplexers/multiplexers at the amplifier input (or output for a counter-propagating pumping configuration) that can degrade NF and introduce cross-talk [121]. In order to reduce pumping complexity and related costs, cladding pumping is also actively studied towards efficient multicore SDM amplification [105]. Cladding pumping allows the use of low-cost and high-power multimode diode lasers that pump all erbium-doped cores simultaneously. However, an important limitation to the efficiency of this method is the low pump field overlap with the doped cores. This naturally originates from the small aggregate core area compared to pump cladding area (assuming a uniformly distributed pump power). In this regard, the improvement of the signal and pump overlap should ideally be performed by shrinking the cladding rather than enlarging the signal cores that must maintain the single mode propagation condition.

In this chapter, we propose and study a double-cladding erbium-doped six-core fiber with an annular-cladding (AC-MC-EDF) to guide the multimode pump field. The chapter is organized as follows. In Section 4.2, we delineate the operating principle of the AC-MC-EDF by outlining the combination of core and cladding designs, and we identify the design constraints related to fiber fabrication with MCVD process. Subsequently, in Section 4.3, using the determined parameters, we investigate the performance of the novel AC-MC-EDF through numerical simulations, calculating signal gain and NF. In Section 4.4, we discuss three configurations to launch the pump in the annular-cladding, enlightening possible solutions to be tested in future experiments. Finally, our conclusion discusses the design of annular-cladding for multicore amplifiers in view of the simulation results, as well as future work.

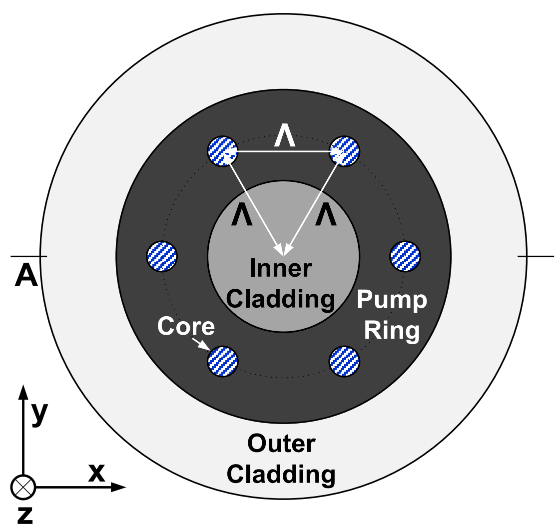

Figure 4.1. Transverse cross-section of AC-MC-EDF showing: the annular pump cladding (dark gray), doped cores (blue), depressed inner cladding (gray), and outer cladding (light gray).

4.2 Fiber structure and design

4.2.1 Fiber structure description

The proposed design of an AC-MC-EDF is shown in Figure 4.1. It consists of a double cladding structure that contains six doped cores for signal amplification. However, in contrast to most previous studies proposing seven core fibers, the center core, which is more susceptible to cross-talk, is absent [144]. This MCF design, placing cores along a ring, has been demonstrated with up to 12 cores [68]. The inner cladding further presents a depressed refractive index value so that the pump is actually guided by an annular (or ring) cladding index profile.

Figure 4.2 shows the refractive index profiles of several types of MC-EDFs, namely the annular-cladding design with depressed-index inner silica cladding [ACS-MC-EDF, Figure 4.2(a)], depressed-index inner cladding made by an air hole [ACA-MC-EDF, Figure 4.2(b)], the standard double cladding fiber (DC-MC-EDF) that will be used for comparison [Figure 4.2(c)], and the conventional single cladding fiber which will be used to determine the minimum annular-cladding thickness [Figure 4.2(d)]. In all cases, the fiber cladding is populated by six cores, as shown in Figure 4.1. The cores are arranged in a ring with a core-to-core pitch (and core-to-center distance), Λ. Based on previous studies of multicore transmission fibers [130], acceptable cross-talk level is achieved with Λ = 40 μm and a similar value was chosen here. This six-core geometry was recently demonstrated with a standard double cladding MC-EDF [144][108]. The pump annular-cladding is assumed to be pure silica, with refractive index $n_{\text{clad,p}}$, and the outer cladding is a low-refractive index polymer, with refractive index $n_{\text{clad,out}}$. The inner cladding could be formed by two means: a solid all-glass inner cladding or an air hole inner cladding. In Fig. 2(a), the depressed-index inner cladding is made with fluorine-doped silica, with refractive index $n_{\text{clad,in}}$. We consider that a maximum refractive index step $n_{\text{clad,p}}-n_{\text{clad,in}} = 5.9\times10^{-3}$ is achievable with fluorine-doped silica. Certainly, the use of an air hole as inner cladding [Figure 4.2(b)] provides a much larger index step. Table 4.1 shows the definition of the respective refractive indices and the main geometrical parameters of all designs where several values are left to be specified. In sub-sections

4.2.3 and 4.2.4 below, we will determine the missed values, i.e. signal core parameters and design the pump ring accordingly.

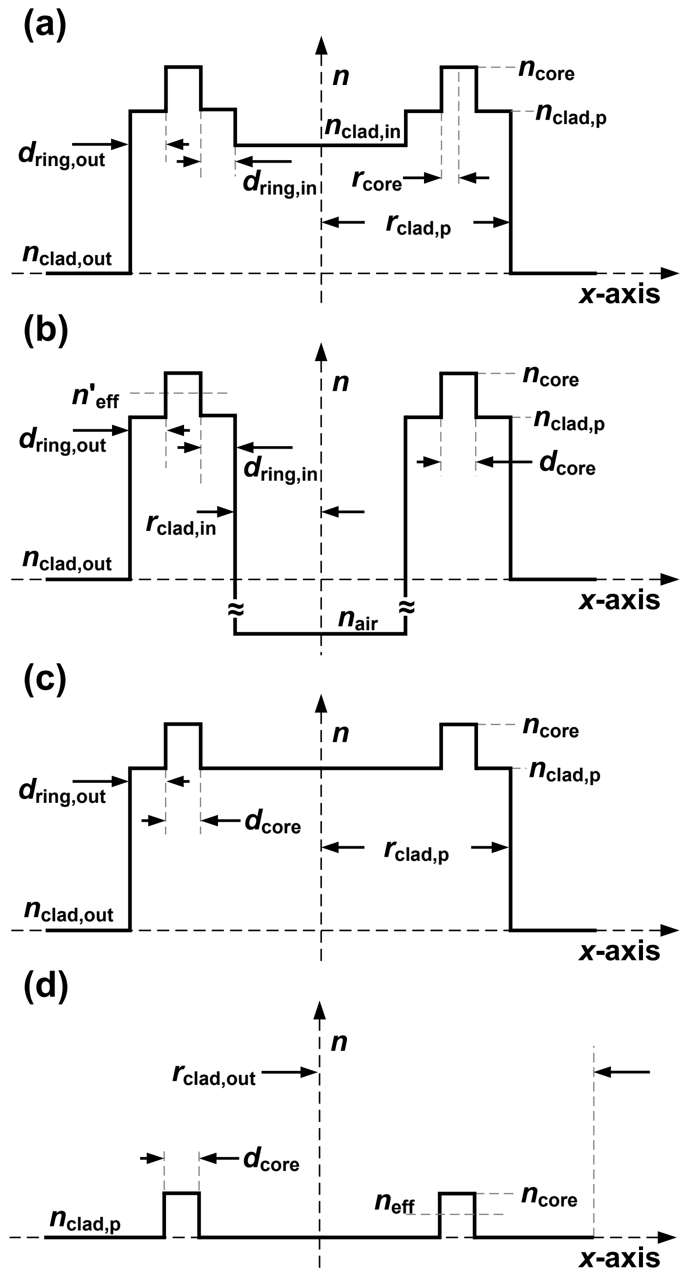

Figure 4.2. Refractive index profile (taken along the A line of Fig. 1.) of a multicore erbium-doped fiber with a) annular pump cladding with solid inner cladding, b) annular pump cladding with air-hole inner cladding, c) standard double cladding, and d) single clad-ding.

Table 4.1. Fiber parameters

Item	Value	Unit	Definition
n_{core}	TBD	-	Signal core refractive index
$n_{\mathrm{clad,p}}$	1.44402	-	Pump cladding refractive index
$n_{\mathrm{clad,in}}$	TBD	-	Inner cladding refractive index
n_{air}	1.0	-	Air refractive index
$n_{\mathrm{clad,out}}$	1.37	-	Polymer refractive index
d_{core}	TBD	µm	Signal core diameter
$d_{\mathrm{ring,in}}$	TBD	µm	Distance from signal core edge to pump cladding inner edge
$d_{\mathrm{ring,out}}$	TBD	µm	Distance from signal core edge to pump cladding outer edge
r_{core}	TBD	µm	Signal core radius
$r_{\mathrm{clad,in}}$	TBD	µm	Inner pump cladding radius
$r_{\mathrm{clad,out}}$	70	µm	Outer polymer cladding radius
$r_{\mathrm{clad,p}}$	TBD	µm	Outer pump cladding radius

The benefits brought about by such cladding geometry are motivated by the reduced power consumption and lower achievable NFs due to the larger pump-signal field overlap. In general the required pump power, P_{d}, for a given inversion ratio η, is related to the power density, S_{p}, through [145],

$$P_{\mathrm{d}} = S_{\mathrm{p}} \times A_{\mathrm{clad}} = \frac{\eta\left(h\nu A_{21}/\sigma_{13}\right)}{1-\eta} A_{\mathrm{clad}} \tag{4.1}$$

where h is Planck's constant, v the pump light frequency, A_{21} the spontaneous emission rate, σ_{13} the pump absorption cross-section at v, and A_{clad} the cladding area where the pump field is confined. For a 50 % inversion ratio, a 980 nm pump, A_{21} = 10^{-2} s^{-1} (typical value for

Erbium, corresponding to $\tau = 10$ ms) and $\sigma_{13} = 2.18\times10^{-25}$ m^2, one finds a pump power density $S_p = 92.98$ MW/m^2. Therefore the required pump power is 0.88 W for a conventional cladding of 55 μm radius, while it is 0.70 W for a similar annular-cladding of 25 μm inner (depressed cladding) radius and 55 μm outer radius. In the previous representative example, the switch from a conventional cladding to an annular-cladding translates into 21 % savings in power consumption, which is an increasingly important metric in contemporary telecommunication networks.

4.2.2 Amplifier modeling

Some fiber parameters, such as (r_{core}) and numerical aperture (NA) can be optimized through numerical calculations, using standard coupled rate equations [124], to evaluate the expected small signal gain (G) and NF with given amplifier operation scenarios. Here, we note that there is no conceptual difference between a solid and an air hole inner cladding design under a uniform pump power distribution assumption as they both achieve similar overlap factors of the pump with the cores. Consequently, in the following model, we only consider the solid inner cladding case. For simplicity, particularly for the signal core optimization in Section 4.2.3, signal power amplification is simulated in only one core but the pump absorption takes into account the presence of all cores. The equations describing power evolution along the fiber are thus given by [124],

$$\frac{dP_{\text{p}}(z)}{dz} = -N_1\sigma_{\text{ap}}\frac{N_{\text{core}}A_{\text{core}}}{A_{\text{ring}}}P_{\text{p}}(z) \tag{4.2}$$

$$\frac{dP_{\text{s}}(z)}{dz} = \left(N_2\sigma_{\text{es}} - N_1\sigma_{\text{as}}\right)\Gamma_{\text{s}}P_{\text{s}}(z) \tag{4.3}$$

$$\frac{dP_{\text{i}}^{\pm}(z)}{dz} = \left(N_2\sigma_{\text{ei}} - N_1\sigma_{\text{ai}}\right)\Gamma_{\text{i}}P_{\text{i}}^{\pm}(z) \pm 2h\nu_{\text{i}}\Delta\nu_{\text{i}}N_2\sigma_{\text{ei}}\Gamma_{\text{i}} \tag{4.4}$$

where $\sigma_{a,j}$ and $\sigma_{e,j}$ are respectively the absorption and emission cross-sections for the pump (j = p), signal (j = s) or ASE (j = i). P_p is the pump power at 980 nm, P_s is the signal power at the given signal wavelength while $P^{\pm}_{i}$ indicates the forward or backward ASE power at frequency ν_i. N_{core} is the number of cores (N_{core} = 6 in the present case), while A_{core} and A_{ring} denote the signal core area and pump ring area, respectively. Since we can assume that the pump power is uniformly distributed over the whole ring with negligible loss of accuracy, the A_{core}/A_{ring} ratio represents the pump overlap factor (Γ_p). Similarly, Γ_s and Γ_i denote the overlap factors calculated under single mode condition for signal and ASE at each wavelength. We have employed a two-level energy model for the Er^{3+} ions with N_2 and N_1 denoting the populations of the up-per ($^4I_{13/2}$) and lower ($^4I_{15/2}$) levels, which leads to

$$N_2 = \frac{\dfrac{\sigma_{ap}\left(A_{core}/A_{ring}\right)P_p}{h\nu_p} + \dfrac{\sigma_{as}\Gamma_s P_s}{h\nu_s} + \sum_i \dfrac{\sigma_{ai}\Gamma_i P_i}{h\nu_{i_\lambda}}}{\dfrac{\sigma_{ap}\left(A_{core}/A_{ring}\right)P_p}{h\nu_p} + \dfrac{\left(\sigma_{as}+\sigma_{es}\right)\Gamma_s P_s}{h\nu_s} + \sum_i \dfrac{\left(\sigma_{ai}+\sigma_{ei}\right)\Gamma_i P_i}{h\nu_i} + A_{core}/\tau} N_T \quad (4.5)$$

$$N_1 = N_T - N_2 \quad (4.6)$$

where $N_t = N_1 + N_2$ is the total population corresponding to the erbium ion concentration.

4.2.3 Signal core design

Prior to designing the pump ring, the signal core parameters of the AC-MC-EDF, i.e. core radius and numerical aperture, must be selected so as to achieve decent signal gain (>20 dB) with the typical parameters shown in Table 4.2. Simulations for optimizing the core parameters con-sider a single core (N_{core} = 1) since all six cores are theoretically identical. In this initial step, we consider a conventional double cladding design [Figure 4.2(c)]. We assume that erbium ions are uniformly distributed across the core, with a 2.62×10^{25} m^{-3} concentration, while background propagation loss and ion-ion interactions are neglected. We further assume that the pump is uniformly distributed inside the pump cladding that has a 110-µm diameter and 0.46 numerical aperture (fused silica surrounded by low index polymer) as is generally the case in cladding pumping operation. A pump source at 980 nm is injected in a co-propagating configuration with respect to the signal. The pump absorption cross-section was taken to be 2.18×10^{-25} m^2. To examine small signal gain, we performed the simulations with −30-dBm input signal at 1550 nm in a 5-m long DC-MC-EDF.

Table 4.2. Simulation parameters

Item	Value	Unit	Definition
P_p	1000	mW	Pump power
P_s	−30	dBm	Signal power
λ_p	980	nm	Pump wavelength
λ_s	1550	nm	Signal wavelength
L	5	m	Fiber length
ρ	2.62×10^{25}	m^{-3}	Erbium ion concentration
σ_{as}	2.47×10^{-25}	m^2	Signal absorption cross-section
σ_{es}	3.34×10^{-25}	m^2	Signal emission cross-section
σ_{ap}	2.18×10^{-25}	m^2	Pump absorption cross-section
σ_{ep}	0	m^2	Pump emission cross-section
r_{core}	1.5~5.5	µm	Core radius
NA_{core}	0.1~0.25	-	Core numerical aperture
τ	10	ms	Upper level ($^4I_{13/2}$) lifetime

Figure 4.3(a) shows the small signal gain over a region delimited by the single-mode cut-off V = 2.405 (top right), and insufficient gain condition, i.e. G <20 dB (bottom left). As expected, the signal gain increases with core radius since the overlap factor of the pump with the doped core can be estimated by the geometric ratio $\Gamma_p = A_{core}/A_{clad}$. However, it should be noted that the NF [Figure 4.3(b)], simultaneously increases. Keeping within acceptable gain and NF values, while enforcing the single mode regime, we choose r_{core} = 4.5 µm and NA = 0.11 (marked with a cross in Figure 4.3) as the core parameters. The set of parameters r_{core} = 2.5

μm and NA = 0.15 (solid square in Figure 4.3), is used here for comparison purposes. This latter set of parameters, from a previous work [148][149], would be more representative of a core pumped EDF. Both sets yield signal gain over 20 dB at 1550 nm, the former achieves 29.07-dB small signal gain (NF = 7.45), while the latter provides 24.35-dB small signal gain (NF = 6.90) using a 1-W pump.

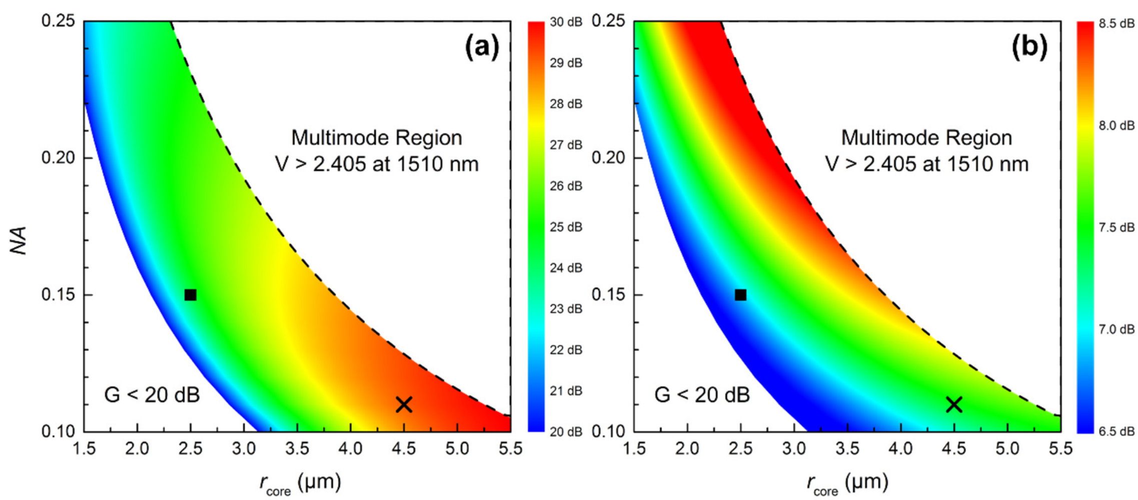

Figure 4.3. (a) Signal gain and (b) NF as a function of core radius (r_{core}), and numerical aperture (NA) for a 1-W pump. Solid square and cross represent respectively parameter sets (r_{core} = 2.5 μm, NA = 0.15) and (r_{core} = 4.5 μm, NA = 0.11).

4.2.4 Pump ring design

In order to increase the overlap between erbium ions and the pump, the thickness of the pump ring should be minimized while keeping the core diameter (d_{core}) fixed. The total thickness of the pump ring (t_{ring}) can be divided into three parts,

$$t_{ring} = d_{ring,in} + d_{core} + d_{ring,out} \tag{4.7}$$

where $d_{ring,in}$ and $d_{ring,out}$ are respectively the distances from the core edge to the inner ring side and outer ring side (Figure 4.2). The two distances ($d_{ring,in}$ and $d_{ring,out}$) have a practical limit in that their narrowing should not distort too much the signal mode field guided in the core. This impact can be estimated by calculating the relative effective index difference (F_{eff}) of the signal mode guided by the core with and without the presence of the pump ring,

$$F_{\text{eff}} = \frac{n_{\text{eff}} - n'_{\text{eff}}}{n_{\text{eff}} - n_{\text{clad,p}}} \tag{4.8}$$

where the n'_{eff} and n_{eff} denote the effective indices of the fundamental signal mode with and without the presence of a pump ring cladding. In the latter case, the refractive index of the pump ring ($n_{\text{clad,p}}$) is equal to the refractive indices of inner/outer cladding respectively [Figure 4.2(d)].

Again, we examine the properties of a single core in a pump ring cladding having a solid inner cladding [Figure 4.2(a)] or an air hole inner cladding [Figure 4.2(b)]. The results are compared to an infinite cladding [Figure 4.2(d)] in order to assess the influence on the signal mode introduced by the pump ring thickness variations. As the pump ring becomes increasingly thin, the evanescent part of the signal mode field will start to overlap with the ring cladding boundaries which can increase scattering losses of the signal due to surface roughness at these interfaces. Simultaneously, the overlap of the signal mode field with the outer and inner cladding will impact the modal effective index and we therefore use the calculated F_{eff} as a metric to verify that the signal mode is not perturbed by the presence of the ring.

First, we examined the depressed inner cladding case with fluorine-doped silica [Figure 4.2(a)] and signal core parameters set r_{core} = 4.5 μm and NA = 0.11. Figure 4.4(a) plots F_{eff} as a function of $d_{\text{ring,in}}$ and $d_{\text{ring,out}}$ that are concurrently varied from 1 μm to 11 μm. Also shown in Figure 4.4(a) is the boundary (solid white line) for which F_{eff} <1 % (top right part of the graph). These results thus indicate that if $d_{\text{ring,in}}$ and $d_{\text{ring,out}}$ are properly chosen within the F_{eff} <1 % region, the effect on the signal mode field caused by the finite pump ring thickness can be ignored. For instance, the modal field corresponding to the dot marker in Figure 4.4(a) ($d_{\text{ring,in}}$ = $d_{\text{ring,out}}$ = 1.5 μm) turns out to be elliptical, which means that it is strongly distorted, while the star ($d_{\text{ring,in}}$ = $d_{\text{ring,out}}$ = 10.5 μm) shows a perfectly symmetric modal field with signal confinement of 0.74 in the core. The different values for the minimum $d_{\text{ring,in}}$ and $d_{\text{ring,out}}$ [$d_{\text{ring,in}}$ = 4.88 μm and $d_{\text{ring,out}}$ = 5.5 μm, solid red triangle in Figure 4.4(a)] come from the different index contrast at the inner and outer cladding boundaries. Figure 4.4(b) shows similar calculations performed for the case of an air hole inner cladding, while keeping remaining parameters the same. In this case, the minimum $d_{\mathrm{ring,in}}$ and $d_{\mathrm{ring,out}}$ values are identical since the index contrast is almost the same at both boundaries. The minimum value of ring thickness, t_{ring} = 20.86 μm, indicated by the open red triangle in Figure 4.4(b), corresponds to $d_{\mathrm{ring,in}}$ = 5.86 μm and $d_{\mathrm{ring,out}}$ = 6.0 μm.

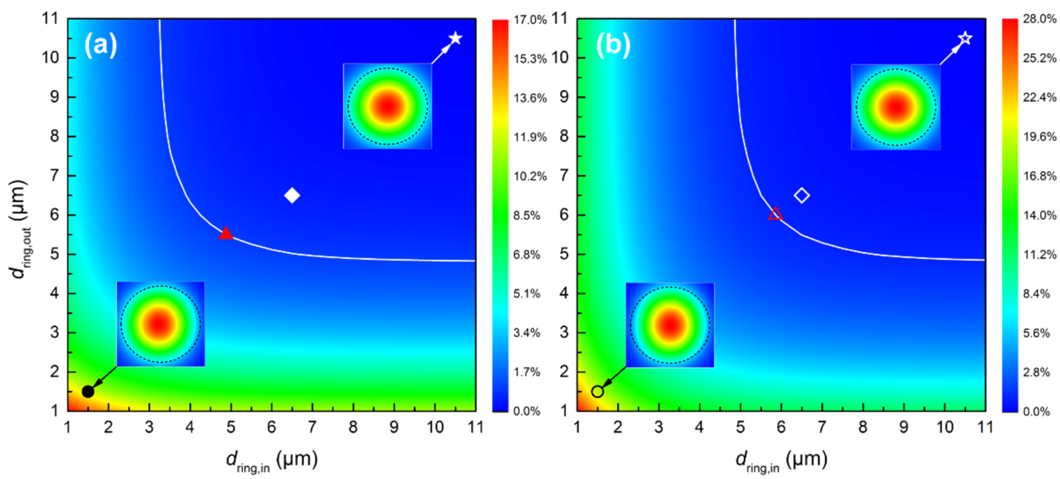

Figure 4.4. Relative effective index difference (F_{eff}) as function of $d_{\mathrm{ring,in}}$ and $d_{\mathrm{ring,out}}$ for (a) a solid inner cladding and (b) an air hole inner cladding. The white solid line corresponds to F_{eff} = 1 %. Star, diamond and circle represent $d_{\mathrm{ring,in}} = d_{\mathrm{ring,out}}$ = 10.5 μm, 6.5 μm and 1.5 μm, respectively. Insets show the signal mode field profile corresponding to small and large values of F_{eff}.

In most cases of cladding pumping, assuming that all the pump power is confined in the cladding ring and furthermore considering its largely multimoded , an indicator of the pump power savings, P_{e}, enabled by the ring design can be estimated by,

$$P_{\mathrm{e}} = \frac{A_{\mathrm{clad,in}}}{A_{\mathrm{clad,in}} + A_{\mathrm{ring}}} \tag{4.9}$$

where $A_{\mathrm{clad,in}}$ and A_{ring} are respectively the inner cladding and pump ring areas (Figure 4.1). We find that P_{e} = 0.21 (i.e. saving 21 % power) can be achieved through annular pump cladding with $d_{\mathrm{ring,in}} = d_{\mathrm{ring,out}}$ = 10.5 μm (solid and open star in Figure 4.4). Alternatively, a factor

$P_e = 0.32$ can be achieved for $d_{ring,in} = d_{ring,out} = 6.5$ µm (solid and open diamond in Figure 4.4). With the minimum ring thickness, the annular-cladding design could reduce the required pump power by up to 38 % [red triangle in Figure 4.4(a)] compared to a conventional geometry without annular-cladding.

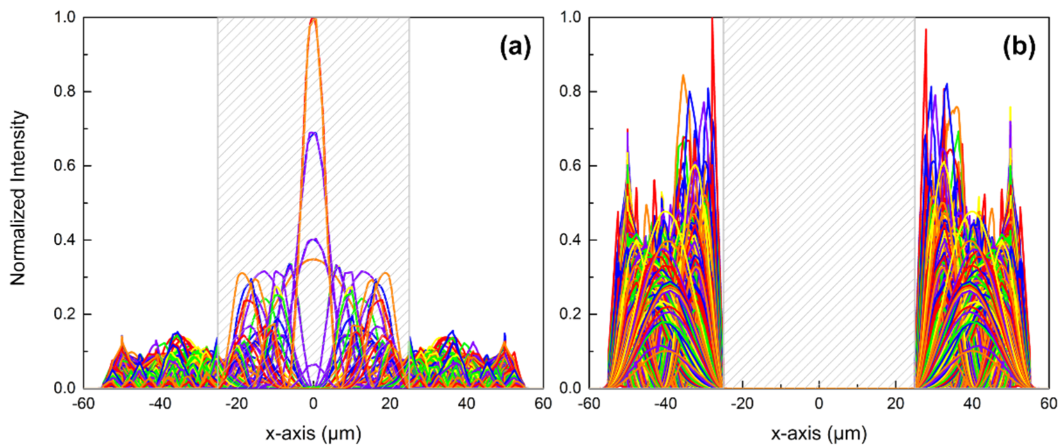

Figure 4.5. Normalized intensity distributions (along x-axis, from view A in Figure 4.1. Transverse cross-section of AC-MC-EDF showing: the annular pump cladding (dark gray), doped cores (blue), depressed inner cladding (gray), and outer cladding (light gray).) of the first 500 modes for (a) solid and (b) air hole inner claddings.

As indicated in Figure 4.4, although the minimum ring thickness of the air hole scheme is thicker than the solid inner cladding one, it is expected that the former will enable stronger pump power confinement within the pump ring than the latter that is likely to show pump power leakage into the inner cladding. To verify this assumption, we calculated the first 500 pump modes of the ring cladding without signal cores and with $d_{ring,in} = d_{ring,out} = 10.5$ µm using COMSOL® for both solid [Figure 4.2(a)] and air hole [Figure 4.2(b)] inner cladding. The normalized intensity of each mode along an axis cutting through the center of the fiber (in this case the x-axis along line A in Figure 4.1. Transverse cross-section of AC-MC-EDF showing: the annular pump cladding (dark gray), doped cores (blue), depressed inner cladding (gray), and outer cladding (light gray).) are plotted in Figure 4.5 where shaded gray area represents the inner cladding region. Modes are normalized to carry unit power. The calculations confirm that no guided mode exist in the inner cladding in case of air hole [Figure 4.5(b)] contrary to a solid inner cladding [Figure 4.5(a)]. Assuming all the 500 modes are equally excited, there would be 8 % (average) of total power contained in solid inner cladding, the power fraction of solid inner cladding for some HOMs can reach 95 %. In section 4.4, we will re-examine this issue via simulations using the beam propagation method (BPM). Practical limitations of our current in-house fiber fabrication methods (preform produced by MCVD and stack-and-draw) require that tring ≳ 30 μm. In this particular instance, diamond markers in Figure 4.4 identify manufacturing compliant parameters. As previously discussed, $n_{clad,in}$ is also limited by the maximum amount of fluorine that can be incorporated into the silica glass giving $n_{clad,in}$ = 1.43812 at λ = 1550 nm. The final parameters of the proposed AC-MC-EDF design are listed in Table 4.3.

Table 4.3. AC-MC-EDF parameters

Item	Value	Unit	Definition
r_{core}	4.5	μm	Core radius
NA_{core}	0.11	-	Core numerical aperture
n_{ring}	1.44402	-	Pump ring index
$\Delta n_{clad,in}$	5.9×10^{-3}	-	Inner cladding index difference
$n_{clad,out}$	1.37	-	Inner cladding index
Λ	40	μm	Core pitch
$d_{ring,in}$	10.5	μm	Core edge to ring inner side
$d_{ring,out}$	10.5	μm	Core edge to ring outer side

4.3 Amplification performance simulation

Using the model described in Section 4.2.2, we now examine the gain and NF of the proposed MCF designs with cladding pumping. We inject pump powers from 0.5 W to 1.5 W in the annular-cladding, while the signal (1550 nm) input power is set at −30 dBm. For each pump power value, we find the optimum fiber length and calculate gain and NF. We assume six identical cores (N_{core} = 6). Results are shown in Fig. 6 for the proposed AC-MC-EDF design with the parameter sets identical to the ones identified by the same solid markers (diamond and star) in Figure 4.4(a), while the open markers correspond to a standard DC-MC-EDF [i.e. $n_{\mathrm{clad,in}} = n_{\mathrm{clad,p}}$, Figure 4.2(c)] but with otherwise the same parameters. For the AC-MC-EDF, the model assumes that all the pump power is uniformly distributed in the annular-cladding and there is therefore no distinction between the air hole and depressed-index silica inner claddings. Figure 4.6(a) indicates that for a given gain level, for example 30 dB, the AC-MC-EDF requires 1.1 W of pump power, which is 300 mW less than the DC-MC-EDF. For the same pump power, considering pump power levels producing >20-dB gain, the AC-MC-EDF achieves between 4 to 10-dB higher gain than the DC-MC-EDF, as well as a lower NF at all pump levels (especially for P_{p} <1.1 W). Note that NF calculations are performed for conditions leading to G >10 dB. Furthermore, the thinner pump ring scheme (diamond in Figure 4.4), i.e. $d_{\mathrm{ring,in}} = d_{\mathrm{ring,out}} = 6.5$ µm, achieves up to 8-dB better gain than a thicker one (star in Figure 4.4).

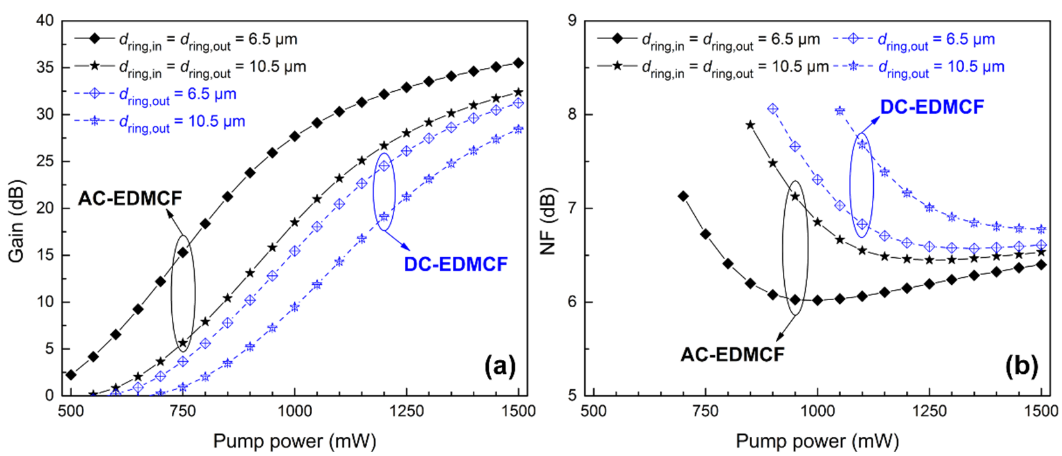

Figure 4.6. Signal gain (a) and NF (b) against input pump power from 0.5 to 1.5 W. Star and diamond markers correspond to the two pump ring parameter sets found in Figure 4.4, solid markers are for AC-MC-EDF and open ones for DC-MC-EDF.

The saturated output power is calculated for 1-W pump and optimized fiber length (calculated for a −30-dBm input signal power). We varied the input signal power from −50 dBm to 10 dBm, at 1550 nm with results shown in Figure 4.7. Again, for each input signal power, the AC-MC-EDF achieves better gain, e.g. 12 dB more at −30 dBm, as well as smaller NF.

The dynamic range associated with saturated input power (defined for the 3-dB gain compression), for AC-MC-EDF is narrower than a DC-MC-EDF. Design optimization towards increasing the saturation output power, as can be required for WDM inline amplifiers, will require further investigation.

A usual performance metric for EDFAs with in-core pumping is the power conversion efficiency (PCE) defined as $PCE = (P_{s,out} - P_{s,in})/P_p$, where P_s,out is the output signal power. In the case of cladding pumping, where the pump power is typically larger than the signal power by three orders of magnitude, we propose the modified PCE_{clad} defined as,

$$PCE_{clad} = \frac{PCE}{\left(A_{core} / A_{clad,p} \right)} \tag{4.10}$$

Figure 4.8 shows the PCE_{clad} against pump power for AC-MC-EDF and DC-MC-EDF with different cladding parameters. Fig. 8 indicates that at high pump power the proposed annular-cladding design improves pump power utilization significantly, e.g. about 16 times higher PCE_{clad} than a comparable DC-MC-EDF with 1 W of pump power for $d_{ring,in} = d_{ring,out} = 6.5$ µm. Compared to thicker pump ring scheme ($d_{ring,in} = d_{ring,out} = 10.5$ µm), a thinner ring enables a more efficient usage of pump power, i.e. more net signal gain is obtained per unit pump power (1 mW).

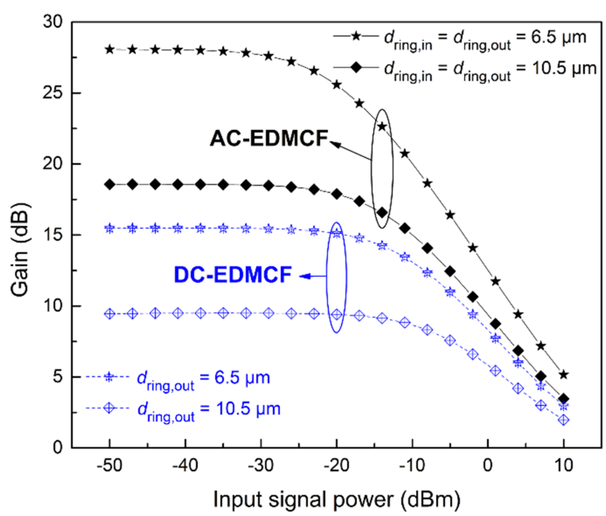

Figure 4.7. Signal gain against input signal power from −50 to 10 dBm. Star and diamond represent the two pump ring parameter size sets in Figure 4.4. Solid markers are for AC-MC-EDF and open ones for DC-MC-EDF.

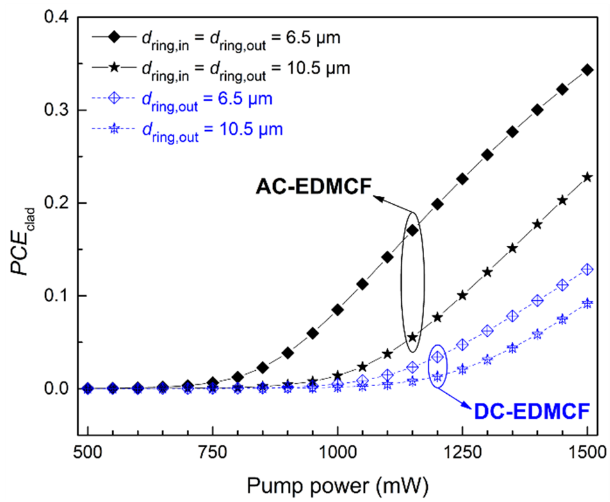

Figure 4.8. PCE_{clad} against pump power for AC-MC-EDF and DC-MC-EDF.

4.4 Pump injection scheme

Unlike the conventional DC-MC-EDF, in which the center cladding area can be fed by a multimode pump laser [17], we propose an alternate method to couple the pump in our annular-cladding fiber using multiple injection spots. In this scheme one could simultaneously inject the pump and the signals, through modern coupler fabrication techniques such as TFBs [150] or 3D photo-written waveguides [151], by strategically locating pump injection spots between the cores.

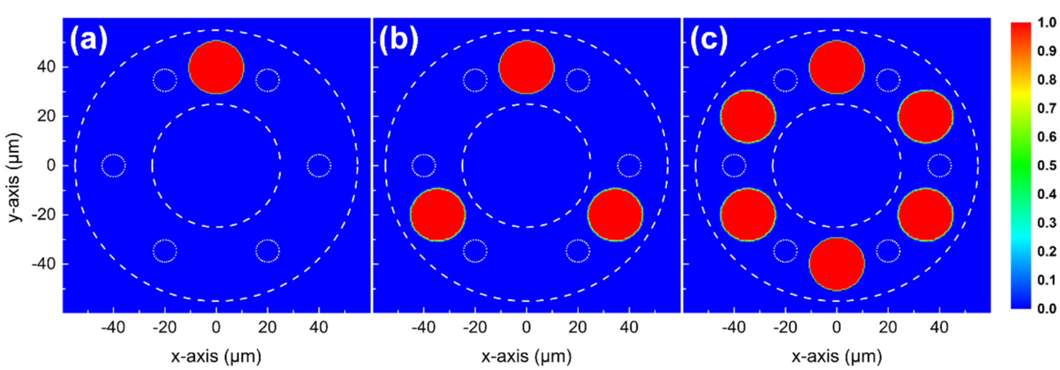

Figure 4.9. Pump (980 nm) injection by imaging multiple spots with flat-top intensity pro-files on the AC-MC-EDF showing (a) a single spot, (b) three spots and (c) six spots. White dashed circles represents the limits of the annular pump cladding, while the six white dotted circles indicate the positions of the signal core.

Here, we examine three configurations of multi-spots injection of the pump in the cladding. We consider that the spots are mutually incoherent and model the multimode field of each spot as a 20-μm diameter flat-top intensity profile (with uniform phase). Figure 4.9 shows the injection pattern with one spot [Figure 4.9(a)], three spots [Figure 4.9(b)] and six spots [Figure 4.9(c)]. In all cases, the pump is injected half-way between cores. In the case of three spots and six spots, the phase of each spot is chosen randomly between 0 and 2π before we per-form BPM simulations (OptiBPM®) over a maximum propagation length of 40 mm.

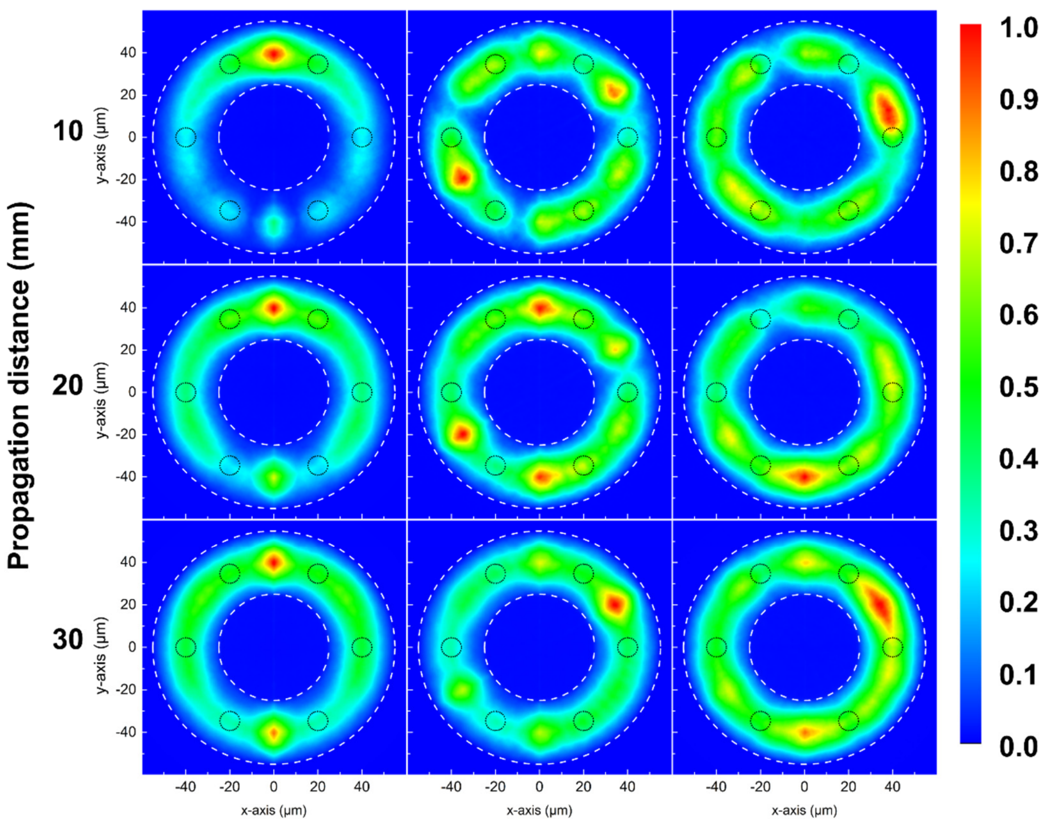

Figure 4.10. Normalized length averaged intensity distributions after 10, 20, and 30 mm propagation through the annular-cladding with (a) single spot, (b) three spots and (c) six spots injection scheme. White dashed circle represents the limits

of the annular pump cladding and the six black dotted circles indicate the position of the signal cores.

We propagated the field along the fiber and calculated the intensity distributions after each 100 µm along the z-axis. We then performed a summation of all intensity distributions over a length of 10 mm and then the summation was normalized. Figure 4.10 illustrates this length averaged intensity distributions after 10-mm, 20-mm, and 30-mm long pump power propagation. As we can see in Figure 4.10, after propagating over a length of 20 mm in the AC-MC-EDF, the average intensity in the cladding is already well distributed across the annular-cladding (dashed white circle). Because of the uniform phase front assumption of the input pump field, the injection into the multimode annular-cladding can lead to a self-imaging phenomenon (Talbot effect) as shown, for example, in the single spot excitation of Figure 4.10(a). In a practice, we expect the multimode pump laser input to have a random phase for each mode, which would result in a uniform pump power distribution. This simulation shows that the injected pump power gets rapidly distributed across the cladding.

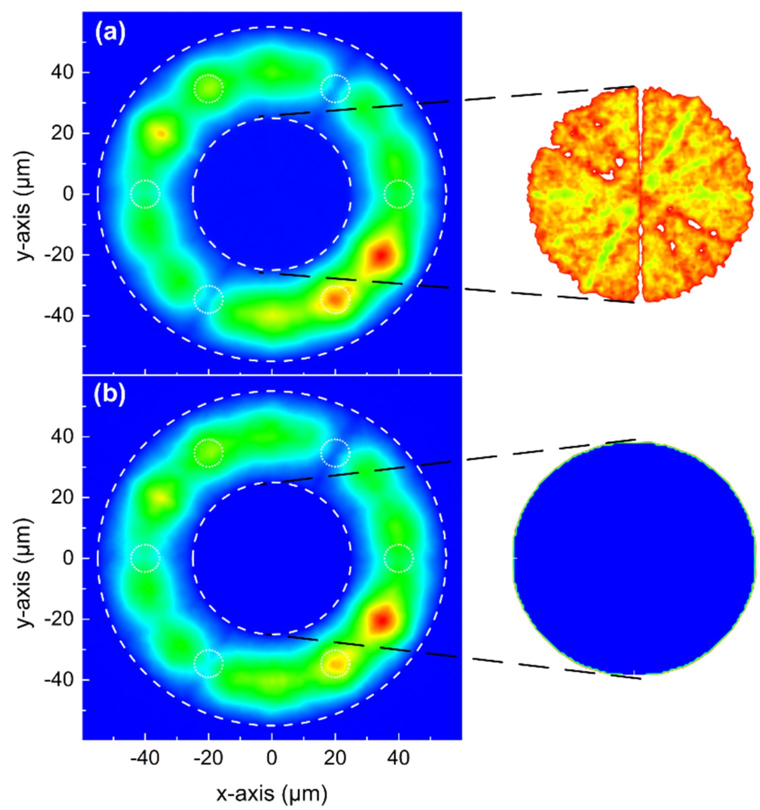

Figure 4.11. Zoom-in of the normalized average intensity distributions with six-spot injection after 40-mm propagation through the annular-cladding for (a) ACS-MC-EDF (solid inner cladding) and (b) ACA-MC-EDF (air hole inner cladding).

Using BPM simulations, we examined if the injected pump power leaks into the inner cladding region (six-spot excitation after 40 mm). As predicted in Section 4.2, we observed a small amount of pump power leaking to the inner solid silica cladding [Figure 4.11(a)], while the pump power is well confined within the annular pump cladding when the inner cladding is an air hole [Figure 4.11(b)].

Besides the end-facet signal and pump injection, the side-coupling of pump power is another option that has been investigated for double cladding single core fibers. Before applying the technique on MCF, one needs to be aware that most of these techniques, such as v-groove coupling [152], require precise mechanical alignment and can suffer from stability issues, with the exception of the side-coupling tapered-fused fiber combiner [153]. Furthermore, owing to the multicore fiber structure, either methods can perturb the signal cores due to their close proximity to the cladding boundary [88]. Such a side-coupling pump injection scheme has recently been used to pump a multicore amplifier with multimode cores demonstrating the potential of this technique for annular-cladding fibers [90].

4.5 Conclusion

We proposed a six-core EDF with an annular-cladding design to increase the pumping efficiency of cladding pumped MCF amplifiers. After optimizing the signal core parameters (core size and NA), we investigated and compared several cladding designs that efficiently confine and guide the pump. The dimensions of the annular-claddings were chosen so as to reduce the perturbation of the signal core modes. The annular-cladding designs include an inner cladding index depression formed by either doping the silica glass with fluorine or by placing an air hole in the central region of the fiber. Both of these designs comply with practical considerations related to preform fabrication with MCVD. The proposed design demonstrates lower pump power requirements compared to standard double cladding design. Simulations also indicate that the annular-cladding MCF design is superior in terms of gain and NF as well as power conversion efficiency, given similar core parameters. As with all MCF proposals, combination of pump and signals poses important challenges. Cladding pumping enables the use of multimode laser diodes delivering high pumping power that can be shared between cores. An end-facet multi-spot pump injection configurations could be used to deliver one to six pump beams in the cladding. BPM simulations indicate that multi-spots injected pump power will spread rapidly in the annular-cladding so as to pump all cores. Other possibilities, such as side-coupling, could also be applied.

4.6 Acknowledgement

This work was supported by the Canada Research Chair in Advanced photonics technologies for communications (APTEC), by the Canada Excellence Research Chair in Enabling Photonic innovations for information and communications (CERCP) and by the Natural sciences and engineering research council of Canada (NSERC). C. Jin acknowledges the support of the China Scholarship Council.

4.7 Supplementary information

In this section, the measured parameters of the two fibers fabricated at COPL (2120B2 and 2120C2) are first shown in Table 4.4. Following, we compared the pump confinement between the conventional double cladding and the proposed annular-cladding by mean of ray-tracing. At last, the amplification performance such as signal gains, NFs of both solid depressed-index and air-hole cases are experimentally evaluated and the results are discussed.

4.7.1 Fiber parameters

Table 4.4. Measured fiber parameters of 2120B2/C2

Item	Value	Unit
r_{core}	4~5	μm
Λ	40	μm
$r_{\mathrm{clad,in}}$	29.5~30	μm
r_{ring}	54.5~55	μm
$r_{\mathrm{clad,out}}$	70	μm
$\mathrm{NA}_{\mathrm{core}}$	0.104	-
ρ	2.8×10^{25}	m^{-3}

4.7.2 Cladding pumping scheme ray-tracing simulations

We use ray-tracing implemented in ZEMAX to simulate the side-pump coupling scheme in order to evaluate both the side-pump coupling efficiency, and the pump confinement within the annular-cladding. The EDF was placed in physical contact with a down-tapered coreless fiber (diameter is tapered from 125 μm to 20 μm, over 35 mm). 500,000 rays are launched into the coreless fiber from a source at the input facet. The detector is placed at the end of both the multicore fiber and the coreless fiber, and the pump power distribution is calculated by counting the number of rays in the transverse cross-section. Figure 4.12 depicts the simulation results for EDFs (without cores) with: (a) uniform cladding, (b) annular-cladding with solid inner cladding and (c) annular-cladding with air-hole inner cladding. The results show increased pump intensity for both annular-cladding cases compared to uniform cladding (no inner cladding). Moreover, the air-hole produces the largest pump confinement due to the large index contrast between annular-cladding and inner cladding. The results indicate that the solid case and air-hole case obtain 7 % and 40 % more pump intensity in the cores locations, respectively.

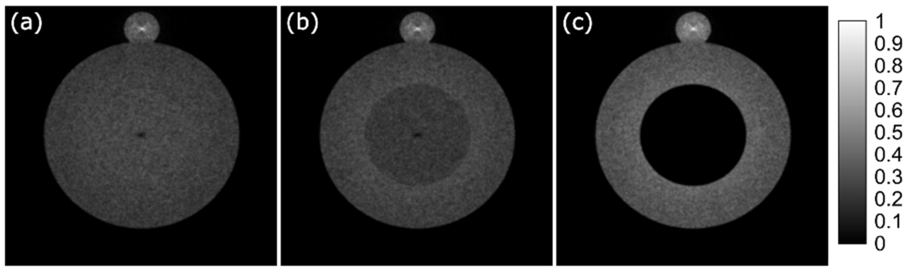

Figure 4.12. Simulation of the pump power distribution for (a) uniform cladding; (b) annular-cladding with solid inner cladding; (c) annular-cladding with air-hole inner cladding.

We fabricated side-couplers for a 1-m EDFs and observed the pump distribution using 980 nm multimode pump lasers. The beam patterns are shown in Figure 4.13. The cores appear as six black dots due to pump light absorbed by erbium ions. The intensity distribution in the ring matches with the simulation well.

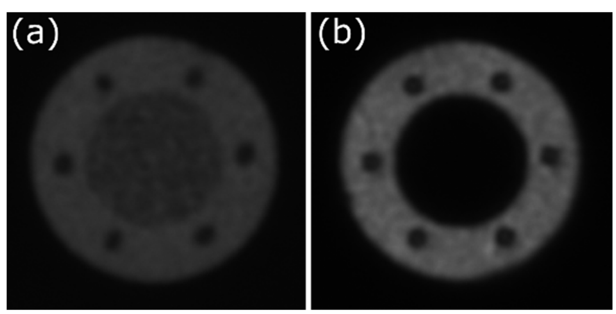

Figure 4.13. Output beam pattern with multimode side pumping at 980 nm for (a) annular-cladding with solid inner cladding; (b) annular-cladding with air-hole inner cladding.

4.7.3 Characterization of the depressed solid-glass cladding and air-cladding AC-MC-EDFs

Figure 4.14 shows the six-core EDFs characterization setup for co-propagating pumping. The signal is an eight-channel WDM laser source that covers the C-band, and has an output power of −12 dBm per wavelength. The multimode laser diode (LD) for cladding-pumping emits 25 W at 980 nm. The side-pumping coupling efficiencies are measured to be 65 % for the solid case and 62 % for the air-hole case, respectively. The SMF at the input and output is butt-coupled into the 2.1-m long six-core EDFs. Two isolators are utilized in order to avoid reflections from the WDM source and the optical spectrum analyzer (OSA) used to measure the output spectrum of the fiber under test (FUT). Unused cladding pump light is dumped via a cladding pump light stripper (CPLS) made by cladding surface etching. Counter-propagation pumping characterization is accomplished by switching point A and B in the setup.

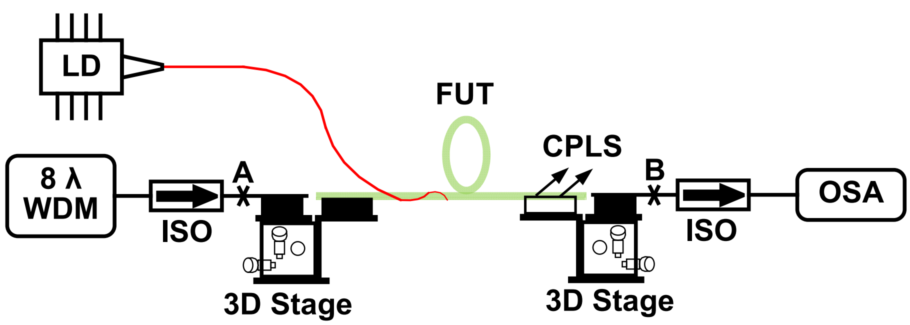

Figure 4.14. Experimental setup to characterize the six-core EDFs.

At 15-W coupled pump power (25 W × 60 %), both amplifiers achieve more than 19-dB gain and less than 6-dB NF per core across the C-band, as shown in Figure 4.15. The gain variation between cores is less than 2 dB. The amplifier with an air-hole inner cladding achieves 1.5-dB more gain due to the stronger pump confinement and a similar NF. The counter-propagating configuration has 0.5-dB more gain than co-propagating pumping at short wavelengths because it provides pump power to the input of the fiber where the signal is injected, while in the latter case a short fiber length before the side-coupling section remains unpumped (about 0.1 m). The maximum signal output power is above 20 dBm. Taking into account all the cores, the power conversion efficiency is about 4 %.

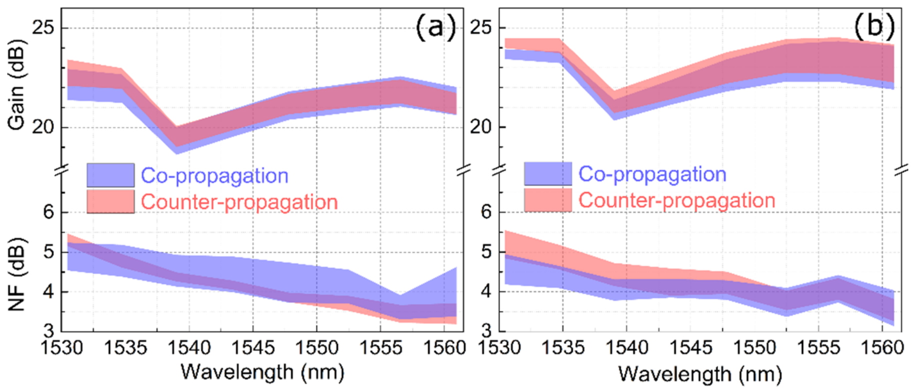

Figure 4.15. Range of internal gains and NFs of co- and counter-propagating pumping for (a) annular-cladding with depressed-solid center; (b) annular-cladding with air-hole center.

4.8 Summary

In this chapter, we proposed and discussed the annular pump cladding design for the MC-EDF and the multi-spot edge-coupled cladding pump scheme. In the supplementary information, the enhanced pump confinement enabled by the proposed design was evaluated by the ray-tracing simulation. Afterwards, the two types of fabricated MC-EDF were characterized incorporating with side coupled cladding pumping scheme. Results show that the air-hole case provider better gain than the solid case.

Chapter 5

Spatially Integrated Optical Fiber Amplifier

Abstract

SDM using spatial channels in MCFs and MMFs can increase the transmission capacity per optical fiber so as to avert the impending '*capacity crunch*' and reduce the cost per bit at the same time. With recent record-breaking SDM transmission experiments, realization of integrated SDM components with complexity and cost that scale sublinearly with the SDM channel count has come to the forefront. We demonstrate a cladding-pumped six-core three-mode EDFA that can amplify 18 spatial channels with a complexity similar to a single-mode EDFA. The amplifier delivers >20-dBm total output power per core and <7-dB NF over the C-band. This cladding-pumped EDFA enables combined space-division and wavelength-division multiplexed transmission over multiple MMF spans.

Résumé

Le SDM basés sur des canaux se propageant dans des fibres multi-cœurs et multimodes peut augmenter la capacité de transmission des fibres optiques de manière à éviter la pénurie de largeur de bande et simultanément réduire le coût de transmission par bit d'information. Suite aux expériences récentes de transmission SDM, la réalisation de composants SDM intégrés permettant de réduire la complexité et les coûts des systèmes en fonction du nombre de canaux devient primordiale. Nous démontrons un amplificateur à fibre dopée à l'erbium ayant six cœurs, chacun comportant trois modes. La fibre, pompée dans la gaine, peut amplifier 18 canaux spatiaux avec une complexité similaire à un amplificateur classique à un seul cœur. L'amplificateur est caractérisé par une puissance de sortie totale >20-dBm par cœur et un facteur de bruit <7-dB de bruit sur la bande C. Cette fibre multi-cœur à double gaine permet de combiner le multiplexage spatial et le multiplexage en longueur d'onde sur plusieurs tronçons de fibre multimodes et multi-cœurs.

5.1 Introduction

Bandwidth demands for optical networks are growing exponentially and will exceed the maximum achievable capacity of a SMF due to fiber nonlinearities [154], resulting in a '*capacity crunch*'[11] in the near future. The simplest way to avert the '*capacity crunch*' is to use multiple SMF transmission systems in parallel. However, this most basic form of SDM duplicates all the optical amplifiers, ROADMs, and transponders for each additional fiber and has linear cost and complexity scaling. Alternatively, SDM that uses the spatial domain for integration can provide similar capacity increase but with great potential for reducing the cost per bit of transmission. Some examples are fibers with enlarged cores that support multiple spatial modes [44][54], fibers with multiple cores [155][55], wavelength switches that switch all cores/modes simultaneously [144], and optical fiber amplifiers [117][156].

In the past five years, tremendous progress has been made in both SDM components and SDM transmission. Spatial degrees of freedom have increased from three modes to 15 modes in MMFs, from three cores to 36 cores in MCFs. Over 2 $\mathrm{Pbit{\cdot}s^{-1}}$ transmission over 100 spatial channels in MC-FMFs [57][60] have been demonstrated. Different types of spatial multiplexers based on bulk optics [157], fused fiber bundle [158][159], laser-inscribed 3-dimensional waveguide devices[160][161], photonic integration [162][163] and multi-plane light conversion [79] have enabled efficient connections between multiple SMFs and SDM fibers. Efforts to reduce receiver computational complexity due to MIMO processing include MMFs with low DGMD and low inter-mode group coupling [164][165] as well as MCFs with <−40-dB core-to-core cross-talk [166][167].

As for SDM optical amplifiers, core-pumped multimode and multicore EDFAs have previously been used for WDM/SDM [168][169]. However, core pumping requires almost the same number of pump diodes as the number of cores and offers only a slight reduction in complexity and costs compared to duplicating SMF amplifiers. Cladding-pumped amplifiers can significantly reduce the complexity and cost of multi-spatial channel amplifiers [105][170][171][118]. In cladding-pumped amplifiers, the pump light is coupled to the cladding modes independently from the core modes, which eliminates wavelength combining elements and also enables simple pumping schemes. For instance, side-pumping [153] does not require access to the fiber facet but rather couples pump light into the cladding modes through the side of the fiber (Supplementary Information 'Side-pumping'). The pump light illuminates all cores, see Figure 5.1(a), eliminating the need for a separate pump diode per core. Moreover, uniform illumination of the cores simplifies modal gain equalization. The main drawback which has to be overcome with cladding-pumped amplifiers is the reduced pump power conversion efficiency since the illuminated cladding area is much larger than the core area.

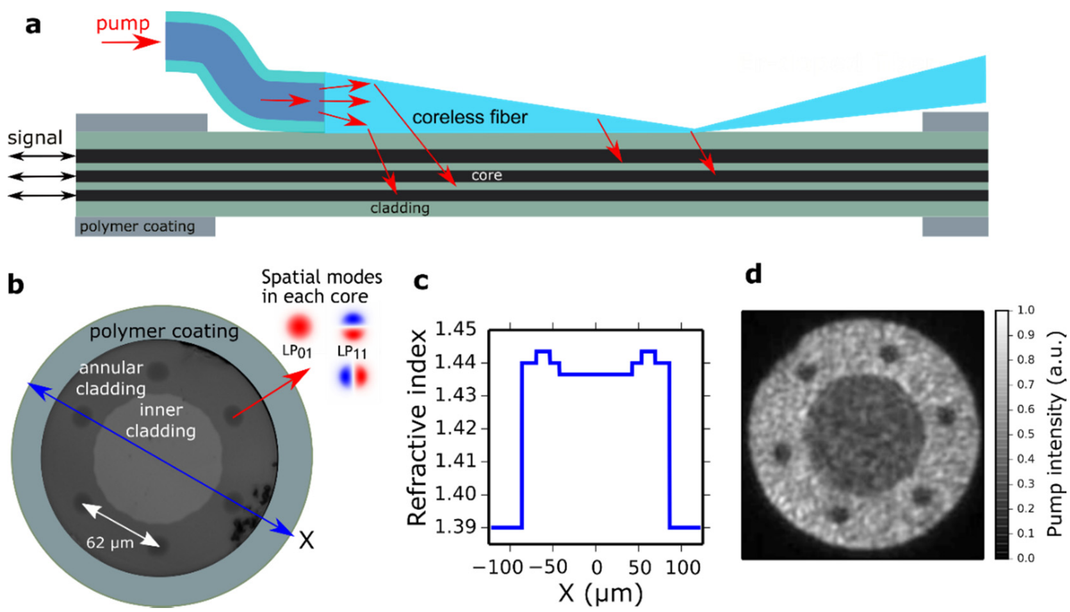

Figure 5.1. Cladding-pumped six-core EDFA. (a) Schematics of side-pumping. (b) EDF facet image. (c) Refractive index profile of EDF. (d) Output pump intensity distribution with multimode side pumping at 980 nm.

In this chapter, we explore integrated SDM optical amplifiers that can amplify many spatial channels and therefore significantly reduce the complexity and cost of SDM transmission systems. We designed and fabricated an annular-cladding six-core EDF as shown in Figure 5.1(b) to increase pump power conversion efficiency. This work demonstrates amplification of 18 spatial channels (six cores with three spatial modes each) using only a single optical pump. The inner cladding is a depressed-index region able to prevent pump light from entering the central region due to total internal reflection. This enhances the pump intensity around the cores in the annular-cladding and can save more than 25 % pump power compared to a uniform cladding (Supplementary Information ‘Pump power for strong population inversion’), enabling a >20-dBm output power per core and <7-dB NF over the entire C-band. This amplifier was used in a 120-km WDM/SDM transmission experiment comprised of three amplified spans.

5.2 The annular-cladding six-core erbium-doped fiber

The refractive index profile along the x-axis Figure 5.1(b) of the annular-cladding six-core EDF is illustrated in Figure 5.1(c). The fabrication of the six-core EDF is addressed in detail in Supplementary Information ‘Fiber preparation and fabrication’. Each core supports the LP_{01} mode and the two degenerated LP_{11} modes in the C-band (Supplementary Information ‘Fiber parameters’). To achieve high output power per spatial channel, which can only be accomplished if the EDFA maintains a high ratio of pump intensity to signal intensity throughout the gain medium so that it is not saturated, we designed core and cladding refractive indices to provide larger mode areas, which reduces the signal intensity without affecting the pump intensity. The calculated mode field areas are 168 μm^2 and 179 μm^2 for the LP_{01} and LP_{11} mode group, respectively, which are much larger than that of SMFs. The nearly identical mode fields also contribute to minimizing the MDG, which was measured to be less than 2 dB [Figure 5.9(c)]. We demonstrated that the average pump intensity in the annular-cladding compared to the inner cladding is enhanced by a factor of 1.45 as shown in Figure 5.1(d) which contributes to lower NFs through full population inversion at the input of the amplifier. It was verified that the annular-cladding has negligible impact to the side-pump coupling efficiency, which is around 96 % similar to that of the uniform cladding. (Supplementary Information ‘Ray-tracing simulation’)

5.3 Annular-cladding six-core erbium-doped fiber characterization

Figure 5.2(a) and b show the internal gains (excluding input and output coupling losses) and NFs for one of the six cores as functions of coupled-pump power in the forward-pumping configuration (Supplementary Information ‘Gain and NF measurements’). Figure 5.2(c) and d show the range of internal gains and NFs for all six cores with a coupled-pump power of

15 W and total input signal power of −12 dBm and −2 dBm, respectively. The cladding-pumped six-core EDFA provides an output power of >20 dBm per core and <7-dB NF over the C-band for the LP_{01} mode. The gain and NF deviations of 1 dB are mainly attributed to the inaccuracy in the measurements of input and output coupling losses. Performance discrepancies, especially for NFs at short wavelengths can be observed between forward and backward pumping, which can be attributed to inadequate pump power for forward pumping at the input where the coreless fiber starts to be wrapped around the EDF. This slight deficiency can be eliminated by either using bi-directional pumping or couple the pump into a passive fiber with an identical structure to the EDF first. We replaced the SMF at EDF output

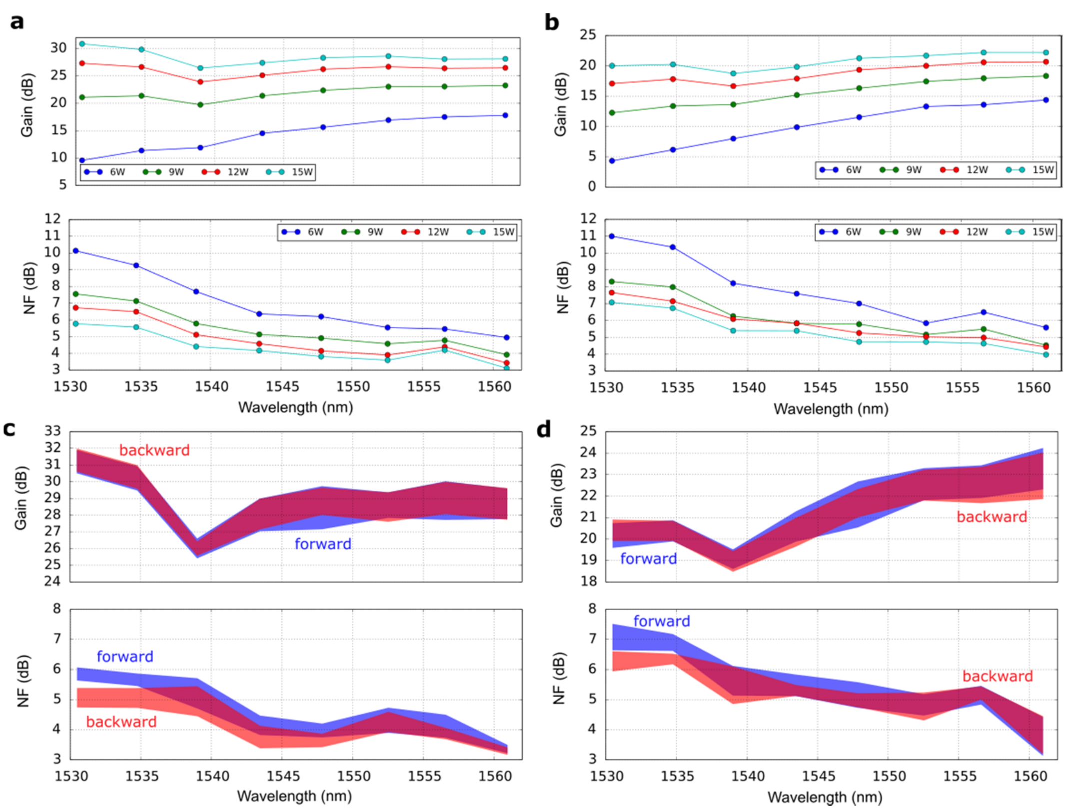

Figure 5.2. Internal gain and NF characterization. (a),(b) Results for LP_{01} mode of one core in a forward-pumping configuration with a total input power of −12 dBm and −2 dBm, respectively as a function of coupled-pump power. (c),(d) Range of internal gains and NFs in both forward and backward pumping for all six cores with a total input power of −12 dBm and −2 dBm, respectively.

with a 50/125-μm MMF to detect the output power for all three spatial modes as all the modes are excited at the same time, each with −2-dBm input power. It was measured that 22-dBm output power can be provided by each core with 15-W pump power coupled into the cladding.

To use each core as an independent amplifier, it is essential to have negligible core-to-core cross-talk and pump-depletion-induced cross-talk. The worst-case core-to-core cross-talk for a connectorized six-core EDFA was measured to be better than −35 dB, which is mainly attributed to fabrication errors of tapered fiber bundles (Supplementary Information "Cross-talk") and can be further minimized through fabrication optimization. The ratio between signal core area and cladding area is 1.2 %. A benefit of this small overlap of the gain medium with the pump is negligible pump depletion which avoids pump-depletion-induced cross-talk. No pump-depletion-induced cross-talk was observed under different signal loading conditions [Figure 5.9(c)].

Figure 5.3(a) shows the overview of the multi-span MMF transmission experiment empowered by the cladding-pumped six-core EDFA. The 120-km fiber link contains four graded-index MMF spans each supporting three spatial modes at 1550 nm. Figure 5.3(b) depicts how all six amplifying cores were used for either forward or backward transmission. In the forward direction, a different core was used for amplification between the MMF spans (cores 1, 2 and 6). In the backwards direction, for the three remaining cores, dummy channels were launched to fully load the amplifier. The six MMFs of each fan-out were spliced to the MMF spans. The amplifier was operated with 8-W fiber-coupled power to compensate the losses from the transmission MMF and the fan-outs.

The transmitter which produced eight wavelengths spaced at 100 GHz is illustrated in Figure 5.3(b). The even and odd wavelengths were separately modulated by independent 30-GBaud QPSK waveforms with Nyquist pulse shaping and the WDM comb was then polarization multiplexed. 12 independent launch signals were prepared by splitting and delay decorrelating the WDM comb and were coupled into the six spatial and polarization modes of the MMFs using mode-group selective photonic lantern based spatial multiplexers (SMUXs).

Optical attenuators were used to equalize the input signal power into each core. The combined SDM and WDM forward signal was transmitted through three cores of the amplifier over 35-km MMF after the first and second stage, and 25-km MMF after the transmitter and another 25-km MMF in front of the receiver. At the receiver, the forward SDM signals were demultiplexed by another photonic-lantern-based SMUX and fed to three polarization-diversity-multiplexed coherent receivers operating at 40 GS·s^{-1}. MIMO-based offline DSP was applied to recover the signals (Supplementary Information 'Data processing').

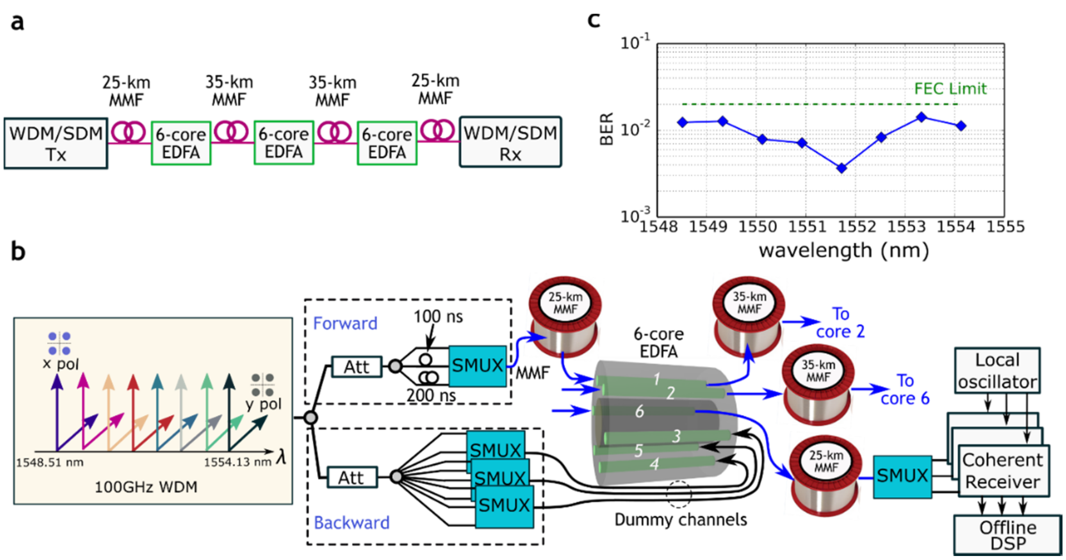

Figure 5.3. Multi-MMF span transmission. (a) Overview of multi-MMF span with four MMFs and three amplifying cores. (b) Transmission setup includes a WDM/SDM transmitter for generating signal and dummy channels, 120-km transmission link with one in-line six-core EDF and SDM receiver. (c) BER for eight WDM channels.

Figure 5.3(c) shows the BER curves for all wavelength channels averaged across all spatial modes after the 120-km MMF span which are below the 2×10^{-2} forward error correction (FEC) limit for all wavelengths with a total capacity of 2.4 Tb·s^{-1}. After 120-km transmission, the optical-signal-noise ratio (OSNR) was larger than 17 dB compared to the OSNR of 35 dB at the transmitter output, which provides an equivalent NF of 6 dB per core considering fiber losses and coupling losses (Supplementary Information 'Equivalent NF').

The transmission reach was constrained by the accumulated MDL around 26 dB, induced at each splicing point between the six-core EDF and the fan-in/fan-out due to mode-profile mismatch and pitch deviation after down-tapering (Supplementary Information 'Mode dependent loss'). Through optimizing the tapering parameters and using fibers with identical mode profiles, we should be able to minimize the accumulated MDL in addition to employing differential group delay-compensated MMF spans to increase transmission reach. This work presents a novel type of EDF using both cores and modes which is scalable to support a large spatial channel count and can be an efficient and low-cost solution for integrated optical amplification. The depressed-index region is not limited at the center and can be separated and distributed at any location of the cladding. Through increasing the refractive index contrast between the cladding region containing cores and the depressed-index region or using air-hole for the depressed-index region, pump power conversion efficiency can be further enhanced.

5.4 Supplementary Information

5.4.1 Pump power for strong population inversion

Low NF and high gain can only be obtained through strong population inversion. In the absence of an input signal and neglecting ASE in a short fiber segment, the required pump power to achieve an inversion ratio of η can be calculated as [87] : $P = \eta[(h\nu A_{21}/\sigma_{13})A_{clad}]/(1-\eta)$, where h is the Planck's constant, ν is the pump light frequency, A_{21} = 100 s^{-1} is the spontaneous emission rate, σ_{13} =2.18 × 10^{-25} m^2 is the pump absorption cross-section at ν (corresponding to 980 nm), A_{clad} is cladding area over which the pump is distributed.

A low NF requires a population inversion >90 % [87][156]. For an optical fiber with the pump power uniformly distributed in a cladding with a diameter of 170 µm, this low NF constraint requires approximately 18 W of pump power. For the designed annular-cladding six-core EDF with an inner cladding diameter of 85 µm, the required pump power is reduced to 13 W.

5.4.2 Side-pumping

Side-pumping injects the pump light into the inner cladding using either embedded mirrors [172], V-grooves [152], a downsized capillaries [173] or down-tapered fibers [153]. Figure 5.4 illustrates the side-pump coupling combiner using a down-tapered coreless fiber wrapped on a DC-MC-EDF [121].

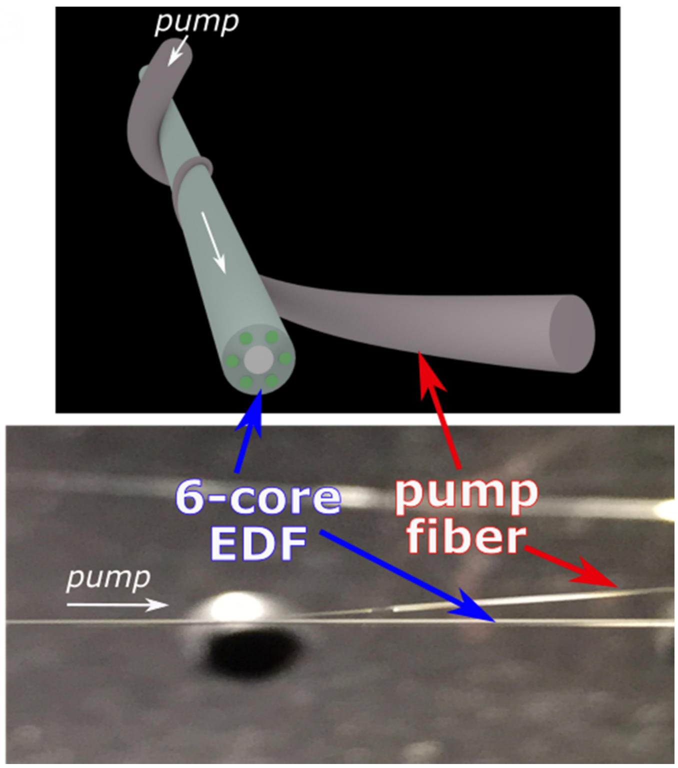

Figure 5.4. Schematic and image of the side-pump coupling technique using a tapered coreless fiber.

In the experiments, a commercially available high power 980-nm laser diode with a 105/125-µm (core diameter/cladding diameter) MMF pigtail was used as the pump source. It produces an output power up to 25 W and has a wavelength temperature drift <0.3 nm °C^{-1} and a spectral full width at half maximum <3 nm. The MMF has a NA of 0.22 and was spliced to a 125-µm diameter coreless fiber. The coreless fiber was tapered down to a diameter of 15 µm over a length of 20 mm and wrapped 1.5 times around a 50-mm section of uncoated EDF. A tension was applied to bring both fibers in physical contact on the pump side. After the coupling area, an air gap between the pump delivery fiber and the EDF prevents the pump light from coupling out of the EDF. Along the taper, the light is adiabatically transferred from the tapered fiber into the amplifying fiber. An efficiency around 65 % was achieved, which could be improved to 90 % [153] by optimizing fabrication parameters.

5.4.3 Fiber preparation and fabrication

Silica optical fiber preforms are usually fabricated by vapor-phase techniques that can be broadly classified into two categories, namely inside and outside deposition. The former includes MCVD [174] and plasma chemical vapor deposition (PCVD) [175], while the later encompasses vapor axial deposition (VAD) [176] and outside vapor deposition (OVD) [177]. Rare-earth element doping in the preform can be achieved either in vapor-phase or in liquid-phase. Among the liquid-phase techniques, solution doping [178] is a convenient process.

In this letter, we used a standard MCVD process for silica glass deposition of the fiber waveguide structure and solution doping for loading erbium ions into the fibre core with a typical concentration of 2.8×10^{25} ions/m^3. The multicore EDF was subsequently fabricated from the single-core preform by a stack-and-draw method, which is widely employed for microstructure [179] or photonic crystal fiber fabrication [180]. The preform deposition, stack assembly and fiber drawing were all done at the COPL of Université Laval. Additional details on the process steps are given below.

Initially, silicon chloride ($SiCl_4$) gas incorporated in a mixture of oxygen and helium is blown through a pure silica substrate tube and heated by an oxy-hydrogen flame. Oxidation, as written in Equation (5.1), under this high temperature condition leads to silicon dioxide deposition on the internal surface of the support tube resulting in the so-called soot boule.

$$SiCl_4 + O_2 = SiO_2 + 2Cl_2 \tag{5.1}$$

Note that the torch temperature to obtain soot boule should be less than about 1500 °C to avoid verification, i.e. sintered glass deposition inside the silica tube that typically occurs under higher temperatures of about 1800~2000 °C. The silica soot, that finally covers all the inside surface of the pure silica tube substrate, has a porous structure with pore diameters that can be varied from nm to μm scale [181]. Although we have not measured the porosity of the soot, it is sufficiently repeatable to meet the need of our multicore design. By carefully adjusting the input flow rate of the gas mixture and the substrate tube temperature, one can control the density of the soot structure to achieve the designed distribution profile of erbium ions.

Next, the tube with the deposited silica soot was immersed into a deionized water based solution that comprises both erbium chloride [$ErCl_3$-6(H_2O), in which erbium exists in the form of ions] and aluminum chloride [$AlCl_3$-6(H_2O)] crystalline hydrate. Erbium ion loading was thus performed by capillary action [182]. We prepared the solution to achieve desired erbium ion doping concentration in the fiber, which depends on both the density of silica soot and the erbium ion concentration of the solution [178]. Afterwards, the tubes with the doped soot boules were dried with nitrogen to remove the aqueous solution.

After doping, the tube with the soot boule was put back on the lathe to complete the process. It was firstly dehydrated by oxy-hydrogen torch heating at low temperature. An oxidation reaction, as expressed in Equations (5.2) and (5.3), also occurs during this step and, consequently, all the dopants were transformed within the soot boule in the form of oxides. Secondly, vitrification of the soot structure was carried out under torch temperature about 2000 °C. Thirdly, extra torch heating collapses the doped tube into a solid glass preform rod with a diameter of around 15 mm.

$$4ErCl_3 + 3O_2 = 2Er_2O_3 + 6Cl_2 \tag{5.2}$$

$$4AlCl_3 + 3O_2 = 2Al_2O_3 + 6Cl_2 \tag{5.3}$$

Since the doped multicore fiber has six cores, in order to achieve sufficient fiber length, we made three identical doped silica preforms using the process described above. Figure 5.5 shows the refractive index profile (refractive index) for all the three preforms (measured by Photon Kinetics PK2600). The preforms were subsequently cut in half so that each preform was used for two of the cores.

To make the stack assembly, the outside diameter of the preforms must be reduced. The three fabricated doped single core preforms were therefore etched, via soaking into HF acid solution, to a diameter of about 2.9 mm. During the HF etching, the core dimension is not modified. The stack assembly also requires a low index fluorine doped silica rod to make the inner cladding. This rod was similarly fabricated by the MCVD deposition, vitrification and collapse process described above by mixing fluorine with the silicon chloride gas. This rod is coreless and undoped with erbium. The lower index fluorine rod was placed at the center of a pure silica holding tube with external and internal diameter of 18 mm and 16 mm, respectively. Then, six doped core rods were stacked around and apart from the fluorine-doped silica rod in a hexagonal packing configuration. Additionally, we used pure silica rods to fill the empty space and to fix the core-spacing and core-to-cladding distances. These silica rods make the annular-cladding that guides the pump. The bundle was hold in place by welding a 20-mm long and 15-mm wide silica rod on the bottom of the stacked preform. Figure 5.6 illustrates the image of stacked preform transverse cross-section. Finally, the stacked preform was drawn to 177-μm fiber diameter and coated with a lower index polymer to make the final double-clad multi-core doped fiber. During drawing, the fiber is further over coated with a higher index polymer to maintain the fiber mechanical properties.

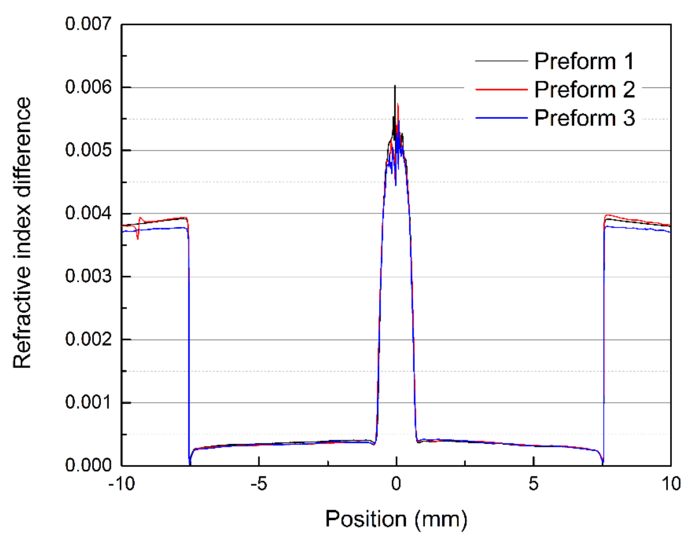

Figure 5.5. Refractive index difference profile of the three doped core single preforms.

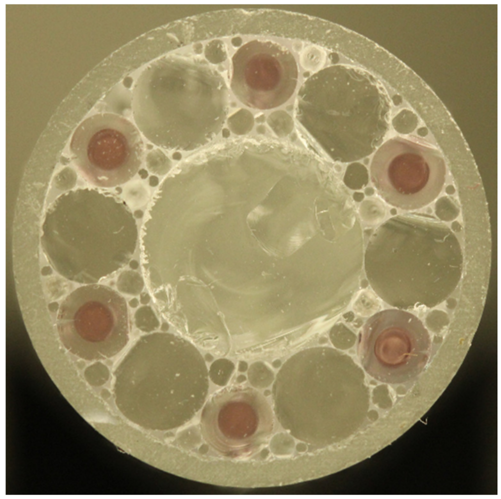

Figure 5.6. Stacked preform (assembly) transverse cross-section image. In the figure, the six rods with 'red' centers are the doped cores. The largest rod at center is fluorine-doped silica inner cladding and the rest of the area is filled with pure silica rods of different sizes.

5.4.4 Fiber parameters

Each core has a NA of 0.104 and a diameter of 16.5 μm. The core-to-core pitch is 62 μm. The low-index inner cladding at the center is made of fluorine-doped silica that creates a refractive index step of 6×10^{-3} compared to the index of the annular-cladding populated by the six cores. The whole cladding diameter is 170 μm, while the inner cladding diameter is 85 μm. The edges of the cores are placed 10 μm from the annular-cladding inner boundary and 16 μm from the outer boundary, respectively. A low-index polymer coating with a NA of 0.4 acts as a double cladding to confine the cladding modes in the annular glass cladding. The NA between the annular-cladding and inner central cladding is 0.11.

The mode profiles of the three spatial modes guided by one of the six cores are shown in Figure 5.7 using a mode-selective photonic lantern at 1300 nm to individually excite each mode. Erbium ions have negligible absorption at 1300 nm, which makes it possible to observe sharp images of excited modes.

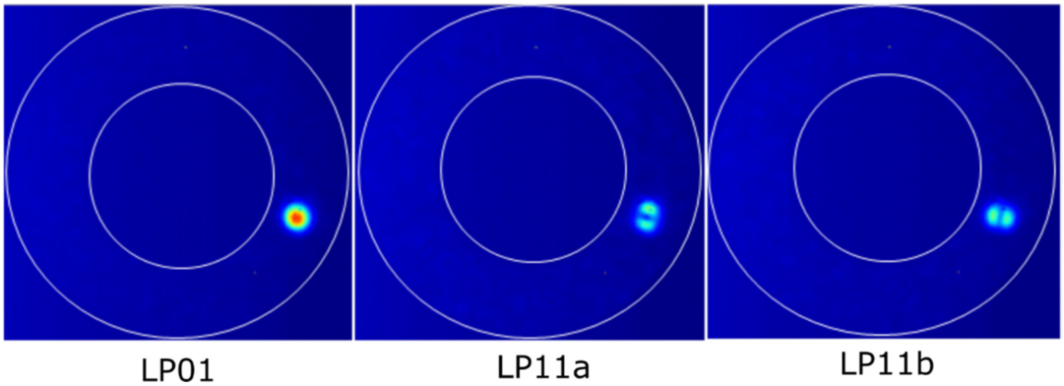

Figure 5.7. Three individually excited spatial modes at 1300 nm.

5.4.5 Ray-tracing simulation

We used ray-tracing implemented in ZEMAX® to simulate the side-pump coupling efficiency, and the pump confinement for two cladding structures: uniform and annular-cladding. 10^7 rays were launched into the coreless fiber from a source at the input facet with the same NA as the MMF used in the measurements. The detectors were placed at the end of both fibers and the pump power distribution was calculated by counting the number of rays exiting the transverse cross-section.

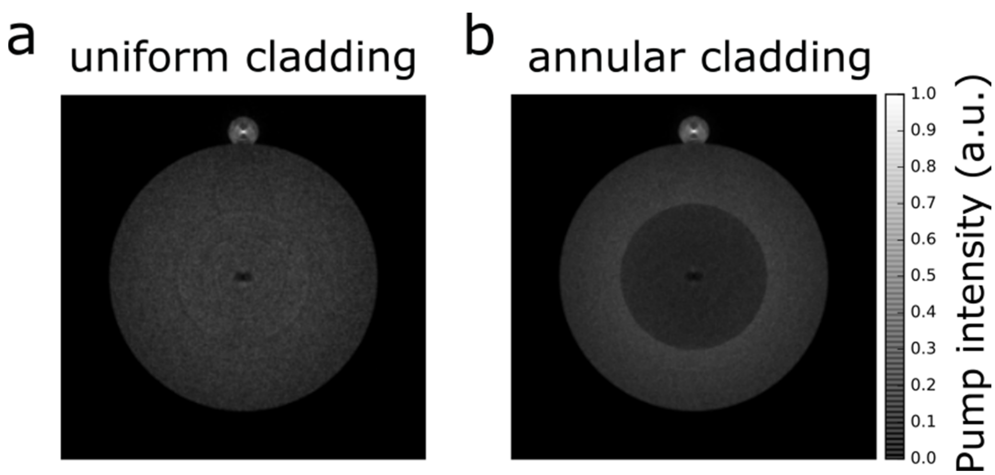

Figure 5.8. Simulated pump power distribution for uniform and annular-cladding by side pumping.

Figure 5.8 shows the simulated pump power distribution for uniform and annular-cladding, respectively, by side-pumping.

5.4.6 Gain and noise figure measurements

The gain and NF performance of each EDF core was characterized in the WDM configuration using eight laser sources covering the C-band as the signal and an OSA to measure the output spectrum. The input signal power was adjusted by a variable optical attenuator. The SMFs at the input and output are placed on two three-axis stages and were butt-coupled onto each core of a 2.1-m long six-core EDF to selectively excite and detect the LP_{01} mode with a mode extinction ratio larger than 30 dB. The input and output sections of the EDF were fixed on two fiber holders. Two isolators at the input and output were used to prevent lasing induced by facet reflection. Switching the input and output SMFs enabled characterization of the EDFA under both forward and backward pumping. With the pump coupling efficiency of 65 %, the maximum coupled-pump power is 15 W. Any residual cladding pump is dumped via a cladding pump light stripper made by degrading the fiber surface through HF etching. Due to the degeneracy of two LP_{11} modes, it is difficult to accurately characterize each LP_{11} mode in terms of NF. The NF of both LP_{11} modes is expected to be similar.

5.4.7 Crosstalk

To investigate core-to-core and pump-depletion-induced cross-talk, the EDF was characterized using fiber fan-in/fan-out and the setup is illustrated in Figure 5.9(a). Figure 5.9(b) shows the schematic and facet image of the fan-in/fan-out based on a tapered fiber bundle that consists of six graded-index cores with a diameter of 15 μm arranged in a ring to match the core structure of the six-core EDF with a core-to-core pitch of 62 μm. The input MMFs of the fan-in/fan-out device support 15 spatial modes and are spliced to other MMFs supporting three spatial modes with coupling losses from the LP_{01} to LP_{01} and LP_{11} to LP_{11} are <0.5 dB. Mode-group selective photonic-lantern-based SMUXs [158][183] with a mode selectivity better than 12 dB excite the three spatial modes with 0.5-dB loss for the LP_{01} and 1.5-dB loss for the LP_{11} modes, respectively.

Figure 5.9(c) shows the amplifier output power per spatial channel of one core under different signal loading conditions in saturation condition.

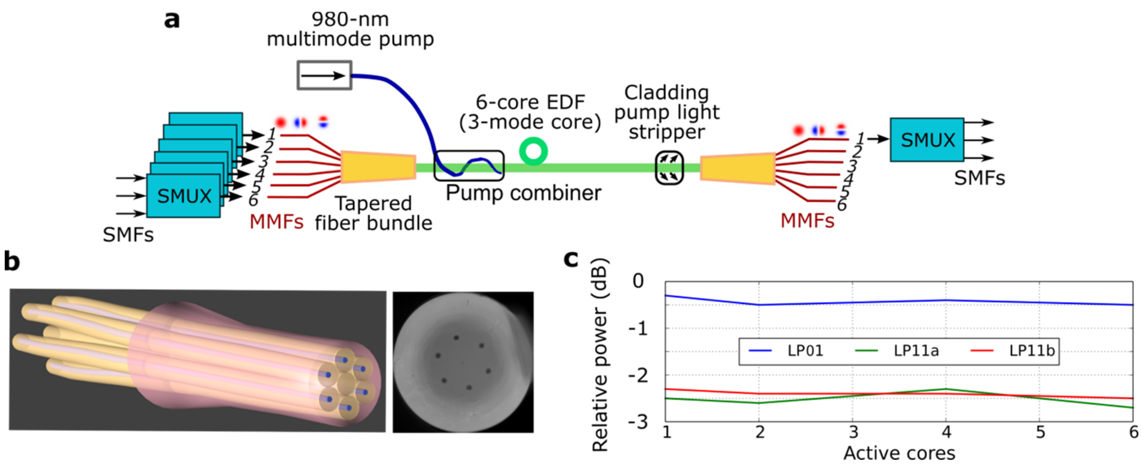

Figure 5.9. Core-to-core cross-talk and pump-depletion-induced cross-talk characterization. (a) Characterization setup for the cladding-pumped six-core EDF with connected fan-in/fan-outs. (b) Schematics and facet image of a tapered-fiber-bundle-based fan-in/fan-out. (c) Output power per mode under different signal loading conditions.

5.4.8 Data processing

Off-line DSP was applied to recover the signals and the preprocessing steps include: 2 × resampling, front-end skew corrections, chromatic dispersion and frequency offset correction. A 6 × 6 (6 = three spatial modes × two polarizations) frequency-domain equalizer with 800 symbol-spaced taps based on a data-aided LMS algorithm was applied to converge the equalizer and determine the channel impulse response. For BER counting, we used the CMA to slowly adapt the equalizer followed by carrier-phase recovery.

5.4.9 Equivalent noise figure

In order to evaluate the performance for the cascaded amplification case, system $NF_{sys}(dB) = SNR_{in}(dB) - SNR_{out}(dB)$ and effective NF, $NF_{eff}(dB) = NF_{sys}(dB) - 10\times\log_{10}(m) - \alpha(dB)$ were used, where $SNR_{in}(dB)$ is the input SNR in dB, $SNR_{out}(dB)$ is the output SNR in dB, m is the number of amplifiers in a chain and $\alpha(dB)$ is the fiber span loss.

5.4.10 Mode-dependent loss

MDL can be varied across the frequency. A frequency-averaged MDL was applied and calculated based on the converged equalizer acquired in the DSP. The equalizer can be represented in frequency domain by a matrix H_f with a size of $N_m \times N_m \times L_b$, where N_m is the number of space-polarization modes and L_b is the equalizer length in number of taps ($N_m = 6$ *and* $L_b = 1024$ in our case). The last dimension of H_f corresponds to different frequencies. Therefore, at each frequency, the equalizer is a 2-dimensional $N_m \times N_m$ matrix written as H_{fi}, where i is from 1 to L_b. N_m singular values for each frequency were calculated by applying singular value decomposition to each H_{fi}. The frequency-averaged MDL was calculated based on the square of N_m averaged singular values over the frequency S_j, where j is from 1 to N_m through application of $\mathrm{MDL} = 10\times\log_{10}(\max(S_j^2)/\min(S_j^2))$. Figure 5.10 gives the intensity-impulse response after 120-km transmission averaged over all 6 × 6 spatial channels and shows multiple peaks from coupling between LP_{01} and LP_{11} modes at the six splice points. Figure 5.11 provides the BER for each spatial and polarization mode versus wavelength. There are four spatial and polarization modes in the LP_{11} mode group and two in the LP_{01} mode group. Lower BERs were achieved for the LP_{01} modes since they are less sensitive to the errors at each splicing point compared to the LP_{11} modes.

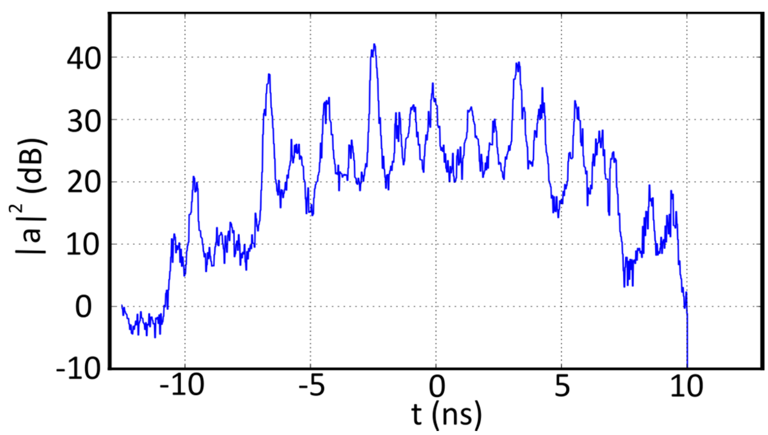

Figure 5.10. Intensity-impulse response.

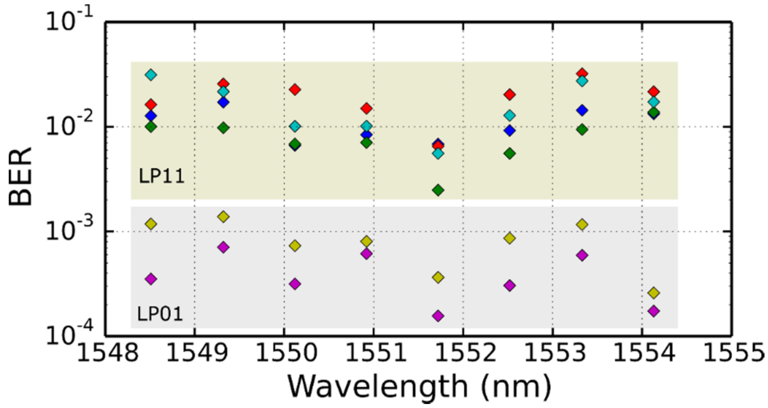

Figure 5.11. BER for each spatial and polarization mode versus wavelength.

Chapter 6

Conclusions and Perspective

6.1 Conclusions

In this thesis, we first briefly reviewed the development of optical fiber communications systems that nowadays provide the high bandwidth services, from video streaming to cloud computing, at the heart of today's society. State-of-the-art optical fiber transmission systems are the results of a relentless succession of profound technological transformations that have consisted of the introduction of WDM, PDM as well as advanced modulation techniques. We have discussed how a new paradigm shift is now needed to overcome the transmission capacity limit set by information theory and the seemingly unavoidable nonlinear impairments. The current emerging solution is to exploit space as a new degree of freedom for multiplexing data channels. Researchers worldwide are exploring SDM with the hope that it will overcome the so-called '*capacity crunch*' in the forthcoming decade.

Two SDM paths are presently being pursued: MCF and FMF transmission. Both approaches allow multi-spatial channels integration within a single optical fiber strand. Recent progress in both scenarios was reviewed and some reports revealed that the SDM can achieve hundreds of times capacity extension compared to the conventional SMF transmission link. Although encouraging results and even milestone heroic experiments have been demonstrated, several key technical issues still need to be investigated, such as DMGD in the MDM transmission system and cross-talk in the MCF based SDM transmission system.

In order to implement SDM transmission systems, novel spatially integrated elements such as spatial multiplexers, attenuator, isolator, etc. as well as subsystems like optical amplifiers, WSS, etc. have to be investigated and developed. The optical amplifier is critical for optical fiber transmission links, particularly for the long-haul transmission case. After reviewing the current proposal for EDF based SDM optical amplifiers, including MC-EDFA, FM-EDFA, and MC-FM-EDFA, we decided to investigate in this thesis novel EDF designs that would improve the performance of SDM optical amplifiers. Our work in FMF amplifiers was focused on providing means to dynamically equalize the mode dependant gain. For MCF amplifiers, we focused on improving the pump power efficiency. Moreover, the proposed fibers have been fabricated, characterized and MCF amplifiers were demonstrated in a full SDM transmission system.

Chapter 2 described the basic theory of the rare-earth doped fiber amplifiers, in particular, the EDFA. In the EDFA operation mechanism, the energy levels and cross-sections represent key points in order to understand the amplifier working principle. After that, we expressed the numerical modeling of conventional EDFA including power propagation and population rate equations. When applying the numerical model to describe an EDFA for SDM, one has to modify the set of equations, in particular, the overlap integral terms. Considering the strong mode spatial distribution dependence, we proposed a multi-block model in order to resolve the fiber transverse cross-section.

By implementing that decomposition, the integrals which describe the interaction between the propagating channels and erbium ions in the power propagation evolution and atomic rate equations can be simplified to a summations. This model is used in Chapter 3 to propose a MM-EDFA design offering a simple approach to precisely control the MDG. The amplification of the co-propagating LP_{01} and LP_{11} modes of the MM-EDFA interact with different portions of the erbium doping profile, i.e. the LP_{01} mode gain benefits from the central doped rod while the outer doped ring preferably contributes to the LP_{11} mode. Combining this engineered doping profile with a pump injected into the fundamental pump mode, one can adjust the MDG through tuning the pump power. We optimized the doping profile design parameters such as the width and doping level of each ring through numerical simulations. Subsequently, we evaluated the gain as well as the NF of single stage MM-EDFA based on either an outer ring plus center rod or a double-ring doping profile. Simulation results showed that the proposed designs can achieve not only ZDMG but also adjustable DMG. We further discussed the possibility to change the DMG via tuning of bi-directional pump powers in a dual-stage MM-EDFA configuration employing two doping profiles for each stage.

In Chapter 4, we design a novel MC-EDF that has an annular silica cladding, populated by six doped signal cores, to guide the pump light. With either solid index-depressed or air-hole central inner cladding, the pump modes are well confined inside a ring-shaped region, i.e. so-called annular-cladding. This tailored fiber structure enhances the pump power utilization in the cladding pumped EDFAs for SDM transmission system, in particular for the long-haul links. We numerically investigated the optimized signal core and annular pump cladding parameters respecting our fiber fabrication constraints. In addition, the multi-spot edge injection scheme to feed the multimode pump light into the annular-cladding was proposed and examined. Compared to the all-glass conventional double-cladding EDFA, the simulation results predicted 10-dB increase in gain and 21 % pump power savings with the help of the annular-cladding. The pump power can be prevented from leaking into the inner cladding by replacing the depressed-index solid inner cladding with an air-hole, and the pump power confinement was further enhanced.

Based on the simulation work discussed above, we successfully fabricated and characterized a six-core three-mode EDF which has annular pump cladding associating with index depressed inner cladding. In Chapter 5, we demonstrated the spatially integrated EDFA based on that fiber, which can amplify 18 spatial channels simultaneously. Thanks to the annular pump cladding design and side pumping by a 25-W multimode laser diode, the six-core three-mode amplifier generates more than 20-dBm total output power per each of the three-mode core over the C-band. Meanwhile, NF less than 7-dB was achieved for all the cores over the C-band. Following the doped fiber characterization, we conducted a transmission experiment in order to validate the amplifier performance in the SDM system. The propagation loss of three transmission spans consist of 120-km MMF in total and are compensated by three cores of the amplifier while another three cores were fully loaded with counter-propagating dummy channels. Experimental results indicated that the amplifier provided sufficient gain as well as low NF to enable the long reach of the SDM transmission system. Moreover, some details about the fiber fabrication, characterization and experiment were discussed in the corresponding context.

The original work presented in this thesis was the object of several journal and conference papers. Chapter 3, entitled “Tailored modal gain in a multi-mode erbium-doped fiber amplifier based on engineered ring doping profiles” was presented at the Photonics North 2013 conference and published in a SPIE proceeding. Chapter 4, entitled “Annular-cladding erbium-doped multicore fiber for SDM amplification," is based on a paper published in Optics Express, an OSA journal with high impact factor. Chapter 5 entitled "Spatially Integrated Optical Fiber Amplifier," is based on a paper submitted to Nature Photonics following the invitation respecting to the *ECOC* 2015 post-deadline paper [90] by the editor.

6.2 Perspectives

Although we demonstrated the MC-FM-EDFA, some technical issues such as cross-talk, MDL, pump coupling etc. still needed to be paid attention to and investigated.

A key component in SDM is the spatial channel multiplexer. Since the doped fiber used in an amplifier has only few or dozen meters, the main source of cross-talk is believed to be introduced by the multiplexer. Currently, the TFB and photonic lantern are the most attractive candidates as multiplexers for the MCF and MMF based SDM system, but novel multiplexers that provide better performance can be investigated to reduce cross-talk and MDL. The solution will most likely be required to be fiber-based device due to provide low insertion loss and splice feasibbility.

Further design of EDF for the spatially integrated fiber amplifier should focus on enhancing the power utilization efficiency, increasing output power, supporting spatial channel scalability, and extending to new transmission windows such as L-band. Possibilities could include a modified fiber structure design incorporating a depressed-index trench to help pump mode confinement around signal core area as well as providing an opportunity to integrate more fiber cores. Moreover, future fiber designs have to pay attention to the passive transmission fiber structures. In other words, the doped fiber parameters must be suitably matched to those of the passive fiber to ensure good performance.

On the other hand, the SI-EDFA is not restricted for use in SDM transmission systems. On the contrary, it can be implemented in state-of-the-art single-core SMF based transmission systems. Considering the fiber scale integration, this amplifier could replace multiple individual amplifiers and thereafter the system power budget and implementation costs are expected to be reduced. In order to realize that, novel elements that provide spatial integration must be studied.

Aside from inline optical amplification, such erbium-doped multicore, multimode or multicore multimode fibers can also be used to devise novel fiber lasers. As an example, the MCF laser is an attractive idea since it can integrate several lasers within one fiber and share a common pump source which may be more efficient overall. Such multicore laser can have either identical wavelengths or differents wavelength depending on the application scenario.

In general, the spatially integrated optical fiber amplifier based on erbium-doped MCF, MMF or MC-FMF has the benefits of power consumption efficiency and reduced system cost through better integration. That amplifier efficiently drives not only the SDM system but also state-of-the-art transmission systems to help build next generation green optical fiber networks.

References

[1] K. C. Kao and G. a. Hockham, “Dielectric-fibre surface waveguides for optical frequencies,” *Proc. Inst. Electr. Eng.*, vol. 113, no. 7, p. 1151, 1966.

[2] F. P. Kapron, “Radiation Losses in Glass Optical Waveguides,” *Appl. Phys. Lett.*, vol. 17, no. 10, p. 423, 1970.

[3] E. Desurvire, J. R. Simpson, and P. C. Becker, “High-gain erbium-doped traveling-wave fiber amplifier,” *Opt. Lett.*, vol. 12, no. 11, pp. 888–890, 1987.

[4] D. J. Richardson, J. M. Fini, and L. E. Nelson, “Space-division multiplexing in optical fibres,” *Nat. Photonics*, vol. 7, pp. 354–362, 2013.

[5] R. J. Essiambre and R. W. Tkach, “Capacity trends and limits of optical communication networks,” *Proc. IEEE*, vol. 100, no. 5, pp. 1035–1055, 2012.

[6] P. J. Winzer, “Modulation and multiplexing in optical communication systems,” *LEOS Newsletter*, no. February, pp. 4–9, 2009.

[7] C. E. Shannon, “A mathematical theory of communication,” *Bell Syst. Tech. J.*, vol. 27, pp. 379–423, 623–656, 1948.

[8] P. P. Mitra and J. B. Stark, “Nonlinear limits to the information capacity of optical fibre communications,” *Nature*, vol. 411, no. 6841, pp. 1027–30, Jun. 2001.

[9] E. B. Desurvire, “Capacity Demand and Technology Challenges for Lightwave Systems in the Next Two Decades,” *J. Light. Technol.*, vol. 24, no. 12, pp. 4697–4710, Dec. 2006.

[10] R. Essiambre and G. Foschini, “Capacity limits capacity limits of fiber fiber-optic communication systems,” in *Optical Fiber Communication Conference/National Fiber Optic Engineers Conference*, 2009, p. OThL1.

[11] A. Chralyvy, “The coming capacity crunch,” in *European Conference and Exhibition on Optical Communication*, 2009, p. Plenary paper.

[12] A. Tarighat, R. C. J. Hsu, A. Shah, A. H. Sayed, and B. Jalali, “Fundamentals and challenges of optical multiple-input multiple-output multimode fiber links,” *IEEE Commun. Mag.*, vol. 45, no. 5, pp. 57–63, May 2007.

[13] T. Morioka, “New Generation Optical Infrastructure Technologies : ‘ EXAT Initiative ’ Towards 2020 and Beyond,” in *OptoElectronics and Communications Conference*, 2009, pp. 9–10.

[14] H. Stuart, "Dispersive multiplexing in multimode optical fiber," *Science (80-.).*, vol. 289, no. 5477, pp. 281–283, Jul. 2000.

[15] T. Hayashi, T. Taru, and O. Shimakawa, "Ultra-low-crosstalk multi-core fiber feasible to ultra-long-haul transmission," in *Optical Fiber Communication Conference/National Fiber Optic Engineers Conference*, 2011, p. PDPC2.

[16] P. Sillard, M. Bigot-astruc, D. Boivin, H. Maerten, and L. Provost, "Few-Mode Fiber for Uncoupled Mode-Division Multiplexing Transmissions," in *European Conference and Exhibition on Optical Communication*, 2011, p. Tu.5.LeCervin.7.

[17] Cen Xia, R. Amezcua-Correa, Neng Bai, E. Antonio-Lopez, D. M. Arrioja, A. Schulzgen, M. Richardson, J. Liñares, C. Montero, E. Mateo, Xiang Zhou, and Guifang Li, "Hole-Assisted Few-Mode Multicore Fiber for High-Density Space-Division Multiplexing," *IEEE Photonics Technol. Lett.*, vol. 24, no. 21, pp. 1914–1917, Nov. 2012.

[18] R. Ryf, "SDM components and MIMO experiments in multimode and multicore fibers," in *European Conference and Exhibition on Optical Communication*, 2014, p. Th.2.1.1.

[19] R. Ryf, S. Randel, A. H. Gnauck, C. Bolle, R.-J. Essiambre, P. Winzer, D. W. Peckham, A. McCurdy, and R. Lingle, "Space-division multiplexing over 10 km of three-mode fiber using coherent 6×6 MIMO processing," in *Optical Fiber Communication Conference/National Fiber Optic Engineers Conference*, 2011, p. PDPB10.

[20] J. Sakaguchi, Y. Awaji, N. Wada, A. Kanno, T. Kawanishi, T. Hayashi, T. Taru, T. Kobayashi, and M. Watanabe, "109-Tb/s (7×97×172-Gb/s SDM/WDM/PDM) QPSK transmission through 16.8-km homogeneous multi-core fiber," in *Optical Fiber Communication Conference/National Fiber Optic Engineers Conference*, 2011, p. PDPB6.

[21] B. Zhu, X. Liu, S. Chandrasekhar, T. Taunay, M. Fishteyn, M. Yan, J. M. Fini, E. Monberg, and F. Dimarcello, "112-Tb/s (7×160×107Gb/s) Space-Division Multiplexed DWDM Transmission over a 76.8-km Multicore Fiber," in *European Conference and Exhibition on Optical Communication*, 2011, p. Tu.5.B.5.

[22] B. J. Puttnam, R. S. Luis, W. Klaus, J. Sakaguchi, J.-M. Delgado Mendinueta, Y. Awaji, N. Wada, Y. Tamura, T. Hayashi, M. Hirano, and J. Marciante, "2.15 Pb/s transmission using a 22 core homogeneous single-mode multi-core fiber and wideband optical comb," in *European Conference and Exhibition on Optical Communication*, 2015, p. PDP.3.1.

[23] S. Chandrasekhar, A. Gnauck, X. Liu, P. Winzer, Y. Pan, E. C. Burrows, B. Zhu, T. Taunay, M. Fishteyn, M. Yan, J. M. Fini, E. Monberg, and F. Dimarcello,

"WDM/SDM Transmission of 10×128-Gb/s PDM-QPSK over 2688-km 7-Core Fiber with a per-Fiber Net Aggregate Spectral-Efficiency Distance Product of 40,320 km.b/s/Hz," in *European Conference and Exhibition on Optical Communication*, 2011, p. Th.13.C.4.

[24] R. Ryf, R. Essiambre, A. Gnauck, S. Randel, M. A. Mestre, C. Schmidt, P. Winzer, R. Delbue, P. Pupalaikis, A. Sureka, T. Hayashi, T. Taru, and T. Sasaki, "Space-Division Multiplexed Transmission over 4200 km 3-Core Microstructured Fiber," in *Optical Fiber Communication Conference/National Fiber Optic Engineers Conference*, 2012, p. PDP5C.2.

[25] H. Takahashi, T. Tsuritani, E. Le Taillandier de Gabory, T. Ito, W.-R. Peng, K. Igarashi, K. Takeshima, Y. Kawaguchi, I. Morita, Y. Tsuchida, Y. Mimura, K. Maeda, T. Saito, K. Watanabe, K. Imamura, R. Sugizaki, and M. Suzuki, "First Demonstration of MC-EDFA-Repeatered SDM Transmission of 40×128-Gbit/s PDM-QPSK Signals per Core over 6,160-km 7-core MCF," in *European Conference and Exhibition on Optical Communication*, 2012, p. Th.3.C.3.

[26] B. Zhu, T. Taunay, M. Fishteyn, X. Liu, S. Chandrasekhar, M. Yan, J. Fini, E. Monberg, and F. Dimarcello, "Space-, Wavelength-, Polarization-Division Multiplexed Transmission of 56-Tb/s over a 76.8-km Seven-Core Fiber," in *Optical Fiber Communication Conference/National Fiber Optic Engineers Conference*, 2011, p. PDPB7.

[27] X. Liu, S. Chandrasekhar, X. Chen, P. Winzer, Y. Pan, B. Zhu, T. Taunay, M. Fishteyn, M. Yan, J. M. Fini, E. Monberg, and F. Dimarcello, "1.12-Tb/s 32-QAM-OFDM Superchannel with 8.6-b/s/Hz Intrachannel Spectral Efficiency and Space-Division Multiplexing with 60-b/s/Hz Aggregate Spectral Efficiency," in *European Conference and Exposition on Optical Communication*, 2011, p. Th.13.B.1.

[28] R. Ryf, R. J. Essiambre, S. Randel, a. H. Gnauck, P. J. Winzer, T. Hayashi, T. Taru, and T. Sasaki, "MIMO-based crosstalk suppression in spatially multiplexed 3×56-Gb/s PDM-QPSK signals for strongly coupled three-core fiber," *IEEE Photonics Technol. Lett.*, vol. 23, no. 20, pp. 1469–1471, 2011.

[29] S. Randel, M. Magarini, R. Ryf, A. Gnauck, P. Winzer, T. Hayashi, T. Taru, T. Sasaki, and others, "MIMO-based Signal Processing of Spatially Multiplexed 112-Gb/s PDM-QPSK Signals using Strongly-Coupled 3-Core Fiber," in *European Conference and Exposition on Optical Communication*, 2011, p. Tu.5.B.1.

[30] R. Ryf, A. Sierra, R.-J. Essiambre, A. Gnauck, S. Randel, M. Esmaeelpour, S. Mumtaz, P. J. Winzer, R. Delbue, P. Pupalaikis, A. Sureka, T. Hayashi, T. Taru, and T. Sasaki, "Coherent 1200-km 6×6 MIMO Mode-Multiplexed Transmission over 3-Core Microstructured Fiber," in *European Conference and Exposition on Optical Communication*, 2011, p. Th.13.C.1.

[31] J. Sakaguchi, B. J. Puttnam, W. Klaus, Y. Awaji, N. Wada, A. Kanno, T. Kawanishi, K. Imamura, H. Inaba, K. Mukasa, R. Sugizaki, T. Kobayashi, and M. Watanabe, "19-core fiber transmission of 19×100×172-Gb/s SDM-WDM-PDM-QPSK signals at 305Tb/s," in *Optical Fiber Communication Conference*, 2012, p. PDP5C.1.

[32] A. H. Gnauck, S. Chandrasekhar, X. Liu, S. Randel, S. Corteselli, T. Taunay, B. Zhu, and M. Fishteyn, "WDM Transmission of 603-Gb/s Superchannels over 845 km of 7-Core Fiber with 42.2 b/s/Hz Spectral Efficiency," in *European Conference and Exhibition on Optical Communication*, 2012, p. Th.2.C.2.

[33] X. Liu, S. Chandrasekhar, A. H. Gnauck, P. Winzer, S. Randel, S. Corteselli, B. Zhu, T. Taunay, and M. Fishteyn, "Digital Coherent Superposition for Performance Improvement of Spatially Multiplexed 676-Gb/s OFDM-16QAM Superchannels," in *European Conference and Exhibition on Optical Communication*, 2012, p. Tu.3.C.2.

[34] H. Takara, A. Sano, T. Kobayashi, H. Kubota, H. Kawakami, A. Matsuura, Y. Miyamoto, Y. Abe, H. Ono, K. Shikama, Y. Goto, K. Tsujikawa, Y. Sasaki, I. Ishida, K. Takenaga, S. Matsuo, K. Saitoh, M. Koshiba, and T. Morioka, "1.01-Pb/s (12 SDM/222 WDM/456 Gb/s) Crosstalk-managed Transmission with 91.4-b/s/Hz Aggregate Spectral Efficiency," in *European Conference and Exhibition on Optical Communication*, 2012, p. Th.3.C.1.

[35] M. Tadakuma, K. Watanabe, T. Saito, T. Tsuritani, K. Maeda, K. Igarashi, M. Suzuki, Y. Tsuchida, R. Sugizaki, I. Morita, and K. Imamura, "1.03-Exabit/s.km Super-Nyquist-WDM Transmission over 7,326-km Seven-Core Fiber," in *European Conference and Exhibition on Optical Communication*, 2013, p. PD3.E.3.

[36] K. Hiraga, M. Yamada, H. Kawakami, S. Matsuo, H. Masuda, H. Takara, A. Sano, K. Saitoh, T. Kobayashi, K. Takenaga, I. Ishida, Y. Abe, H. Ono, M. Wada, T. Morioka, Y. Sasaki, T. Mizuno, and Y. Miyamoto, "2×344 Tb/s propagation-direction interleaved transmission over 1500-km MCF enhanced by multicarrier full electric-field digital back-propagation," in *European Conference and Exhibition on Optical Communication*, 2013, p. PD3.E.4.

[37] R. Ryf, N. K. Fontaine, B. Guan, R.-J. Essiambre, S. Randel, A. H. Gnauck, S. Chandrasekhar, A. Adamiecki, G. Raybon, B. Ercan, R. P. Scott, S. J. Ben Yoo, T. Hayashi, T. Nagashima, and T. Sasaki, "1705-km transmission over coupled-core fibre supporting 6 spatial modes," in *European Conference and Exhibition on Optical Communication*, 2014, p. PD.3.2.

[38] H. Takara, T. Mizuno, H. Kawakami, Y. Miyamoto, H. Masuda, K. Kitamura, H. Ono, S. Asakawa, Y. Amma, K. Hirakawa, S. Matsuo, K. Tsujikawa, and M. Yamada, "120.7-Tb/s (7 SDM/180 WDM/95.8 Gb/s) MCF-ROPA unrepeatered transmission of PDM-32QAM channels over 204 km," in *European Conference and Exhibition on Optical Communication*, 2014, p. PD.3.1.

[39] M. Salsi, C. Koebele, D. Sperti, P. Tran, P. Brindel, H. Mardoyan, S. Bigo, A. Boutin, F. Verluise, P. Sillard, M. Bigot-Astruc, L. Provost, F. Cerou, and G. Charlet, “Transmission at 2×100Gb/s, over Two Modes of 40km-long Prototype Few-Mode Fiber, using LCOS based Mode Multiplexer and Demultiplexer,” in *Optical Fiber Communication Conference/National Fiber Optic Engineers Conference*, 2011, p. PDPB9.

[40] S. Randel, R. Ryf, A. Sierra, P. J. Winzer, A. H. Gnauck, C. A. Bolle, R.-J. Essiambre, D. W. Peckham, A. McCurdy, and R. Lingle, “6×56-Gb/s mode-division multiplexed transmission over 33-km few-mode fiber enabled by 6×6 MIMO equalization,” *Opt. Express*, vol. 19, no. 17, pp. 16697–16707, Aug. 2011.

[41] C. Koebele, M. Salsi, L. Milord, R. Ryf, C. A. Bolle, P. Sillard, S. Bigo, and G. Charlet, “40km Transmission of Five Mode Division Multiplexed Data Streams at 100Gb/s with low MIMO-DSP Complexity,” in *European Conference and Exposition on Optical Communication*, 2011, p. Th.13.C.3.

[42] E. Ip, N. Bai, Y. Huang, E. Mateo, F. Yaman, S. Bickham, H.-Y. Tam, C. Lu, M. Li, S. Ten, A. P. T. Lau, V. Tse, G.-D. Peng, C. Montero, X. Prieto, and G. Li, “88×3×112-Gb/s WDM Transmission over 50-km of Three-Mode Fiber with Inline Multimode Fiber Amplifier,” in *European Conference and Exposition on Optical Communication*, 2011, p. Th.13.C.2.

[43] A. Li, A. Al Amin, X. Chen, and W. Shieh, “Reception of Mode and Polarization Multiplexed 107-Gb/s CO-OFDM Signal over a Two-Mode Fiber,” in *Optical Fiber Communication Conference/National Fiber Optic Engineers Conference*, 2011, p. PDPB8.

[44] R. Ryf, S. Randel, A. H. Gnauck, C. Bolle, A. Sierra, S. Mumtaz, M. Esmaeelpour, E. C. Burrows, R. J. Essiambre, P. J. Winzer, D. W. Peckham, A. H. McCurdy, and R. Lingle, “Mode-division multiplexing over 96 km of few-mode fiber using coherent 6×6 MIMO processing,” *J. Light. Technol.*, vol. 30, no. 4, pp. 521–531, Feb. 2012.

[45] E. Ip, N. Bai, Y.-K. Huang, E. Mateo, F. Yaman, M.-J. Li, S. Bickham, S. Ten, Y. Luo, G.-D. Peng, G. Li, T. Wang, J. Linares, C. Montero, and V. Moreno, “6×6 MIMO Transmission over 50+25+10 km Heterogeneous Spans of Few-Mode Fiber with Inline Erbium-Doped Fiber Amplifier,” in *Optical Fiber Communication Conference/National Fiber Optic Engineers Conference*, 2012, p. OTu2C.4.

[46] V. Sleiffer, Y. Jung, V. Veljanovski, R. van Uden, M. Kuschnerov, Q. Kang, L. Grüner-Nielsen, Y. Sun, D. Richardson, S. Alam, F. Poletti, J. Sahu, A. Dhar, H. Chen, B. Inan, T. Koonen, B. Corbett, R. Winfield, A. Ellis, and H. De Waardt, “73.7 Tb/s (96×3×256-Gb/s) mode-division-multiplexed DP-16QAM transmission with inline MM-EDFA,” in *European Conference and Exhibition on Optical Communication*, 2012, p. Th.3.C.4.

[47] R. Ryf, M. a. Mestre, S. Randel, X. Palou, A. H. Gnauck, R. Delbue, P. Pupalaikis, A. Sureka, Y. Sun, X. Jiang, and R. Lingle, "Combined SDM and WDM transmission over 700-km Few-Mode Fiber," in *Optical Fiber Communication Conference/National Fiber Optic Engineers Conference*, 2013, p. OW1I.2.

[48] R. Ryf, S. Randel, N. K. Fontaine, M. Montoliu, E. Burrows, S. Chandrasekhar, A. H. Gnauck, C. Xie, R.-J. Essiambre, P. Winzer, R. Delbue, P. Pupalaikis, A. Sureka, Y. Sun, L. Gruner-Nielsen, R. V. Jensen, and R. Lingle, "32-bit/s/Hz Spectral Efficiency WDM Transmission over 177-km Few-Mode Fiber," in *Optical Fiber Communication Conference/National Fiber Optic Engineers Conference*, 2013, p. PDP5A.1.

[49] E. Ip, M. Li, C. Montero, and Y. Yano, "6×28-Gbaud Few-Mode Recirculating Loop Transmission with Gain-Equalized Inline Few-Mode Fiber Amplifier," in *Optical Fiber Communication Conference/National Fiber Optic Engineers Conference*, 2013, p. OW4F.3.

[50] B. Inan, Y. Jung, and V. Sleiffer, "Low Computational Complexity Mode Division Multiplexed OFDM Transmission over 130 km of Few Mode Fiber," in *Optical Fiber Communication Conference/National Fiber Optic Engineers Conference*, 2013, p. OW4F.4.

[51] H. Chen, V. Sleiffer, R. Van Uden, C. Okonkwo, M. Kuschnerov, Y. Sun, H. De Waardt, and T. Koonen, "3 MDM×8 WDM×320-Gb/s DP-32QAM Transmission over a 120km Few-Mode Fiber Span Employing 3-Spot Mode Couplers," in *OptoElectronics and Communications Conference and Photonics in Switching*, 2013, pp. PD3–6.

[52] E. Ip, M. Li, Y.-K. Huang, A. Tanaka, E. Mateo, W. Wood, J. Hu, Y. Yano, and K. Koreshkov, "146λ×6×19-Gbaud Wavelength- and Mode-Division Multiplexed Transmission over 10×50-km Spans of Few-Mode Fiber with a Gain-Equalized Few-Mode EDFA," in *Optical Fiber Communication Conference/National Fiber Optic Engineers Conference*, 2013, p. PDP5A.2.

[53] V. A. J. M. Sleiffer, P. Leoni, Y. Jung, J. Surof, M. Kuschnerov, V. Veljanovski, S. U. Alam, D. J. Richardson, L. Grüner-Nielsen, Y. Sun, B. Corbett, R. Winfield, S. Calabrò, and H. de Waardt, "20×960-Gb/s Space-division-multiplexed 32QAM transmission over 60 km few-mode fiber," *Opt. Express*, vol. 22, no. 1, pp. 749–755, 2014.

[54] N. K. Fontaine, R. Ryf, H. Chen, A. V. Benitez, B. Guan, R. Scott, B. Ercan, S. J. Ben Yoo, L. E. Grüner-Nielsen, Y. Sun, R. Lingle, E. Antonio-Lopez, and R. Amezcua-Correa, "30×30 MIMO Transmission over 15 Spatial Modes," in *Optical Fiber Communication Conference*, 2015, p. Th5C.1.

[55] R. G. H. van Uden, R. A. Correa, E. A. Lopez, F. M. Huijskens, C. Xia, G. Li, A. Schülzgen, H. de Waardt, A. M. J. Koonen, and C. M. Okonkwo, "Ultra-high-density spatial division multiplexing with a few-mode multicore fibre," *Nat. Photonics*, vol. 8, pp. 865–870, Oct. 2014.

[56] T. Mizuno, T. Kobayashi, H. Takara, A. Sano, H. Kawakami, T. Nakagawa, Y. Miyamoto, Y. Abe, T. Goh, M. Oguma, T. Sakamoto, Y. Sasaki, I. Ishida, K. Takenaga, S. Matsuo, K. Saitoh, and T. Morioka, "12-core×3-mode Dense Space Division Multiplexed Transmission over 40 km Employing Multi-carrier Signals with Parallel MIMO Equalization," in *Optical Fiber Communication Conference*, 2014, p. Th5B.2.

[57] J. Sakaguchi, W. Klaus, J. M. Delgado Mendinueta, B. J. Puttnam, R. S. Luis, Y. Awaji, N. Wada, T. Hayashi, T. Nakanishi, T. Watanabe, Y. Kokubun, T. Takahata, and T. Kobayashi, "Realizing a 36-core, 3-mode Fiber with 108 Spatial Channels," in *Optical Fiber Communication Conference*, 2015, p. Th5C.2.

[58] K. Igarashi, D. Souma, Y. Wakayama, K. Takeshima, Y. Kawaguchi, T. Tsuritani, I. Morita, and M. Suzuki, "114 Space-Division-Multiplexed Transmission over 9.8-km Weakly-Coupled-6-Mode Uncoupled-19-Core Fibers," in *Optical Fiber Communication Conference*, 2015, p. Th5C.4.

[59] K. Shibahara, T. Mizuno, H. Takara, A. Sano, H. Kawakami, D. Lee, Y. Miyamoto, H. Ono, M. Oguma, Y. Abe, T. Kobayashi, T. Matsui, R. Fukumoto, Y. Amma, T. Hosokawa, S. Matsuo, K. Saitoh, H. Nasu, and T. Morioka, "Dense SDM (12-core×3-mode) Transmission over 527 km with 33.2-ns Mode-Dispersion Employing Low-Complexity Parallel MIMO Frequency-Domain Equalization," in *Optical Fiber Communication Conference*, 2015, p. Th5C.3.

[60] D. Soma, K. Igarashi, Y. Wakayama, K. Takeshima, Y. Kawaguchi, N. Yoshikane, T. Tsuritani, I. Morita, and M. Suzuki, "2.05 Peta-bit/s super-nyquist-WDM SDM transmission using 9.8-km 6-mode 19-core fiber in full C band," in *European Conference and Exhibition on Optical Communication*, 2015, p. PDP.3.2.

[61] R. Ryf, N. K. Fontaine, M. Montoliu, S. Randel, B. Ercan, H. Chen, S. Chandrasekhar, A. Gnauck, S. G. Leon-Saval, J. Bland-Hawthorn, J. R. Salazar Gil, Y. Sun, and R. Lingle, "Photonic-Lantern-Based Mode Multiplexers for Few-Mode-Fiber Transmission," in *Optical Fiber Communication Conference*, 2014, p. W4J.2.

[62] S. Iano, T. Sato, S. Sentsui, T. Kuroha, and Y. Nishimura, "Multicore optical fiber," in *Optical Fiber Communication Conference*, 1979, p. WB1.

[63] K. Saitoh and T. Matsui, "Multi-core hole-assisted fibers for high core density space division multiplexing," in *OptoElectronics and Communications Conference*, 2010, pp. 7C2–1.

[64] T. Hayashi, T. Taru, O. Shimakawa, T. Sasaki, and E. Sasaoka, "Low-Crosstalk and Low-Loss Multi-Core Fiber Utilizing Fiber Bend," in *Optical Fiber Communication Conference/National Fiber Optic Engineers Conference*, 2011, p. OWJ3.

[65] S. Matsuo, K. Takenaga, Y. Arakawa, Y. Sasaki, S. Taniagwa, K. Saitoh, and M. Koshiba, "Large-effective-area ten-core fiber with cladding diameter of about 200 μm," *Opt. Lett.*, vol. 36, no. 23, pp. 4626–4628, Dec. 2011.

[66] M. Koshiba, K. Saitoh, and Y. Kokubun, "Heterogeneous multi-core fibers: proposal and design principle," *IEICE Electron. Express*, vol. 6, no. 2, pp. 98–103, 2009.

[67] K. Takenaga, S. Tanigawa, N. Guan, S. Matsuo, K. Saitoh, and M. Koshiba, "Reduction of Crosstalk by Quasi-Homogeneous Solid Multi-Core Fiber," in *Optical Fiber Communication Conference/National Fiber Optic Engineers Conference*, 2010, p. OWK7.

[68] S. Matsuo, Y. Sasaki, T. Akamatsu, I. Ishida, K. Takenaga, K. Okuyama, K. Saitoh, and M. Kosihba, "12-Core Fiber With One Ring Structure for Extremely Large Capacity Transmission," *Opt. Express*, vol. 20, no. 27, pp. 28398–28408, 2012.

[69] K. Takenaga, S. Matsuo, K. Saitoh, and M. Koshiba, "Multicore fiber with ring structure," in *IEEE Photonics Society Summer Topical Meeting Series*, 2013, p. MC2.1.

[70] S. Berdagué and P. Facq, "Mode division multiplexing in optical fibers," *Appl. Opt.*, vol. 21, no. 11, pp. 1950–5, Jun. 1982.

[71] P. Sillard, D. Molin, M. Bigot-Astruc, K. De Jongh, F. Achten, A. M. Velazquez-Benitez, R. Amezcua-Correa, and C. M. Okonkwo, "Low-Differential-Mode-Group-Delay 9-LP-Mode Fiber," *J. Light. Technol.*, vol. 34, no. 2, pp. 425–430, Jan. 2016.

[72] P. Sillard, D. Molin, M. Bigot-Astruc, K. de Jongh, and F. Achten, "Low-Differential-Mode-Group-Delay 9-LP-Mode Fiber," in *Optical Fiber Communication Conference*, 2015, vol. 1, no. 1, p. M2C.2.

[73] C. Koebele, M. Salsi, G. Charlet, and S. Bigo, "Nonlinear Effects in Mode-Division-Multiplexed Transmission Over Few-Mode Optical Fiber," *IEEE Photonics Technol. Lett.*, vol. 23, no. 18, pp. 1316–1318, Sep. 2011.

[74] K.-P. Ho and J. M. Kahn, "Mode-dependent loss and gain: statistics and effect on mode-division multiplexing," *Opt. Express*, vol. 19, no. 17, pp. 16612–16635, Aug. 2011.

[75] R. J. Essiambre, M. a. Mestre, R. Ryf, A. H. Gnauck, R. W. Tkach, A. R. Chraplyvy, Y. Sun, X. Jiang, and R. Lingle, "Experimental investigation of inter-modal four-wave mixing in few-mode fibers," *IEEE Photonics Technol. Lett.*, vol. 25, no. 6, pp. 539–542, 2013.

[76] R. J. Essiambre, M. a. Mestre, R. Ryf, A. H. Gnauck, R. W. Tkach, A. R. Chraplyvy, Y. Sun, X. Jiang, and R. Lingle, “Experimental observation of inter-modal cross-phase modulation in few-mode fibers,” *IEEE Photonics Technol. Lett.*, vol. 25, no. 6, pp. 535–538, 2013.

[77] C. Koebele, M. Salsi, D. Sperti, P. Tran, P. Brindel, H. Mardoyan, S. Bigo, A. Boutin, F. Verluise, P. Sillard, M. Astruc, L. Provost, F. Cerou, and G. Charlet, “Two mode transmission at 2×100Gb/s, over 40km-long prototype few-mode fiber, using LCOS-based programmable mode multiplexer and demultiplexer,” *Opt. Express*, vol. 19, no. 17, pp. 16593–16600, Aug. 2011.

[78] A. Al Amin, A. Li, S. Chen, X. Chen, G. Gao, and W. Shieh, “Dual-LP_{11} mode 4×4 MIMO-OFDM transmission over a two-mode fiber,” *Opt. Express*, vol. 19, no. 17, pp. 16672–16679, Aug. 2011.

[79] G. Labroille, B. Denolle, P. Jian, P. Genevaux, N. Treps, and J.-F. Morizur, “Efficient and mode selective spatial mode multiplexer based on multi-plane light conversion,” *Opt. Express*, vol. 22, no. 13, pp. 15599–15607, 2014.

[80] H. Bülow, H. Al-Hashimi, B. Schmauss, and H. Bulow, “Stable coherent MIMO transport over few mode fiber enabled by an adiabatic mode splitter,” in *European Conference and Exhibition on Optical Communication*, 2010, p. P4.04.

[81] H. Chen, B. H.P.A. van den, and T. Koonen, “30Gbit/s 3×3 Optical Mode Group Division Multiplexing System with Mode-Selective Spatial Filtering,” in *Optical Fiber Communication Conference/National Fiber Optic Engineers Conference*, 2011, p. OWB1.

[82] K. Igarashi, D. Souma, T. Tsuritani, and I. Morita, “Performance evaluation of selective mode conversion based on phase plates for a 10-mode fiber,” *Opt. Express*, vol. 22, no. 17, pp. 20881–20893, 2014.

[83] J. von Hoyningen-Huene, R. Ryf, and P. Winzer, “LCoS-based mode shaper for few-mode fiber,” *Opt. Express*, vol. 21, no. 15, pp. 18097–18110, Jul. 2013.

[84] R. Ryf, M. A. Mestre, A. Gnauck, S. Randel, C. Schmidt, R. Essiambre, P. Winzer, R. Delbue, P. Pupalaikis, A. Sureka, Y. Sun, X. Jiang, D. Peckham, A. H. McCurdy, and R. Lingle, “Low-Loss Mode Coupler for Mode-Multiplexed transmission in Few-Mode Fiber,” in *Optical Fiber Communication Conference/National Fiber Optic Engineers Conference*, 2012, p. PDP5B.5.

[85] S. Ramachandran, Z. Wang, and M. Yan, “Bandwidth control of long-period grating-based mode converters in few-mode fibers,” *Opt. Lett.*, vol. 27, no. 9, pp. 698–700, May 2002.

[86] T. A. M. J. Koonen, H. Chen, H. P. a Van Den Boom, and O. Raz, "Silicon photonic integrated mode multiplexer and demultiplexer," *IEEE Photonics Technol. Lett.*, vol. 24, no. 21, pp. 1961–1964, 2012.

[87] P. Krummrich and K. Petermann, "Evaluation of Potential Optical Amplifier Concepts for Coherent Mode Multiplexing," in *Optical Fiber Communication Conference/National Fiber Optic Engineers Conference*, 2011, p. OMH5.

[88] K. S. Abedin, J. M. Fini, T. F. Thierry, B. Zhu, M. F. Yan, L. Bansal, F. V Dimarcello, E. M. Monberg, and D. J. DiGiovanni, "Seven-core erbium-doped double-clad fiber amplifier pumped simultaneously by side-coupled multimode fiber," *Opt. Lett.*, vol. 39, no. 4, pp. 993–996, Feb. 2014.

[89] P. Genevaux, C. Simonneau, G. Le Cocq, Y. Quiquempois, L. Bigot, A. Boutin, and G. Charlet, "A Five-Mode Erbium-Doped Fiber Amplifier for Mode-Division Multiplexing Transmission," *J. Light. Technol.*, vol. 34, no. 2, pp. 456–462, Jan. 2016.

[90] C. Jin, B. Huang, K. Shang, H. Chen, R. Ryf, R. J. Essiambre, N. K. Fontaine, G. Li, L. Wang, Y. Messaddeq, and S. LaRochelle, "Efficient annular cladding amplifier with six, three-mode cores," in *European Conference and Exposition on Optical Communication*, 2015, p. PDP.2.1.

[91] G. Le Cocq, L. Bigot, A. Le Rouge, M. Bigot-Astruc, P. Sillard, and Y. Quiquempois, "Design and Characterization of a Multimode EDFA Supporting 4 Transverse Mode Groups for Modal Division Multiplexed Transmissions," in *European Conference and Exhibition on Optical Communication*, 2012, p. Tu.3.F.4.

[92] Q. Kang, E.-L. Lim, Y. Jung, J. K. Sahu, F. Poletti, C. Baskiotis, S.-U. Alam, and D. J. Richardson, "Accurate modal gain control in a multimode erbium doped fiber amplifier incorporating ring doping and a simple LP_{01} pump configuration," *Opt. Express*, vol. 20, no. 19, pp. 20835–20843, Sep. 2012.

[93] C. Jin, B. Ung, Y. Messaddeq, and S. LaRochelle, "Tailored modal gain in a multi-mode erbium-doped fiber amplifier based on engineered ring doping profiles," in *Photonics North*, 2013, vol. 8915, p. 89150A.

[94] D. Askarov and J. M. Kahn, "Design of Transmission Fibers and Doped Fiber Amplifiers for Mode-Division Multiplexing," *IEEE Photonics Technol. Lett.*, vol. 24, no. 21, pp. 1945–1948, Nov. 2012.

[95] E. Ip, "Gain Equalization for Few-Mode Fiber Amplifiers Beyond Two Propagating Mode Groups," *IEEE Photonics Technol. Lett.*, vol. 24, no. 21, pp. 1933–1936, Nov. 2012.

[96] Y. Jung, S. Alam, Z. Li, A. Dhar, D. Giles, I. P. Giles, J. K. Sahu, F. Poletti, L. Grüner-Nielsen, and D. J. Richardson, "First demonstration and detailed characterization of

a multimode amplifier for space division multiplexed transmission systems," *Opt. Express*, vol. 19, no. 26, pp. B952–B957, Dec. 2011.

[97] N. Bai, E. Ip, Y.-K. Huang, E. Mateo, F. Yaman, M.-J. Li, S. Bickham, S. Ten, J. Liñares, C. Montero, V. Moreno, X. Prieto, V. Tse, K. Man Chung, A. P. T. Lau, H.-Y. Tam, C. Lu, Y. Luo, G.-D. Peng, G. Li, and T. Wang, "Mode-division multiplexed transmission with inline few-mode fiber amplifier," *Opt. Express*, vol. 20, no. 3, pp. 2668–2680, Jan. 2012.

[98] M. Salsi, J. Vuong, C. Koebele, P. Genevaux, H. Mardoyan, P. Tran, S. Bigo, G. Le Cocq, L. Bigot, Y. Quiquempois, A. Le Rouge, P. Sillard, M. Bigot-Astruc, and G. Charlet, "In-line Few-Mode Optical Amplifier with Erbium Profile Tuned to Support LP_{01}, LP_{11}, and LP_{21} Mode Groups," in *European Conference and Exhibition on Optical Communication*, 2012, p. Tu.3.F.1.

[99] M. Salsi, D. Peyrot, G. Charlet, S. Bigo, R. Ryf, N. K. Fontaine, M. a. Mestre, S. Randel, X. Palou, C. Bolle, B. Guan, G. Le Cocq, L. Bigot, and Y. Quiquempois, "A Six-Mode Erbium-Doped Fiber Amplifier," in *European Conference and Exhibition on Optical Communication*, 2012, p. Th.3.A.6.

[100] G. Le Cocq, L. Bigot, A. Le Rouge, M. Bigot-Astruc, P. Sillard, C. Koebele, M. Salsi, and Y. Quiquempois, "Modeling and characterization of a few-mode EDFA supporting four mode groups for mode division multiplexing," *Opt. Express*, vol. 20, no. 24, pp. 27051–27061, Nov. 2012.

[101] V. A. J. M. Sleiffer, Y. Jung, V. Veljanovski, R. G. H. van Uden, M. Kuschnerov, H. Chen, B. Inan, L. G. Nielsen, Y. Sun, D. J. Richardson, S. U. Alam, F. Poletti, J. K. Sahu, A. Dhar, A. M. J. Koonen, B. Corbett, R. Winfield, A. D. Ellis, and H. de Waardt, "73.7 Tb/s (96×3×256-Gb/s) mode-division-multiplexed DP-16QAM transmission with inline MM-EDFA," *Opt. Express*, vol. 20, no. 26, pp. B428–B438, Nov. 2012.

[102] Y. Jung, Q. Kang, V. A. J. M. Sleiffer, B. Inan, M. Kuschnerov, V. Veljanovski, B. Corbett, R. Winfield, Z. Li, P. S. Teh, A. Dhar, J. Sahu, F. Poletti, S.-U. Alam, and D. J. Richardson, "Three mode Er^{3+} ring-doped fiber amplifier for mode-division multiplexed transmission," *Opt. Express*, vol. 21, no. 8, pp. 10383–10392, 2013.

[103] E. Ip, M. Li, and C. Montero, "Experimental Characterization of a Ring-Profile Few-Mode Erbium-Doped Fiber Amplifier enabling Gain Equalization," in *Optical Fiber Communication Conference/National Fiber Optic Engineers Conference*, 2013, p. JTh2A.18.

[104] K. S. Abedin, T. F. Taunay, M. Fishteyn, M. F. Yan, B. Zhu, J. M. Fini, E. M. Monberg, F. V Dimarcello, and P. W. Wisk, "Amplification and noise properties of an erbium-doped multicore fiber amplifier," *Opt. Express*, vol. 19, no. 17, pp. 16715–16721, Aug. 2011.

[105] K. S. Abedin, T. F. Taunay, M. Fishteyn, D. J. DiGiovanni, V. R. Supradeepa, J. M. Fini, M. F. Yan, B. Zhu, E. M. Monberg, and F. V Dimarcello, “Cladding-pumped erbium-doped multicore fiber amplifier,” *Opt. Express*, vol. 20, no. 18, pp. 20191–20200, Aug. 2012.

[106] H. Masuda, H. Ono, H. Takara, Y. Miyamoto, K. Ichii, K. Takenaga, S. Matsuo, K. Kitamura, Y. Abe, and M. Yamada, “Remotely pumped multicore erbium-doped fiber amplifier system with high pumping efficiency,” in *IEEE Photonics Society Summer Topical Meeting Series*, 2013, p. WC3.3.

[107] Y. Tsuchida, M. Tadakuma, and R. Sugizaki, “Multicore EDFA for Space Division Multiplexing by Utilizing Cladding-pumped Technology,” in *Optical Fiber Communication Conference*, 2014, p. Tu2D.1.

[108] H. Chen, N. K. Fontaine, R. Ryf, R.-J. Essiambre, L. Wang, Y. Messaddeq, S. LaRochelle, T. Hayashi, T. Nagashima, and T. Sasaki, “Transmission over coupled six-core fiber with two in-line cladding-pumped six-core EDFAs,” in *European Conference and Exhibition on Optical Communication*, 2015, p. We.1.4.2.

[109] H. Chen, N. K. Fontaine, R. Ryf, C. Jin, B. Huang, K. Shang, R.-J. Essiambre, L. Wang, T. Hayashi, T. Nagashima, T. Sasaki, Y. Messaddeq, and S. LaRochelle, “Demonstration of Cladding-Pumped Six-Core Erbium-Doped Fiber Amplifier,” *J. Light. Technol.*, vol. 34, no. 8, pp. 1654–1660, Apr. 2016.

[110] N. Bai, E. Ip, T. Wang, and G. Li, “Multimode fiber amplifier with tunable modal gain using a reconfigurable multimode pump,” *Opt. Express*, vol. 19, no. 17, pp. 16601–16611, Aug. 2011.

[111] Y. Jung, Q. Kang, J. K. Sahu, B. Corbett, F. Poletti, R. Winfield, S. U. Alam, and D. J. Richardson, “Few-mode EDFA Supporting 5 Spatial Modes with Reconfigurable Differential Modal Gain Control,” in *European Conference and Exhibition on Optical Communication*, 2013, p. We.4.A.2.

[112] M. Wada, T. Sakamoto, T. Mori, T. Yamamoto, N. Hanzawa, and F. Yamamoto, “Modal Gain Controllable 2-LP-Mode Fiber Amplifier Using PLC Type Coupler and Long-Period Grating,” *J. Light. Technol.*, vol. 32, no. 24, pp. 4092–4098, 2014.

[113] H. Ono, T. Hosokawa, K. Ichii, S. Matsuo, H. Nasu, and M. Yamada, “2-LP mode few-mode fiber amplifier employing ring-core erbium-doped fiber,” *Opt. Express*, vol. 23, no. 21, pp. 27405–27418, Oct. 2015.

[114] Q. Kang, P. Gregg, Y. Jung, E. L. Lim, S. Alam, S. Ramachandran, and D. J. Richardson, “Amplification of 12 OAM Modes in an air-core erbium doped fiber,” *Opt. Express*, vol. 23, no. 22, pp. 28341–28348, Nov. 2015.

[115] E. Ip, Y. G. Ruo, M.-J. Li, Y.-K. Huang, and J. Kahn, "Experimental demonstration of a Gain-Flattening Filter for Few-Mode Fiber based on a Spatial Light Modulator," in *Optical Fiber Communication Conference*, 2014, p. Th4A.5.

[116] M. Blau, I. Weiss, J. Gerufi, D. Sinefeld, M. Bin-Nun, R. Lingle, L. Grüner-Nielsen, and D. M. Marom, "Variable optical attenuator and dynamic mode group equalizer for few mode fibers," *Opt. Express*, vol. 22, no. 25, pp. 30520–30527, 2014.

[117] Y. Jung, E. L. Lim, Q. Kang, T. C. May-Smith, N. H. L. Wong, R. Standish, F. Poletti, J. K. Sahu, S. U. Alam, and D. J. Richardson, "Cladding pumped few-mode EDFA for mode division multiplexed transmission," *Opt. Express*, vol. 22, no. 23, pp. 29008–29013, 2014.

[118] J. Sakaguchi, W. Klaus, B. J. Puttnam, J. M. D. Mendinueta, Y. Awaji, N. Wada, Y. Tsuchida, K. Maeda, M. Tadakuma, K. Imamura, R. Sugizaki, T. Kobayashi, Y. Tottori, M. Watanabe, and R. V Jensen, "19-core MCF transmission system using EDFA with shared core pumping coupled via free-space optics," *Opt. Express*, vol. 22, no. 1, pp. 90–95, 2014.

[119] S. Jain, T. C. May-Smith, A. Dhar, a S. Webb, M. Belal, D. J. Richardson, J. K. Sahu, and D. N. Payne, "Erbium-doped multi-element fiber amplifiers for space-division multiplexing operations," *Opt. Lett.*, vol. 38, no. 4, pp. 582–584, 2013.

[120] M. Yamada, K. Tsujikawa, L. Ma, K. Ichii, S. Matsuo, N. Hanzawa, and H. Ono, "Optical Fiber Amplifier Employing a Bundle of Reduced Cladding Erbium-Doped Fibers," *IEEE Photonics Technol. Lett.*, vol. 24, no. 21, pp. 1910–1913, Nov. 2012.

[121] K. S. Abedin, J. M. Fini, T. F. Thierry, V. R. Supradeepa, B. Zhu, M. F. Yan, L. Bansal, E. M. Monberg, and D. J. DiGiovanni, "Multicore Erbium Doped Fiber Amplifiers for Space Division Multiplexing Systems," *J. Light. Technol.*, vol. 32, no. 16, pp. 2800–2808, Aug. 2014.

[122] D. E. McCumber, "Einstein relations connecting broadband emission and absorption spectra," *Phys. Rev.*, vol. 136, no. 4A, pp. 16–19, 1964.

[123] C. Giles and E. Desurvire, "Modeling erbium-doped fiber amplifiers," *J. Light. Technol.*, vol. 9, no. 2, pp. 271–283, 1991.

[124] P. C. Becker, N. A. Olsson, and J. R. Simpson, *Erbium-Doped Fiber Amplifiers: Fundamentals and Technology*, 1st ed. San Diego, CA: Academic Press, 1999.

[125] R. W. Tkach, "Scaling optical communications for the next decade and beyond," *Bell Labs Tech. J.*, vol. 14, no. 4, pp. 3–9, Feb. 2010.

[126] P. J. Winzer, "Energy-Efficient Optical Transport Capacity Scaling Through Spatial Multiplexing," *IEEE Photonics Technol. Lett.*, vol. 23, no. 13, pp. 851–853, Jul. 2011.

[127] S. Murshid, B. Grossman, and P. Narakorn, “Spatial domain multiplexing: A new dimension in fiber optic multiplexing,” *Opt. Laser Technol.*, vol. 40, no. 8, pp. 1030–1036, Nov. 2008.

[128] R. Ryf, S. Randel, R.-J. Essiambre, and P. J. Winzer, “Space-division multiplexed transmission over few-mode- and coupled-core fiber based on coherent MIMO digital signal processing,” vol. 8284, pp. 828402–828402–13, 2012.

[129] J. Wang, J.-Y. Yang, I. M. Fazal, N. Ahmed, Y. Yan, H. Huang, Y. Ren, Y. Yue, S. Dolinar, M. Tur, and A. E. Willner, “Terabit free-space data transmission employing orbital angular momentum multiplexing,” *Nat. Photonics*, vol. 6, pp. 488–496, 2012.

[130] T. Hayashi, T. Taru, O. Shimakawa, T. Sasaki, and E. Sasaoka, “Design and fabrication of ultra-low crosstalk and low-loss multi-core fiber,” *Opt. Express*, vol. 19, no. 17, pp. 16576–16592, Aug. 2011.

[131] B. Zhu, T. F. Taunay, M. Fishteyn, X. Liu, S. Chandrasekhar, M. F. Yan, J. M. Fini, E. M. Monberg, and F. V Dimarcello, “112-Tb/s space-division multiplexed DWDM transmission with 14-b/s/Hz aggregate spectral efficiency over a 76.8-km seven-core fiber,” *Opt. Express*, vol. 19, no. 17, pp. 16665–16671, Aug. 2011.

[132] G. Nykolak, S. A. Kramer, J. R. Simpson, D. J. DiGiovanni, C. R. Giles, and H. M. Presby, “An erbium-doped multimode optical fiber amplifier,” *IEEE Photonics Technol. Lett.*, vol. 3, no. 12, pp. 1079–1081, Dec. 1991.

[133] Y. Yung, S. Alam, Z. Li, A. Dhar, D. Giles, I. Giles, J. Sahu, L. Grüner-Nielsen, F. Poletti, and D. Richardson, “First demonstration of multimode amplifier for spatial division multiplexed transmission systems,” in *European Conference and Exposition on Optical Communications*, 2011, p. Th.13.K.4.

[134] R. Ryf, R. Essiambre, J. von Hoyningen-Huene, and P. Winzer, “Analysis of Mode-Dependent Gain in Raman Amplified Few-Mode Fiber,” in *Optical Fiber Communication Conference/National Fiber Optic Engineers Conference*, 2012, p. OW1D.2.

[135] Q. Kang, E. L. Lim, Y. Jung, F. Poletti, S. Alam, and D. J. Richardson, “Design of Four-Mode Erbium Doped Fiber Amplifier with Low Differential Modal Gain for Modal Division Multiplexed Transmissions,” in *Optical Fiber Communication Conference/National Fiber Optic Engineers Conference*, 2013, p. OTu3G.3.

[136] M. Gong, Y. Yuan, C. Li, P. Yan, H. Zhang, and S. Liao, “Numerical modeling of transverse mode competition in strongly pumped multimode fiber lasers and amplifiers,” *Opt. Express*, vol. 15, no. 6, pp. 3236–3246, Mar. 2007.

[137] D. Gloge, “Weakly Guiding Fibers,” *Appl. Opt.*, vol. 10, no. 10, pp. 2252–2258, Oct. 1971.

[138] B. Huang, H. Chen, N. K. Fontaine, C. Jin, K. Shang, R. Ryf, R.-J. Essiambre, B. Ung, Y. Messaddeq, S. LaRochelle, and G. Li, “Characterization of Space-Division Multiplexing Amplifiers Using a Swept Wavelength Coherent Reflectometer,” in *Optical Fiber Communication Conference*, 2016, p. W4F.2.

[139] P. J. Winzer, “Making spatial multiplexing a reality,” *Nat. Photonics*, vol. 8, pp. 345–348, 2014.

[140] G. Li, N. Bai, N. Zhao, and C. Xia, “Space-division multiplexing: the next frontier in optical communication,” *Adv. Opt. Photonics*, vol. 6, no. 4, p. 413, Dec. 2014.

[141] P. M. Krummrich and S. Akhtari, “Selection of energy optimized pump concepts for multi core and multi mode erbium doped fiber amplifiers,” *Opt. Express*, vol. 22, no. 24, pp. 30267–30280, Dec. 2014.

[142] R. Ryf, N. K. Fontaine, H. Chen, B. Guan, B. Huang, M. Esmaeelpour, a H. Gnauck, S. Randel, S. J. B. Yoo, A. M. J. Koonen, R. Shubochkin, Y. Sun, and R. Lingle, “Mode-multiplexed transmission over conventional graded-index multimode fibers,” *Opt. Express*, vol. 23, no. 1, pp. 235–246, Jan. 2015.

[143] J. Sakaguchi, B. J. Puttnam, W. Klaus, J.-M. Delgado-Mendinueta, Y. Awaji, N. Wada, A. Kanno, and T. Kawanishi, “Large-capacity transmission over a 19-core fiber,” in *Optical Fiber Communication Conference/National Fiber Optic Engineers Conference*, 2013, p. OW1I.3.

[144] N. K. Fontaine, T. Haramaty, R. Ryf, H. Chen, L. Miron, L. Pascar, M. Blau, B. Frenkel, L. Wang, Y. Messaddeq, S. LaRochelle, R.-J. Essiambre, Y. Jung, Q. Kang, J. K. Sahu, S.-U. Alam, D. J. Richardson, and D. M. Marom, “Heterogeneous Space-Division Multiplexing and Joint Wavelength Switching Demonstration,” in *Optical Fiber Communication Conference*, 2015, p. Th5C.5.

[145] P. M. Krummrich, “Optical amplification and optical filter based signal processing for cost and energy efficient spatial multiplexing,” *Opt. Express*, vol. 19, no. 17, pp. 16636–16652, Aug. 2011.

[146] P. Krummrich and S. Akhtari, “Optical Amplifiers for Cost and Energy Efficient Spatial Division Multiplexing,” in *Frontiers in Optics 2013/Laser Science XXIX*, 2013, p. FM4B.1.

[147] H. Takara, H. Ono, Y. Abe, H. Masuda, K. Takenaga, S. Matsuo, H. Kubota, K. Shibahara, T. Kobayashi, and Y. Miaymoto, “1000-km 7-core fiber transmission of 10×96-Gb/s PDM-16QAM using Raman amplification with 65 W per fiber,” *Opt. Express*, vol. 20, no. 9, pp. 10100–10105, Apr. 2012.

[148] L. Gagné-Godbout, “Modélisation, fabrication et caractérisation d’un amplificateur à fibre optique à sept coeurs dopés à l'erbium,” Université Laval, 2014.

[149] C. Jin, B. Ung, Y. Messaddeq, and S. LaRochelle, "Annular Cladding Erbium-Doped Multi-Core Fiber for SDM Amplification," in *Conference on Lasers and Electro-Optics*, 2015, p. JW2A.95.

[150] H. Uemura, K. Takenaga, T. Ori, and S. Matsuo, "Fused Taper Type Fan-in/Fan-out Device for Multicore EDF," in *OptoElectronics and Communications Conference*, 2013, p. TuS1_4.

[151] P. Mitchell, G. Brown, R. R. Thomson, N. Psaila, and A. Kar, "57 Channel (19×3) Spatial Multiplexer Fabricated using Direct Laser Inscription," in *Optical Fiber Communication Conference*, 2014, p. M3K.5.

[152] D. J. Ripin and L. Goldberg, "High efficiency side-coupling of light into optical fibres using imbedded v-grooves," *Electron. Lett.*, vol. 31, no. 25, p. 2204, 1995.

[153] T. Theeg, H. Sayinc, J. Neumann, L. Overmeyer, and D. Kracht, "Pump and signal combiner for bi-directional pumping of all-fiber lasers and amplifiers," *Opt. Express*, vol. 20, no. 27, pp. 28125–41, 2012.

[154] R.-J. Essiambre, G. Kramer, P. J. Winzer, G. J. Foschini, and B. Goebel, "Capacity Limits of Optical Fiber Networks," *J. Light. Technol.*, vol. 28, no. 4, pp. 662–701, Feb. 2010.

[155] J. Sakaguchi, W. Klaus, B. J. Puttnam, J.-M. D. Mendinueta, Y. Awaji, N. Wada, Y. Tsuchida, K. Maeda, M. Tadakuma, K. Imamura, R. Sugizaki, T. Kobayashi, Y. Tottori, M. Watanabe, and R. V. Jensen, "19-core MCF transmission system using EDFA with shared core pumping coupled in free-space optics," in *European Conference and Exhibition on Optical Communication*, 2013, p. Th.1.C.6.

[156] C. Jin, B. Ung, Y. Messaddeq, and S. LaRochelle, "Annular-cladding erbium doped multicore fiber for SDM amplification," *Opt. Express*, vol. 23, no. 23, pp. 29647–29659, Nov. 2015.

[157] W. Klaus, J. Sakaguchi, B. J. Puttnam, Y. Awaji, N. Wada, T. Kobayashi, and M. Watanabe, "Free-Space Coupling Optics for Multicore Fibers," *IEEE Photonics Technol. Lett.*, vol. 24, no. 21, pp. 1902–1905, Nov. 2012.

[158] B. Huang, N. K. Fontaine, R. Ryf, B. Guan, S. G. Leon-Saval, R. Shubochkin, Y. Sun, R. Lingle, and G. Li, "All-fiber mode-group-selective photonic lantern using graded-index multimode fibers," *Opt. Express*, vol. 23, no. 1, pp. 224–234, Jan. 2015.

[159] K. Watanabe, T. Saito, K. Imamura, and M. Shiino, "Development of fiber bundle type fan-out for 19-core multicore fiber," in *Optoelectronics and Communications Conference and the Australian Conference on Optical Fibre Technology*, 2014, p. MO1E–2.

[160] R. R. Thomson, H. T. Bookey, N. D. Psaila, A. Fender, S. Campbell, W. N. MacPherson, J. S. Barton, D. T. Reid, and A. K. Kar, "Ultrafast-laser inscription of a three dimensional fan-out device for multicore fiber coupling applications," *Opt. Express*, vol. 15, no. 18, pp. 11691–11697, Sep. 2007.

[161] H. Chen, N. K. Fontaine, R. Ryf, B. Guan, S. J. Ben Yoo, and T. A. M. J. Koonen, "Design Constraints of Photonic-Lantern Spatial Multiplexer Based on Laser-Inscribed 3-D Waveguide Technology," *J. Light. Technol.*, vol. 33, no. 6, pp. 1147–1154, Mar. 2015.

[162] C. R. Doerr, N. Fontaine, M. Hirano, T. Sasaki, L. Buhl, and P. Winzer, "Silicon photonic integrated circuit for coupling to a ring-core multimode fiber for space-division multiplexing," in *European Conference and Exposition on Optical Communications*, 2011, p. Th.13.A.3.

[163] H. Chen, R. van Uden, C. Okonkwo, and T. Koonen, "Compact spatial multiplexers for mode division multiplexing," *Opt. Express*, vol. 22, no. 26, pp. 31582–31594, Dec. 2014.

[164] L. Gruner-Nielsen, Y. Sun, J. W. Nicholson, D. Jakobsen, R. Lingle, and B. Palsdottir, "Few Mode Transmission Fiber with low DGD, low Mode Coupling and low Loss," in *Optical Fiber Communication Conference/National Fiber Optic Engineers Conference*, 2012, p. PDP5A.1.

[165] P. Sillard, M. Bigot-Astruc, and D. Molin, "Few-mode fibers for mode-division-multiplexed systems," *J. Light. Technol.*, vol. 32, no. 16, pp. 2824–2829, 2014.

[166] T. Hayashi, T. Taru, O. Shimakawa, T. Sasaki, and E. Sasaoka, "Characterization of Crosstalk in Ultra-Low-Crosstalk Multi-Core Fiber," *J. Light. Technol.*, vol. 30, no. 4, pp. 583–589, Feb. 2012.

[167] K. Imamura, T. Gonda, and R. Sugizaki, "19-Core fiber with new core arrangement to realize low crosstalk," in *Optoelectronics and Communications Conference and the Australian Conference on Optical Fibre Technology*, 2014, p. TU5C–3.

[168] E. Ip, M. J. Li, K. Bennett, Y. K. Huang, A. Tanaka, A. Korolev, K. Koreshkov, W. Wood, E. Mateo, J. Hu, and Y. Yano, "146λ×6×19-Gbaud wavelength-and mode-division multiplexed transmission over 10×50-km spans of few-mode fiber with a gain-equalized few-mode EDFA," *J. Light. Technol.*, vol. 32, no. 4, pp. 790–797, 2014.

[169] K. Igarashi, K. Takeshima, T. Tsuritani, H. Takahashi, S. Sumita, I. Morita, Y. Tsuchida, M. Tadakuma, K. Maeda, T. Saito, K. Watanabe, K. Imamura, R. Sugizaki, and M. Suzuki, "1109-Tbit/s SDM transmission over 6,370 km using a full C-band seven-core EDFA," *Opt. Express*, vol. 21, no. 15, pp. 18053–18060, Jul. 2013.

[170] R. Miyabe, Y. Tsuchida, K. Maeda, H. Matsuura, S. Takasaka, Y. Mimura, R. Sugizaki, K. Doi, K. Aiso, M. Tadakuma, and W. Kumagai, "Cladding-Pumped Seven-Core EDFA Using a Multimode Pump Light Coupler," in *European Conference and Exhibition on Optical Communication*, 2013, p. We.4.A.5.

[171] K. Ichii, H. Masuda, M. Yamada, K. Takenaga, T. Takahashi, S. Matsuo, and H. Ono, "12-Core Double-Clad Er/Yb-Doped Fiber Amplifier Employing Free-space Coupling Pump/Signal Combiner Module," in *European Conference and Exhibition on Optical Communication*, 2013, p. We.4.A.4.

[172] J. P. Koplow, S. W. Moore, and D. A. V. Kliner, "A new method for side pumping of double-clad fiber sources," *IEEE J. Quantum Electron.*, vol. 39, no. 4, pp. 529–540, Apr. 2003.

[173] C. Jauregui, S. Böhme, G. Wenetiadis, J. Limpert, and A. Tünnermann, "Side-pump combiner for all-fiber monolithic fiber lasers and amplifiers," *J. Opt. Soc. Am. B*, vol. 27, no. 5, pp. 1011–1015, May 2010.

[174] K.-S. Kim and S. E. Pratsinis, "Manufacture of optical waveguide preforms by modified chemical vapor deposition," *AIChE J.*, vol. 34, no. 6, pp. 912–921, Jun. 1988.

[175] P. Geittner, D. Küppers, and H. Lydtin, "Low-loss optical fibers prepared by plasma-activated chemical vapor deposition (CVD)," *Appl. Phys. Lett.*, vol. 28, no. 11, pp. 645–646, 1976.

[176] T. Izawa and N. Inagaki, "Materials and processes for fiber preform fabrication—Vapor-phase axial deposition," *Proc. IEEE*, vol. 68, no. 10, pp. 1184–1187, 1980.

[177] P. C. Schultz, "Fabrication of optical waveguides by the outside vapor deposition process," *Proc. IEEE*, vol. 68, no. 10, pp. 1187–1190, 1980.

[178] J. E. Townsend, S. B. Poole, and D. N. Payne, "Solution-doping technique for fabrication of rare-earth-doped optical fibres," *Electron. Lett.*, vol. 23, no. 7, pp. 329–331, 1987.

[179] J. Laegsgaard and A. Bjarklev, "Microstructured Optical Fibers-Fundamentals and Applications," *J. Am. Ceram. Soc.*, vol. 89, no. 1, pp. 2–12, 2006.

[180] P. Russell, "Photonic crystal fibers," *Science*, vol. 299, no. 5605, pp. 358–362, 2003.

[181] A. Dhar, M. C. Paul, M. Pal, A. K. Mondal, S. Sen, H. S. Maiti, and R. Sen, "Characterization of porous core layer for controlling rare earth incorporation in optical fiber," *Opt. Express*, vol. 14, no. 20, pp. 9006–9015, 2006.

[182] F. Z. Tang, P. McNamara, G. W. Barton, and S. P. Ringer, “Multiple solution-doping in optical fibre fabrication I - Aluminium doping,” *J. Non. Cryst. Solids*, vol. 354, no. 10–11, pp. 927–937, 2008.

[183] B. Guan, B. Ercan, N. K. Fontaine, R. P. Scott, and S. J. B. Yoo, “Mode-Group-Selective Photonic Lantern based on Integrated 3D Devices Fabricated by Ultrafast Laser Inscription,” in Optical Fiber Communication Conference, 2015, p. W2A.16.